A quantum interface between single atoms and nanophotonic structures

A quantum interface between single atoms and nanophotonic structures

a dissertation presented
by
Jeffrey Douglas Thompson
to
The Department of Physics

in partial fulfillment of the requirements
for the degree of
Doctor of Philosophy
in the subject of
Physics

Harvard University
Cambridge, Massachusetts
August 2014

Dissertation Advisor: Professor Mikhail Lukin Jeffrey Douglas Thompson

A quantum interface between single atoms and nanophotonic structures

Abstract

Strong interactions between light and atoms at the single-quantum level are an important ingredient for quantum technologies, as well as for studies of fundamental effects in quantum optics. This thesis describes the development of a novel experimental platform that allows for trapping a single rubidium atom in the evanescent mode of a nanofabricated optical cavity with sub-wavelength dimensions. By virtue of their small size, these cavities provide extremely large atom-photon coupling strengths and good prospects for scalability and integration into complex quantum optical circuits. Positioning the atom near the nano-structure is accomplished using a scanning optical tweezer dipole trap. As a first application, we have demonstrated a coherent optical switch, where a single gate photon controls the propagation of many subsequent signal photons, with the interaction mediated by the atom and cavity. We have also shown that the optical response of the combined atom-cavity system is nonlinear at the level of one or two photons.

Contents

Listing of figures

For my family, Alix, Doug, Steve and Nathalie.

Acknowledgments

The work described in this thesis would not have been possible without the contributions of many other people, and I would like to acknowledge them in this section.

First, I should thank my advisor Misha Lukin, for his support and encouragement over the last six years. I have learned many things from Misha during this time, but still struggle to emulate his fearless approach to science, which makes working with him equal parts terrifying, exciting and productive. I would also like to thank my second advisor, Vladan Vuletić, for his seasoned advice and enthusiasm, and for gently nudging us back on to the right track many times. I am also grateful to Markus Greiner for our conversations over the years, and for agreeing to serve on my committee.

In the lab, I had the pleasure of working for many years with Tobias Tiecke, whose broad interests, technical acumen and good humor in the lab made our work considerably easier and more enjoyable. Additionally, Nathalie de Leon brought to our project a wealth of clearly thought-out concepts and techniques for nanophotonics, both for design and fabrication, without which we would have never been able to get off the ground in that aspect of the project. Sasha Zibrov and Alexey Akimov provided a significant amount of momentum and know-how in the early stages of the project, while Darrick Chang, Frank Koppens, Chun Yu, Dirk Englund, Qimin Quan and Marko Loncar contributed important materials and ideas. More recently, it has been a pleasure to be joined

by Thibault Peyronel and Kali Nayak in the lab. Their experience and different perspectives have made it very rewarding to turn the project over to them.

The best thing about being in a place as productive as the Lukin group, or Harvard more generally, is the high density of experts in various subjects to discuss with and learn from. Over the years, it has been a pleasure to be colleagues and classmates with Shimon Kolkowitz, Peter Maurer, Michael Gullans, Steve Bennett, Soonwon Choi, Yiwen Chu, Kristiaan de Greve, Ruffin Evans, Johannes Feist, Chris Laumann, Mike Goldman, Sarang Gopalakrishnan, Alexey Gorshkov, Mohammad Hafezi, Liang Jiang, Eric Kessler, Georg Kuckso, Peter Komar, Albert Lee, Lee Liu, Jero Maze, Arthur Safira, Brendan Shields, Alp Sipahigil, Emre Togan, Quirin Unterreithmeier, Hendrick Weimer, Norm Yao and Jiwon Yune.

I would also like to acknowledge the Hertz Foundation for their financial support throughout my PhD, and also for the opportunity to get to know an exceptional community of scientists.

I am extremely fortunate to have had the constant and unconditional support of my family during my time in graduate school, from my parents Doug and Alix, and my brother Steve. Lastly, I owe the greatest thanks to my wife Nathalie, who has been the best partner imaginable in every aspect of life.

Chapter 1

Introduction

Over the last 30 years, considerable theoretical and experimental efforts have been devoted to using manifestly quantum mechanical systems to accomplish useful things, such as quantum computing, quantum communications, quantum simulation and quantum-enhanced measurement. In the case of quantum communications, quantum mechanics fundamentally forbids the copying of quantum states [1], allowing the privacy of a communications channel to be verified and guaranteed by the laws of physics [2]. In the other fields, the role of quantum mechanics is a little more subtle, but can be fairly summarized by saying that the space of configurations available to a quantum system of a given number of particles is vastly larger than for the corresponding classical system because of the possibility for quantum entanglement and superpositions.

The central challenge that has so far kept these technologies from developing to the point of being widely applied is that quantum states are very sensitive to perturbations from their surrounding environment. An ordinary computer processor, when running, is hot to the touch, and that heat results from information-carrying currents being dissipated by resistance in the wires in the circuit. In the classical case, this problem can be overcome by simply using more current to boost the signal. In the quantum case, how-

ever, the absorption of even a single quantum of energy by the environment can completely destroy the quantum state of the computer, eliminating its quantum advantage. From an engineering perspective, the challenge to developing technologically useful quantum systems is to identify systems that can be completely isolated from the environment, but that can still be manipulated, controlled and coupled to each other to encode information and perform logic operations. The list of systems under investigation is long and still growing, and includes superconducting circuits, optical photons, electron and nuclear spins in single atoms and ions, as well as spins and charges in solid materials. Each of these systems has advantages and drawbacks, which vary depending on the application.

This thesis is devoted to engineering efficient, dissipation-free interaction between single atoms and single photons. Separately, these are excellent stationary and traveling carriers of quantum information, respectively, but achieving strong coupling between them in a useful experimental platform is still an ongoing pursuit. Many atoms naturally have perfect coupling to photons, in the sense that an atom in an excited state *always* relaxes through spontaneous emission by emitting a photon with a known and predictable spatial mode, without loss into other non-photonic channels. However, this naturally occurring coupling is not very useful, because the resulting photon wave packet is unwieldy, propagating radially outward from the atom in all directions at the same time. Therefore, the experimental challenge is to enhance the coupling to a single, more accessible spatial mode, to the point that the atomic emission into this mode dominates over the natural coupling to all the other directions. From this perspective, we have redrawn the boundary of our system to include only the atom and the target mode, and the natural emission into all directions now acts as dissipation from this reduced system.

The physical requirements necessary to achieve this goal can be understood from a simple calculation. If the target optical mode is confined to a volume V, then a single

photon in that mode will have a characteristic electric field strength $E_0 = \sqrt{\frac{\hbar\omega}{\epsilon_0 V}}$, where ω is the frequency of the optical mode and ϵ_0 is the permittivity of the medium (which we take to be vacuum) [3]. The matrix element coupling the atomic dipole to this mode is then $g = dE_0$, where d is the electric dipole moment associated with the atomic transition. In addition to the volume, the mode is also characterized by a linewidth $\kappa = \omega/Q$, which represents the rate at which light in the target mode decays (for example, by leaking out of an optical cavity through the mirrors). Under the assumption (valid throughout this work) that the optical cavity decay rate is larger than the atom-photon coupling rate ($\kappa > g$), then the atom will undergo spontaneous emission into the target mode at a rate proportional to g^2/κ, because the coherent oscillations associated with the coupling g are interrupted by the cavity decay. Comparing this "good" rate to the "bad" rate of emission into all directions (which we call γ) gives us the ratio $\eta = g^2/(\kappa\gamma)$, which we call the *cooperativity*. In terms of the physical parameters of the optical mode V and Q, the cooperativity has the simple relationship $\eta \propto Q/V$ (γ and d cancel since $d \propto \sqrt{\gamma}$ provided there are no other decay channels for the atomic excited states). Therefore, the engineering challenge is to position atoms in optical modes with high quality factors (long photon lifetimes) and small spatial volumes.

Creating systems with large cooperativity has been a fruitful endeavor for more than thirty years in the field of cavity quantum electrodynamics, or cavity QED for short [4]. Early work was performed in the microwave domain with Rydberg atoms [5, 6]. In the optical domain, high cooperativities were first achieved for single alkali atoms in Fabry-Perot cavities in the mid-1990's [7]. In these systems, the volume is minimized by using curved mirrors that minimize the beam spot size in the center of the cavity (typically achieving volumes in the range of 10^4 to 10^6 λ^3, where λ is the optical wavelength), while high quality factors are achieved by using highly reflective mirror coatings (with finesses

approaching or exceeding one million). Although Fabry-Perot cavities are still widely used as a convenient, technologically mature platform (*e.g.*, [8–10]) with record cooperativites exceeding $\eta = 100$, much effort in the field has recently been devoted to moving to smaller optical cavities, where the light is no longer confined by mirrors but instead by total internal reflection in a solid structure. Because these structures can be made very small while still maintaining high quality factors, it is in principle possible to achieve much higher cooperativities in this way.

The first cavity QED experiments with micro-fabricated solid cavities were performed using quantum dots instead of atoms (*e.g.*, [11]), as they have the natural advantage of existing in the solid material from which the cavity is fabricated. Since then, several experiments with atoms have been realized by positing an ensemble of laser-cooled atoms in the vicinity of solid cavities in the form of silica microtoroids [12] or so-called bottle resonators in tapered silica optical fibers [13]. In these experiments, the atoms experience brief, few-microsecond periods of high-cooperativity coupling ($\eta \sim 10$) to the cavity when they pass through the evanescent field of the cavity. The characteristic cavity volumes are now as small as $10^3\lambda^3$. While this transient coupling has been suitable for the first generation of experiments, it has been an outstanding challenge to confine atoms in the evanescent field of a solid cavity for longer than a few microseconds. This would enable scaling to experiments with multiple atoms coupled simultaneously, and also allow the long ground-state coherence of the atoms to be exploited as a quantum memory.

This thesis presents the realization of even smaller solid optical cavities with volumes of less than one cubic wavelength, and experimental technique for trapping atoms in their evanescent field at sub-wavelength distances from the surface. This allows us to achieve high-cooperativity coupling for extended periods of time. The trapping is performed by loading a single atom into a tightly focused "optical tweezer" dipole trap, and

then moving the optical tweezer to position the atom near the surface of the cavity. This experimental platform has allowed us to demonstrate several applications, including optical nonlinearities at the one- and two-photon level, a switch that allows a single photon to control the propagation of a subsequent classical field, and a quantum non-demolition detector for optical photons.

1.1 Outline of this thesis

This thesis begins in Chapter 2 with the development of the optical tweezer trap used to position the atoms near the cavity. This work is based on previous results showing that it is possible to load and observe single atoms in a small-volume optical dipole trap [14] by simply turning it on in the middle of a standard magneto-optical trap. It has additionally been shown that such a trap can be moved around to change the position of the atom [15]. However, in order to use the optical tweezer to position an atom precisely, it is additionally important that the atom be tightly localized to the center of the optical tweezer. While this localization is ultimately limited by the quantum zero-point fluctuations of the optical tweezer potential, this limit had not been experimentally realized prior to our work. To this end, we implemented Raman sideband cooling to lower the temperature of the atom in the tweezer, ultimately achieving ground-state cooling in two out of three axes. The atomic localization was improved by more than 100-fold (in volume), to $24 \times 24 \times 270$ nm. This chapter is based on our previously published work in Ref. [16].

In Chapter 3, we apply the optical tweezer to position single atoms near the surface of two solid objects: a tapered optical fiber and a photonic crystal optical cavity. This portion contains the most crucial technical insight of this work, which is that the optical

tweezer transforms into an optical lattice when it is pointed at a surface, and that atoms initially confined in the tweezer can be adiabatically loaded into the lattice site closest to the surface. The distance between the closest lattice site and the surface is tunable by the wavelength, polarization or geometry of the substrate, but is generally around $\lambda/4$. We present experimental results showing that the atom is trapped in the lattice site closest to the surface with both substrates. In the case of the photonic crystal cavity, it is also demonstrated that the atom can be moved along the cavity axis to map out the intensity distribution of the cavity mode, and the atom-cavity coupling strength is quantified by looking at the atom-induced reduction in transmission through the cavity. The measured cooperativity is around $\eta = 0.1$, limited by the low quality factor of the cavities. However, the atom-photon coupling strength g exceeds 300 MHz, which is a record for neutral atoms and a direct consequence of the small mode volume of the photonic crystal cavity combined with the proximity of the atom to it. Important technical details and supporting calculations can be found in Appendix A. This chapter is based on our previously published work in Ref. [17].

In Chapter 4, we reap the benefits of several technological advances in cavity fabrication (described in Appendices B and C) to achieve $\eta \sim 8$, which enables several intriguing applications. The key result of having a high cooperativity is that the reflection phase of the cavity changes by π depending on whether the atom is coupled to the cavity. Since the coupling can be turned on and off by changing the hyperfine state of the atom (effectively detuning it from resonance), this enables a quantum phase gate between a qubit stored in the atomic spin and a photon incident on the cavity. We apply this phase gate interaction to demonstrate a "quantum switch", where the presence or absence of only a *single* gate photon flips the hyperfine state of the atom, and determines the propagation of a subsequent signal photon (or possibly many of them). Additionally, we demonstrate

quantum optical nonlinearities at the level of one and two photons, which arise from the fact that the π phase shift in the reflection arising from the single atom disappears when the atom is saturated, which can occur with only one photon because of the strong atom-photon coupling. This chapter is based on our previously published work in Ref [18].

Our ongoing work to further increase the cooperativity and improve the other performance aspects of the experiment is partially documented in Chapter 5. Here, we show that by carefully engineering the process of producing tapered optical fibers, we can improve the coupling efficiency between the fiber and the waveguide to more than 97%. This chapter is based on a manuscript that has been submitted for publication [19].

Chapter 2

Raman sideband cooling of single atoms in a tightly focused optical dipole trap

2.1 Introduction

We investigate quantum control of a single atom in a tightly focussed optical tweezer trap. We show that inevitable spatially varying polarization gives rise to significant internal-state decoherence, but that this effect can be mitigated by an appropriately chosen magnetic bias field. This enables Raman sideband cooling of a single atom close to its three-dimensional ground state (vibrational quantum numbers $\bar{n}_x = \bar{n}_y = 0.01, \bar{n}_z = 8$) even for a trap beam waist as small as $w = 900$ nm. The small atomic wavepacket with $\delta x = \delta y = 24$ nm and $\delta z = 270$ nm represents a promising starting point for future hybrid quantum systems where atoms are placed in close proximity to surfaces.

Single atoms in "optical tweezer" traps [14] are a promising resource for various applications in quantum science and engineering. They can be individually moved [15], manipulated [20, 21], read-out [22, 23], and used to implement quantum gates [24, 25], in a manner similar to trapped ions. At the same time, they may be strongly coupled to photonic [26, 27], plasmonic [28], or other solid-state systems [29–31], opening a new frontier

for the realization of quantum networks and hybrid quantum systems. These intriguing applications require trapping single ultra-cold atoms near surfaces at distances well below an optical wavelength. While this is challenging for ions [32], and magnetically trapped atoms [29, 33], it is achievable with neutral atoms in optical dipole traps.

An optical tweezer can be efficiently loaded with a single atom from an optical molasses by making use of a light-induced two-body loss process (collisional blockade) [14, 34]. The temperature of an atom loaded in this way is in the range of $30 - 200\mu$K [20, 21, 24, 25, 27, 35, 36], at which point the atom has a characteristic root-mean-square (rms) spatial extent of $\delta r \approx 200$ nm and $\delta z \approx 1\mu$m in the radial and axial directions, respectively. This spatial spread is an impediment in several current experiments [24, 37], while the elevated temperature reduces the coherence time [20, 21, 24, 25, 36]. Moreover, interfacing the atom to the near field of a solid-state structure requires much stronger confinement, as in this case the atom must be localized on the scale of a reduced resonance wavelength $\lambda/2\pi = 120$ nm (for Rb).

These applications require significant improvements in laser cooling and coherent manipulation. Raman sideband cooling is a powerful technique to control atomic motion, as was demonstrated previously for ions and atomic ensembles in larger traps [38–42]. Coherent raman transitions between two stable ground states that change the atom's vibrational level can be used to remove energy, combined with an optical pumping process to remove entropy and complete the cooling cycle (Fig. 2.1a).

However, in very tightly confining traps with beam waist $w \sim \lambda$, polarization effects associated with the breakdown of the paraxial approximation can strongly impede coherent manipulation and cooling. Such tightly focussed beams exhibit a longitudinal polarization component, which even for linearly polarized input fields results in spatially varying elliptic polarization [43–46]. The corresponding atomic-state-dependent trapping po-

tentials reduce atomic coherence, induce force fluctuations, and impair cooling [47]. These effects are present not only in optical tweezers, but also at sub-wavelength distances from dielectric boundaries [27, 48], and in projected optical lattices to be used for many-body quantum simulation [49].

In this Letter, we present a detailed study of the longitudinal polarization component of a dipole trap formed by a high-numerical-aperture lens, demonstrate how the associated effect on a trapped atom can be partially compensated using a properly oriented magnetic bias field, and apply these results to perform Raman sideband cooling of a single atom. After cooling, the atom is in the ground state along the two radial directions ($\bar{n}_r = 0.01^{+0.06}_{-0.01}$), and occupies just a few quantum states ($\bar{n}_a = 8.1(8)$) in the axial trap direction. The corresponding rms size of the atomic wavepacket is given by the ground state length of $\delta r = 24$ nm in the radial directions, and a thermal extent $\delta z = 270$ nm in the axial direction. This represents a hundred-fold reduction in spatial volume, and a reduction by 10^4 in phase-space volume, over the starting conditions.

2.2 Vector light shifts from non-paraxial polarization effects

The longitudinal polarization component can be understood in the framework of ray optics (see Figure 2.1b). Light entering a lens consists of parallel rays with transverse linear polarization. Upon refraction the polarization of each ray must also deflect to remain transverse to the ray [43]. In the diffraction-limited volume around the focus, all rays interfere and the resulting field is elliptically polarized. Following Fig. 2.1b, two features emerge near the focus: the polarization vector is rotating in the plane set by the incident polarization vector and the optical axis, and the sense of this rotation is opposite above and below the optical axis.

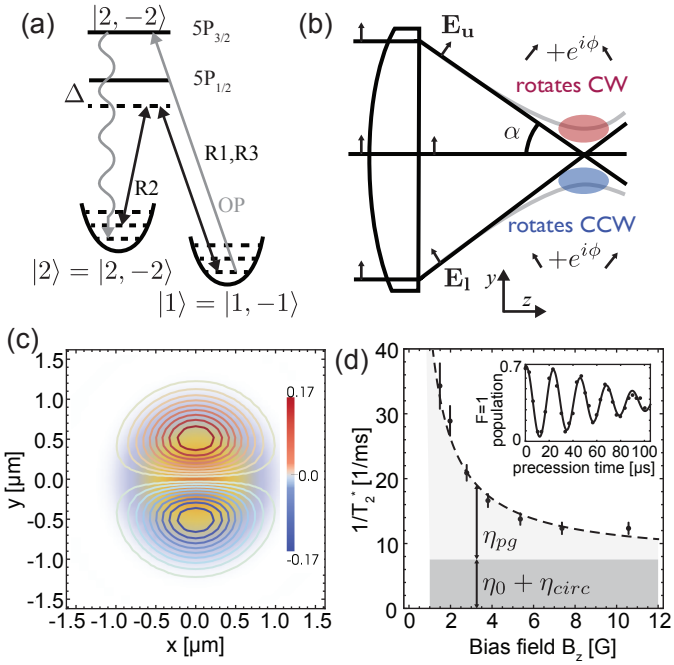

Figure 2.1: (a) Relevant levels and transitions in ^{87}Rb. The eigenstates of the harmonic potential for the ground state are indicated with dashed lines. Atomic levels are defined in the $|F, m_F\rangle$ basis. See text for beam orientations and polarizations. (b) The origin of elliptical polarization near the focus (see text). (c) Cut through the focal plane for $\alpha = 0.43$. Contour lines show $\tilde{C}_x$, which is C_x scaled to the local intensity $|E(\vec{r})|^2/|E(\vec{r}_{max})|^2$. Background shading shows Gaussian intensity profile for comparison. (d) Dephasing rate between the states $|1\rangle$ and $|2\rangle$ as a function of bias field, with $\lambda_T = 815$ nm. The improvement at large bias fields is due to suppression of the polarization gradient. Fit is to model described in text: $\eta_0+\eta_{circ}$ are background dephasing rates from the finite detuning and slight elliptical polarization of the dipole trap; η_{pg} arises from the longitudinal polarization. Inset: Ramsey measurement of dephasing rate between $|1\rangle$ and $|2\rangle$ at $B_z = 10.5$ G.

For light that is far detuned compared to the excited-state hyperfine structure, the vector light shift for alkali atoms in the ground state is [50, 51]:

$$U(\mathbf{r}) = -U_0(\mathbf{r})\frac{\delta_2 - \delta_1}{\delta_2 + 2\delta_1}\mathbf{C}(\mathbf{r}) \cdot g_F\hat{\mathbf{F}} \tag{2.1}$$

where $U_0(\mathbf{r})$ is the scalar dipole trap potential, δ_1 and δ_2 are the detunings from the D1 and D2 lines, respectively, $\epsilon(\mathbf{r})$ is the local (unit norm) polarization vector, $\hat{\mathbf{F}}$ is the total angular momentum operator and $g_F = [F(F+1) - I(I+1) + J(J+1)]/F(F+1)$. The vector $\mathbf{C} = \mathrm{Im}[\epsilon(\mathbf{r}) \times \epsilon^*(\mathbf{r})]$ quantifies the direction and degree of ellipticity (with magnitude $|\mathbf{C}| = 1$ for circularly polarized light; 0 for linear polarization). Using the vector Debye integral [43], we have numerically computed the polarization near the dipole trap focus (Fig. 2.1c). The most important term is the polarization gradient dC_x/dy. For a lens with numerical aperture α, the maximum gradient, occurring at the beam focus, is well approximated by $3.1\alpha \sin\alpha/\lambda$ for uniform illumination of the lens aperture, and $2.6\alpha \sin\alpha/\lambda$ for illumination by a Gaussian beam with a $1/e^2$ diameter equal to the lens diameter. In the experiments presented here, $\alpha = 0.43$ and $\lambda = 815$ nm, so $dC_x/dy = 0.57/\mu$m. Since the state-dependent potential in Equation (2.1) is linear in $\hat{\mathbf{F}}$, it produces the same energy shifts as a magnetic field, so dC_x/dy can also be expressed as an effective magnetic-field gradient with magnitude $B'_x = 1.4$ G/μm at the trap center (using $U_0 = 0.82$ mK).

In the absence of an externally applied magnetic bias field, trapping potentials corresponding to different magnetic sublevels m_F are displaced by $\Delta x = \mu_B \Delta(g_F m_F) B'_x/(m\omega_r^2)$, where $\mu_B \Delta(g_F m_F)$ is the difference in the magnetic moment. For $\Delta(g_F m_F) = 1/2$, the resulting displacement is $\Delta x = 11$ nm, which is non-negligible compared to the ground state length $\sqrt{\hbar/2m\omega} = 24$ nm. While this state-dependent displacement could be useful for Raman cooling or other motional state manipulations [52, 53], it also leads to rapid internal-state decoherence on the timescale of the radial trap oscillation period.

This problem can be mitigated by applying a bias magnetic field $\mathbf{B} = B_z\hat{z}$ orthogonal to $\hat{x}$ that suppresses the effective field gradient according to $B_{tot} = \sqrt{B_z^2 + (B'_x y)^2} \approx B_z + (B'^2_x/2B_z)y^2$. In this case, the gradient causes only a state-dependence in the strength

of the harmonic trap potential. Superpositions of magnetic sublevels that experience different trapping potentials of the form $U_1(\mathbf{r}) = (1+\eta)U_2(\mathbf{r})$ are dephased with a coherence time $T_2^* = 0.97 \times 2\hbar/(k_B T\eta)$ [47], where T is the temperature of the atom and k_B is the Boltzmann constant. In the presence of a large orthogonal bias field, the polarization gradient contributes to η as $\eta_{pg} = \mu_B \Delta(g_F m_F) B_x'^2/(3m\omega^2 B_z)$ (the factor of 1/3 results from averaging over the three trap axes). We can use the dependence on B_z to accurately measure the polarization-induced gradient B', and improve the atomic coherence by applying a large bias field B_z (Fig. 2.1d).

We measure the decoherence between the states $|1\rangle \equiv |F=1, m_F=-1\rangle$ and $|2\rangle \equiv |F=2, m_F=-2\rangle$ by loading a single atom into a tweezer trap with a depth of 1.6 mK at zero bias field, then ramping down the trap depth to 0.82 mK as we ramp up the bias field B_z to the desired value. The atom is optically pumped into $|2\rangle$, the hyperfine transition $|2\rangle \rightarrow |1\rangle$ is driven by a two-photon Raman process in a Doppler-free configuration, and the state detection is accomplished using a push-out beam, as described in more detail below. The coherence time T_2^* is extracted from a Ramsey-type measurement, using a fit to the function introduced in Ref. [47].

At two different trap wavelengths λ_T, we fit $1/T_2^* = 1.03\,(\eta_0 + \eta_{circ} + \eta_{pg})\,(k_B T/2\hbar)$. The only free parameters are the degree of circular polarization in the incident dipole trap beam due to uncompensated birefringence along the beam path (η_{circ}) and the strength of the effective field gradient B_x'. The temperature is determined independently ($T = 40\mu$K for this measurement, see below for technique). η_0 reflects the different trapping potentials for $F=1$ and $F=2$ atoms due to the finite trap detuning. At $\lambda_T = (802, 815)$ nm, we find $B_x' = (2.4, 1.4)$ G/μm, and thus $dC_x/dy = (0.46(6), 0.54(3))/\mu$m, in reasonable agreement with our estimate of 0.57 /μm.

2.3 Raman sideband cooling of a single atom

Having developed a detailed understanding of trap-induced decoherence in this system, we now turn to Raman sideband cooling. We use three orthogonal running-wave fields to drive Raman transitions, labeled R1-R3 (Fig. 2.1a). R1 propagates anti-parallel to the dipole trap ($-\hat{z}$) and is circularly polarized to drive σ_- transitions. R2 propagates along $\hat{x}$ and is circularly polarized; R3 propagates along $\hat{y}$ and is linearly polarized along $\hat{x}$. Optical pumping to the $|2\rangle$ state is provided by circularly polarized beams co-propagating with R1, addressing the $F = 1 \rightarrow F' = 2$ and $F = 2 \rightarrow F' = 2$ transitions on the D2 line. The frequencies of the lasers are set to the measured resonances in the dipole trap, which are shifted by ~ 30 MHz from the resonances in free space; the intensities are about 100 times less than saturation. We measure the $F = 1$ population by pushing out any atom in $F = 2$ using a circularly polarized beam along the optical pumping path that is resonant with the $F = 2 \rightarrow F' = 3$ transition on the D2 line, then measuring whether the atom has remained trapped by turning the molasses back on.

In a typical experiment, we load an atom from the MOT into the optical dipole trap with a depth of 1.6 mK at zero bias field, then decrease the trap depth to 0.82 mK while ramping the bias field B_z up to 7.5 G. Lowering the trap depth serves to increase the coherence time while leaving the trap frequencies high enough that sideband cooling is still achievable, with $(\omega_r, \omega_a) = 2\pi \times (100, 15.6)$ kHz. All temperatures reported in this paper are measured in the 0.82 mK deep trap. We cool the atoms in the following sequence: we first apply the R2 and R3 beams (Fig. 2.1) and the optical pumping beams together for 10 ms to continuously cool the radial modes; then, we perform ten cycles consisting of 2 ms of axial cooling using the R1 and R2 beams, followed by 4 ms of radial cooling using the R2 and R3 beams again. This sequence prevents the radial modes from heating while

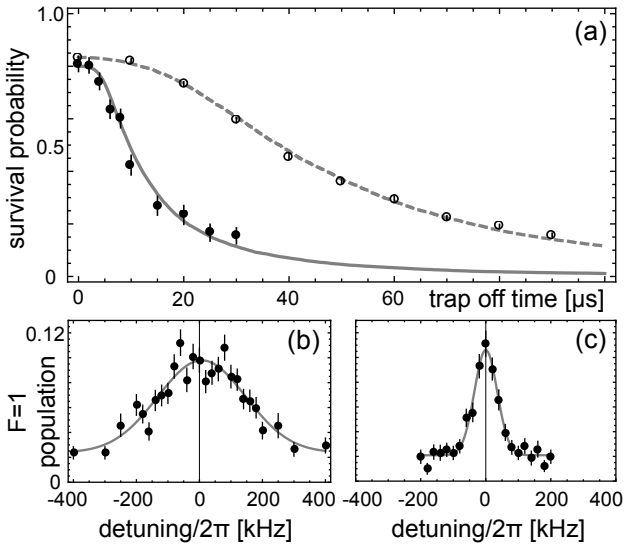

Figure 2.2: (a) Release and recapture temperature measurement. (Closed, open) circles show measurements (before, after) radial cooling. A Monte Carlo model yields kinetic energies K such that $2K/k_B = 52(4)\mu$K before cooling, and $(2K_r/k_B, 2K_a/k_B) = (2.4(1), 158(14))\mu$K after cooling. (b,c) Doppler measurement of the axial kinetic energy before and after cooling the axial mode. (b) After radial cooling only, $2K_a/k_B = 129(19)\mu$K. (c) After radial and axial cooling, $2K_a/k_B = 8.1(1)\mu$K.

the axial cooling proceeds.

The parameters for the first radial cooling phase are optimized by measuring the temperature using a release and recapture technique [54]. This data, shown in Figure 2.2a, is fit using a Monte-Carlo simulation [35]. The initial kinetic energy per dimension K is such that $2K/k_B = 52\mu$K. The measurement after cooling yields anisotropic kinetic energies of $2K_r/k_B = 2.4(1)\mu$K in the radial direction and $2K_a/k_B = 158(14)\mu$K in the axial direction (the release and recapture technique is only weakly sensitive to the axial mode). The fitted kinetic energies represent the global minimum in χ^2 over the entire space of three independent energies for each axis, including unphysical temperatures less than the ground state energy $\hbar\omega/2k_B = 2.4\mu K$ for the radial modes. The agree-

ment of the measured kinetic energy with that of the zero-point motion suggests that we have reached the radial ground state after this cooling phase alone. The radial cooling works best with a two-photon Rabi frequency $\Omega_{R2,R3} = 2\pi \times 17$ kHz and a detuning of $-\omega_r = -2\pi \times 100$ kHz from the two-photon resonance.

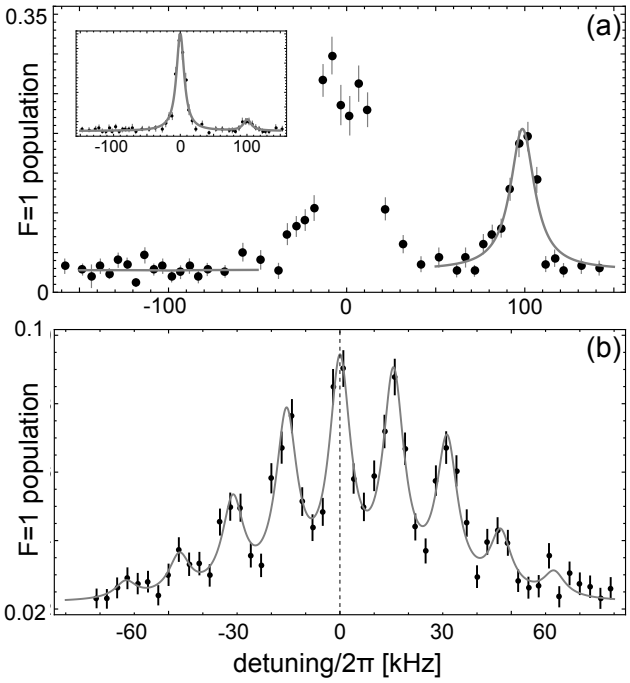

Figure 2.3: Sidebands showing final occupations in the (a) radial and (b) axial directions. In (a), the red and blue sideband amplitudes are fit to independent lorentzians; their ratio yields a radial temperature $\bar{n}_r = 0.01^{+0.06}_{-0.01}$. Inset: same measurement with shorter pulse length so the carrier is also resolved. In (b) 9 peaks are fit with independent heights, but equal spacings and widths. The heights are well-described by a thermal distribution with $\bar{n}_a = 8.1(1)$.

To characterize the axial temperature independently after the radial cooling, we measure the Doppler width of the $|2\rangle$ to $|1\rangle$ transition when driven with the R1 and R2 beams. The wavevector $\Delta\mathbf{k}_{12} = \mathbf{k}_{R1} - \mathbf{k}_{R2}$ has a projection onto the axial and radial di-

rections, but the Doppler profile should mostly be sensitive to the axial mode here since the radial degrees of freedom are already cold. After the first stage of radial cooling, we measure a kinetic energy of $2K_a/k_B = 129(19)\mu$K (Fig. 2.2b). After optimization, we obtain a feature with a width corresponding to $2K_a/k_B = 8.1(1)\mu$K (Fig. 2.2c). This data is fitted to a Gaussian, which conservatively assumes no power broadening. The optimum cooling parameters are a two-photon Rabi frequency of $\Omega_{R1,R2} \sim 2\pi \times 5$ kHz and a detuning of $-2\pi \times 60$ kHz. The parameters used for the interleaved radial cooling phases are the same as above.

To obtain more precise measurements of the final temperature of the atom, we resolve the asymmetric motional sidebands along two axes. The ratio of the sideband amplitude gives information about the vibrational state occupation of the atom [38]. Figure 2.3a shows the sidebands measured in the radial direction with small $\Omega_{R2,R3}$. The blue sideband is essentially absent, with a fitted amplitude 100 times smaller than the red sideband. From this, we extract a radial mode occupation of $\bar{n}_r = 0.01^{+0.06}_{-0.01}$. We do not know to what extent the two radial modes are non-degenerate or what the natural axes are, but from the release-and-recapture data showing that both modes must be very cold, and the fact that the spectrum shown here does not change if we measure it at a different time after the cooling (up to 100 ms later), we infer that the two modes are not perfectly degenerate and the R2+R3 beams address both modes. Therefore, we conclude that this spectrum reflects the temperature of both radial modes.

We also resolve the axial motional sidebands using the R1 and R2 beams at very low power, and observe a spectrum with nine peaks that is slightly asymmetric (Fig. 2.3b). We find that the ratios of the measured peak heights correspond very well to a thermal distribution $\rho_{nn} \propto \exp(-n/\bar{n}_a)$ with a mean vibrational number $\bar{n}_a = 8.1(8)$. The corresponding energy $(\bar{n}_a + 1/2)\hbar\omega_a = 6.5\ \mu\text{K} \times k_B$ is similar to the result of the Doppler

measurement above.

Several properties of the cooled atom are worth noting. The heating rate for the radial degrees of freedom is very low, less than $\Delta\bar{n} < 0.3$ over 200 ms. We observe no heating while translating the atom over distances $\sim 20\mu$m in ~ 10 ms using a scanning galvanometer mirror. Decreasing the Rabi frequency $\Omega_{R1,R2}$ and detuning during the last cooling phase does not decrease the final axial temperature. This is possibly due to the fact that we cannot separately address the axial mode, or to our choice to optically pump along the axial direction, resulting in more heating along that direction. We are not aware of any fundamental effects that would prevent cooling to the ground state in this system.

2.4 Conclusion and outlook

It may be possible to extend the demonstrated method to perform high-fidelity state detection [22, 23] while cooling within one hyperfine state, and collecting optical pumping photons. Furthermore, it should also be possible to cool small ensembles of atoms held in arrays of traps [34] or together in a single trap. In the latter case, Raman cooling is advantageous compared to an optical molasses, in that the detuning of the optical pumping beam can be chosen over a wide range, allowing the effects of light assisted collisions [55] and heating due to rescattered photons [41] to be reduced.

After completing this work, we became aware of the closely related work in Ref. [56].

Chapter 3

Deterministic coupling of a single trapped atom to a nanoscale optical cavity

3.1 Introduction

Hybrid quantum devices, where dissimilar quantum systems are combined to attain qualities not available with either system alone, may enable far-reaching control in quantum measurement, sensing, and information processing. A paradigmatic example is trapped ultra-cold atoms, with excellent quantum coherent properties, coupled to nanoscale solid-state systems, which allow for strong interactions. We demonstrate a deterministic interface between a single trapped rubidium atom and a nanoscale photonic crystal cavity exhibiting sub-wavelength confinement of an optical mode and correspondingly large single-photon fields exceeding 1 kV/cm. By positioning the atom with a resolution down to 190 nm, we probe the cavity near-field non-invasively below the diffraction limit and observe large atom-photon coupling, quantified by the measured single-photon Rabi frequency $2\pi \times 600$ MHz. This approach enables the realization of integrated, strongly-coupled quantum nano-optical circuits.

Trapped, ultra-cold atoms coupled to nanoscale optical cavities are exemplary hybrid

quantum systems [57, 58] with potential applications ranging from single-photon nonlinear optics [11, 59–62] to quantum networks [63, 64]. However, realizing the largest interaction strengths requires placing and controlling an atom very close to a surface, within the near field of the confined optical mode, as set by the reduced atomic resonance wavelength of $\lambda/2\pi \sim 125$ nm for rubidium. Position control at this level has been achieved for single atoms in free space and in micrometer scale cavities using standing waves [65, 66], or high numerical-aperture optics [15, 49]. Achieving similar control close to surfaces is much more challenging, because attractive atom-surface forces are comparable to typical trapping forces for cold atoms in this regime. Previously, atomic ensembles have been stably trapped at distances of 500 nm from a surface using magnetic traps formed by patterned electrodes [29, 33], and down to 230 nm using optical dipole traps based on evanescent waves [27, 67].

3.2 Technique for trapping atoms near nanostructures using an "optical tweezer"

Our technique to deterministically position an atom near an arbitrary nanoscale object uses a tightly focused optical tweezer beam [14] that is retro-reflected from the nanoscale object itself [68, 69], and red-detuned from the atomic resonance (Figure 3.1A). The resulting standing-wave optical lattice has a local intensity maximum, corresponding to a minimum of the potential energy, at a typical distance $z_0 \sim \lambda_T/4$ from the surface, with additional maxima farther away spaced in increments of $\lambda_T/2$ (λ_T is the trap laser wavelength). The lateral position of the trap can be controlled by moving the focused incident beam, while the distance z_0 depends on the phase shift of the reflected light, which is determined by the geometry of the nanostructure. In certain cases, changing the structure

dimensions allows z_0 to be tuned between nearly 0 and $\lambda_T/2$ (Figs. A.3). Crucially, the lattice site closest to the surface can be deterministically loaded with a single atom from a conventional free-space optical tweezer simply by scanning the latter onto and over the surface, provided the atom has been originally prepared at sufficiently low temperature [16]. Even though the attractive van der Waals interaction between the atom and the surface limits the minimum trap distance to about 100 nm for realistic laser intensities (see Appendix A), this method nevertheless allows for direct, strong and reproducible near-field optical coupling of atoms to solid-state nanostructures of interest.

The nanostructure in the present experiment is a photonic crystal waveguide cavity (PWC) that is mounted to a tapered optical fiber tip and placed in the focal plane of a high numerical aperture lens (Figs. 3.1A,B, A.1). A magneto-optical trap (MOT) is formed near the fiber tip and used to load the optical tweezer ($\lambda_T = 815$ nm, $1/e^2$ waist $w = 900$ nm, depth $U_0/k_B = 1.6$ mK) with one atom at a distance of $40\,\mu$m from the nanostructure. (The presence of only a single atom is ensured by the collisional blockade effect [14].) After a period of Raman sideband cooling to the vibrational ground state in the two radial directions, and to a few vibrational quanta in the direction along the tweezer [16, 56], we translate the optical tweezer using a scanning galvanometer mirror (Fig. 3.1C) until it is aimed directly at the nanostructure, thereby loading the atom into the lattice.

3.3 Measuring and controlling the position of the atom

We first verify that we can deterministically load the lattice site closest to the surface by positioning an atom near a bare tapered nanofiber tip (see figure 3.2A,B) without the PWC present. We distinguish the lattice sites spectroscopically by means of a weak, off-

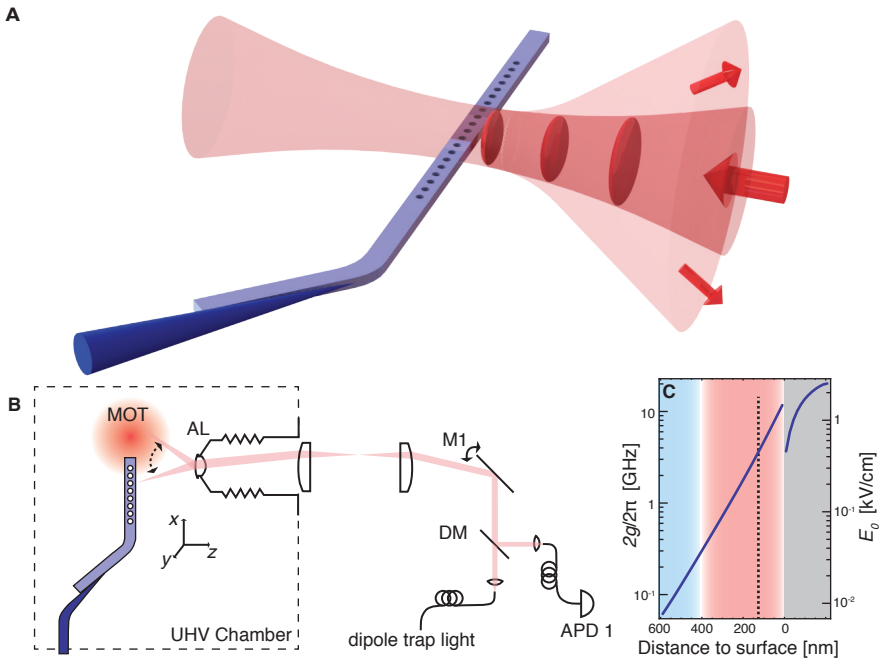

Figure 3.1: Experimental concept. (A) The atom trap near a nanoscale solid-state structure (here, a photonic crystal waveguide) arises from the interference of an optical tweezer with its reflection from the structure, which forms a standing-wave optical lattice. (B) Schematic of experimental apparatus. The trap is loaded with a single atom by displacing an optical tweezer from a nearby point in a free-space MOT. The trap is focused and steered by an aspheric lens (AL) and galvanometer mirror (M1). The presence of a single atom in the tweezer is detected by fluorescence on an avalanche photodiode (APD1), separated from the trapping light by a dichroic mirror (DM). (C) The single-photon Rabi frequency $2g$ and electric field strength E_0 at a given distance from the outer surface of a PWC cavity with mode volume $V = 0.42\lambda^3$. Negative distances correspond to points inside the dielectric. With a trap laser wavelength of 815 nm, the closest lattice site can be tuned from nearly 0-407 nm (shaded red), and the second lattice site from 407-815 nm (shaded blue). As discussed in the text, surface forces and currently realized trap depths limit the achievable distance to $z_0 \approx 100$ nm, at which point $2g/2\pi$ is several GHz.

resonant probe beam guided by the nanofiber. This beam produces a substantial differential AC Stark shift between the ground state hyperfine levels for lattice site A, and a much smaller shift for the more distant lattice sites (see Appendix A). Figure 3.2C shows the microwave-frequency spectra on the $|F = 1, m_F = 0\rangle \leftrightarrow |2, 0\rangle$ transition obtained by focusing the tweezer in different z-planes before loading the lattice (F and m_F indicate the atomic hyperfine and magnetic quantum numbers, respectively). Two distinct peaks appear: one near the unperturbed transition frequency at f_B, and another shifted by 150 kHz at f_A, which we identify as the Stark-shifted resonance frequency in the lattice site closest to the fiber. This identification is made by measuring the coupling of the atomic fluorescence into the fiber. Accounting only for well calibrated losses (detector quantum efficiency and a free-space fiber coupling stage) we expect a fluorescence collection efficiency in the closest (second closest) lattice site of 0.04 (0.002). The measured efficiency associated with peak f_A is 0.015 ± 0.006, thereby confirming the loading of the closest trap (see Appendix A). We conclude from the data in Fig. 3.1C that $100^{+0}_{-12}\%$ of the atoms loaded into the lattice are in the closest site, for optimal loading conditions. Independent measurements show that $94 \pm 6\,\%$ of all atoms are loaded into the lattice under the same conditions, after correcting for independently measured losses from background gas collisions.

We next demonstrate coupling an atom to the optical resonance of a PWC [70] fabricated in silicon nitride (Fig. 3.3A-C). It is attached to a tapered optical fiber tip, which provides both an efficient optical interface to the cavity and mechanical support. Because of the nanoscale dimensions of the waveguide, a significant fraction of the electromagnetic field energy is contained in the evanescent region just outside the waveguide, which allows for significant coupling to an atom trapped in this region without the need to place the atom inside the holes [71, 72]. As shown in Fig. 3.1C, single-photon Rabi frequencies

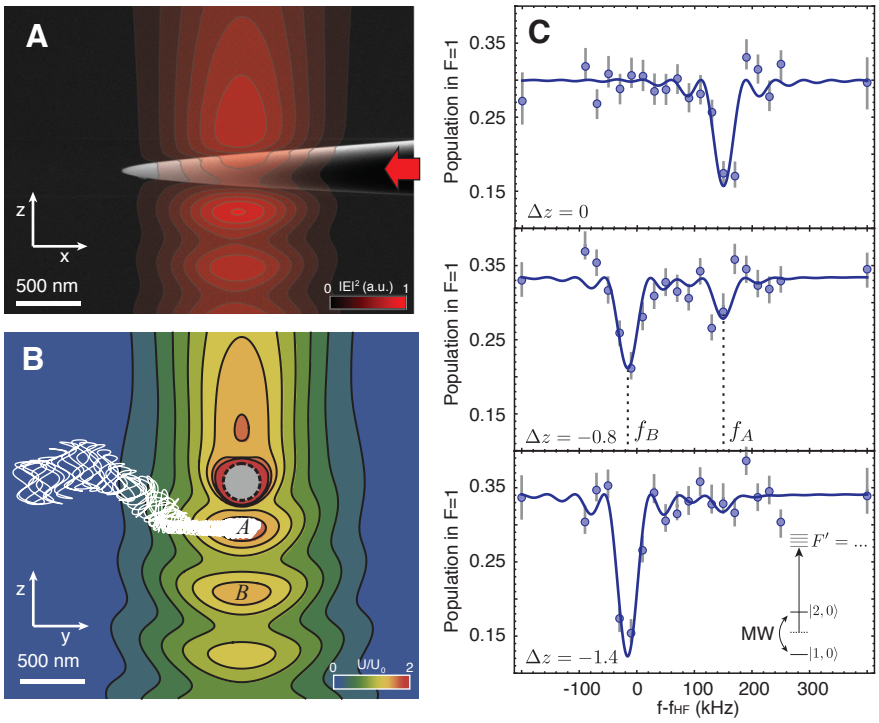

Figure 3.2: Loading the optical lattice near the surface. (A) A scanning electron microscope (SEM) image of a tapered nanofiber tip, overlaid with the simulated optical tweezer intensity in the xz-plane [carried out with a finite-difference time-domain (FDTD) method]. (B) Numerical simulation of loading process. Color map shows the trapping potential in the yz-plane (including surface forces) with the tweezer pointed directly at the nanofiber. The color scale is normalized to the potential depth of the tweezer in free space, U_0. The white line shows the trajectory of a typical trapped atom with energy $E = 3k_B \times 10\mu$K as the tweezer focus is scanned in the $\hat{y}$ direction. A (B) indicates the closest (next closest) lattice site. (C) Hyperfine transition spectra on the $|1,0\rangle \leftrightarrow |2,0\rangle$ transition, probing the atom-fiber separation. The (f_A,f_B) peaks show atoms loaded into the (A, B and more distant) lattice sites. The focal plane of the tweezer is displaced by Δz from the fiber mid-plane in each panel; in this way, different lattice sites can be loaded. At at $\Delta z = 0$ we extract that $100^{+0}_{-12}\%$ of the atoms in the lattice are in the closest site (see text).

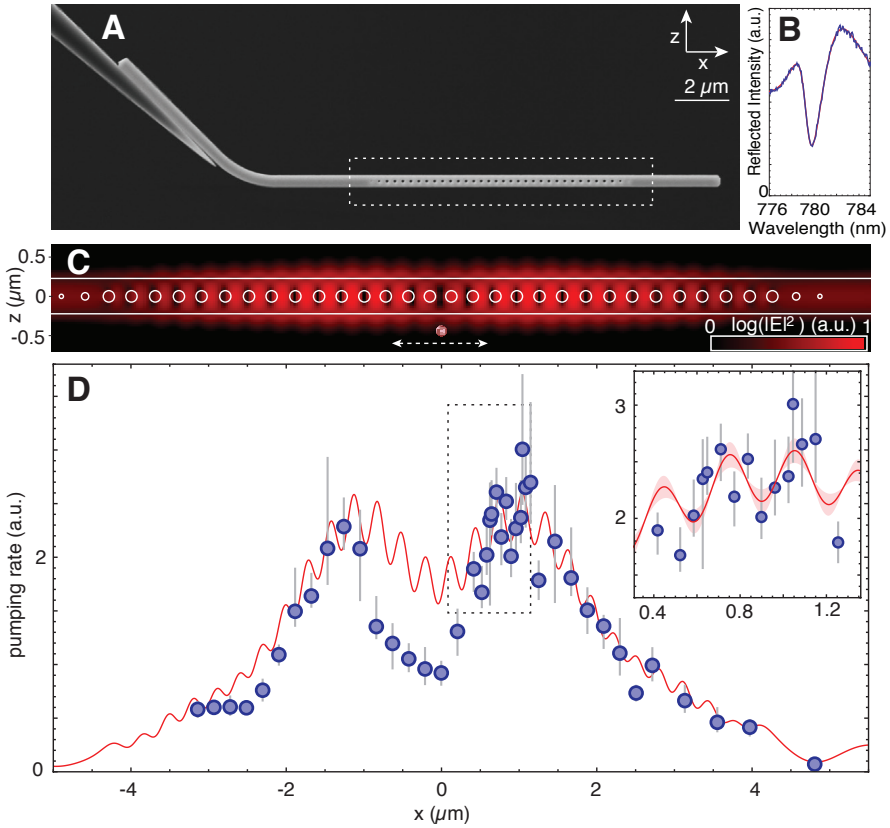

Figure 3.3: Coupling a single atom to a photonic crystal cavity. (A) An SEM image of a typical PWC attached to a tapered optical fiber. The fiber serves as both a mechanical support and an optical interface to the cavity. (B) Reflection spectrum of the PWC resonance near 780 nm, measured through the optical fiber. The line is a fit to a lorentzian plus a background of Fabry Perot modes of the waveguide, yielding $Q = 460(40)$ and $\lambda_0 = 779.5(1)$ (full spectrum in Fig. A.2). (C) Simulation of the PWC resonance at 779.5 nm, overlaid with a cross-section of the structure. The simulated mode volume is $V = 0.89\lambda^3$. *(continued on next page)*

Figure 3.3: *(continued)* (D) Measurement of the intensity distribution of the cavity using a trapped atom. Atoms are loaded at various positions indicated by the dashed arrow in panel (C), and the optical pumping rate from $F = 2 \rightarrow F = 1$ induced by the cavity field is measured. Error bars reflect one standard deviation in the fitted pumping rates. The red line shows a model based on simulations of the cavity mode convoluted with a Gaussian of 95 nm rms width, to incorporate for various broadening effects (see text). The systematic disagreement on the left side of the waveguide may be due to interference with background light from the fiber that is not coupled into the waveguide. *Inset* In a set of points acquired in a continuous 8 hour window to minimize alignment drift, the standing wave structure of the cavity mode can be clearly resolved.

$2g(r) = 2\mathbf{d} \cdot \mathbf{E}(\mathbf{r})/h$ in the range of several GHz (corresponding to single-photon electric fields of several hundred V/cm) are accessible for the atom-surface distances that can be realized with the present trapping technique.

To demonstrate the coupling of the atom to the cavity mode as well as the sub-wavelength lateral position control of the atom, we map out the intensity distribution of the cavity mode by scanning the atom along the waveguide. The local intensity is measured by pumping the cavity weakly with a laser tuned near the $F = 2 \rightarrow F' = 2$ transition of the D2 line, and measuring the optical pumping rate from $|F = 2, m_F = -2\rangle$ to $F = 1$. The measured rate is shown in Fig. 3.3D, along with a simulation of the mode intensity distribution. The simulated cavity mode is a standing wave (with a period given by the PWC lattice constant, $a \sim 290$ nm), modulated over several microns by a gaussian-like envelope with two lobes. Both features are clearly visible in the data. To achieve good agreement with the observed contrast in the optical-pumping rate, the simulation is convolved with a gaussian point-spread function with a root-mean-square (rms) width of 95 nm. This blur arises from drift in the tweezer alignment over the course of the measurement (32 hours), position jitter in the galvanometer mirror and motion of the atom. The rms zero-point atomic motion is 15-20 nm, and the thermal motion could

be somewhat larger because of heating from technical effects during the experimental sequence. Viewed as a non-invasive probe of the intra-cavity field distribution, this technique has a spatial resolution of 190(30) nm using the Sparrow resolution criterion [73].

3.4 Quantifying the atom-cavity coupling strength

Next, we quantify the atom-cavity coupling strength by measuring the reduction of the cavity transmission induced by a single atom. Given the cooperativity $\eta \equiv (2g)^2/(\kappa\Gamma)$, where κ and Γ are the full linewidths of the cavity and the atomic excited $5P_{3/2}$ state, respectively, the transmission in the presence of an (unsaturated) resonant atom is given by $T = (1+\eta)^{-2}$ [61]. To measure the transmission, we couple a weak probe field into the waveguide by scattering a focused beam off of the free-standing tip of the waveguide, and collect the transmitted light through the tapered optical fiber supporting the waveguide. With the atom placed at the cavity mode maximum ($x = +0.8\,\mu$m in Fig. 3.3D), we record the transmission of light near the $F = 2 \rightarrow F' = 3$ transition as shown in Fig. 3.4. The atom decreases the cavity transmission by at most 2.2%, and the full-width at half-maximum (FWHM) of the transmission dip is about 26 MHz, 4 times larger than the natural linewidth. The atom reduces the transmission for about 1 ms, during which time it scatters about 60 photons. The lifetime of the atom in the absence of the probe field is 250 ms; the probe-induced reduction of the lifetime is because of heating associated with photon scattering, which is likely dominated by fluctuating dipole forces as the atom is optically pumped between different magnetic sublevels experiencing different trapping potentials. This optical pumping occurs because the linearly polarized cavity field does not drive a single, closed transition. It also causes the transmission spectrum to be broadened and asymmetric, as the optical transition frequencies are different for each sublevel

because of light shifts and a magnetic bias field (see also Fig. A.7). These effects can be mitigated by using a "magic wavelength" trap [74], or by using a strong magnetic field to spectrally separate the cycling $|2,2\rangle \rightarrow |3,3\rangle$ transition.

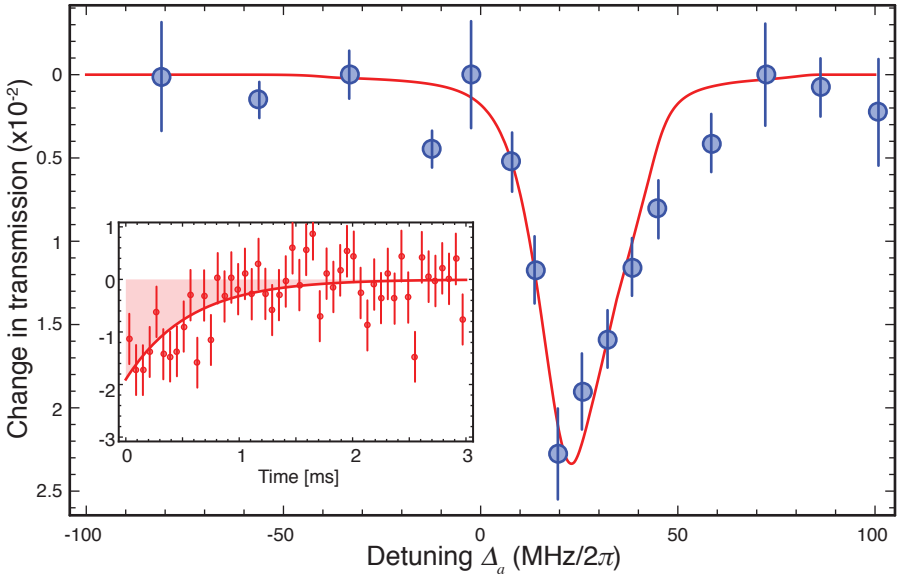

Figure 3.4: Change in cavity transmission from a single atom. The transmission of a weak probe beam tuned tuned to the $F = 2 \rightarrow F = 3$ transition is measured vs. detuning from the atomic resonance $\Delta_a = \omega_l - \omega_a$, with $(\omega_l, \omega_a) =$ (laser, zero-field atomic transition) frequency. The cavity resonance remains fixed at $\omega_a + 0.3\kappa$. Error bars reflect one standard deviation in the fitted transmission reduction. The line is a fit to a numerical model described in the text, yielding $2g = 2\pi \times 600(80)$ MHz. *Inset* Transmission vs. time for cw probe pulse at $\Delta_a = 27$ MHz. The cavity transmission is initially suppressed; after several hundred microseconds the atom is heated by the probe laser and lost from the trap, restoring transmission. Error bars show shot noise in the number of detected photons. The shaded area represents the absence of 60 photons from the transmitted field; the data is averaged over ~ 2500 runs with a single atom.

We have modeled the line broadening using numerical simulations of the master equation for a single Rb atom including the 12 relevant Zeeman states of the $F = 2 \rightarrow F' = 3$ transition (see Appendix A), and find reasonable agreement between the model,

the data, and the predicted coupling strength. The model, shown by the red line in Fig. 3.4, yields an estimate of $\eta = 0.07(1)$ and cavity QED parameters of $(2g, \kappa, \Gamma) = 2\pi \times (0.60(8), 840(80), 0.006)$ GHz for the $|2,0\rangle \rightarrow |3,0\rangle$ transition. This Rabi frequency $2g$ is in excellent agreement with estimates based on numerical modeling of the optical potential and cavity geometry, which yield a trap-surface distance of $z_0 = 260$ nm and $2g/(2\pi) \sim 620$ MHz on the $|2,0\rangle \rightarrow |3,0\rangle$ transition.

3.5 Conclusion and outlook

Several straightforward improvements can be made to increase the atom-photon coupling. An optimized waveguide geometry will allow $z_0 < 130$ nm, increasing $2g/(2\pi)$ to 3 GHz (see Appendix A). Additionally, quality factors as high as $Q = 3 \times 10^5$ have already been demonstrated for silicon nitride PWCs [75]. These two improvements together give a cooperativity of $\eta > 1000$. Even stronger coupling can potentially be accessed by trapping atoms inside the holes in the waveguide, using alternative PWC geometries to create the necessary trapping potentials [72].

The present technique opens up prospects for realizing a wide variety of hybrid quantum systems. For example, the method can be used to deterministically load multiple traps on the same or different PWCs, as well as cavities forming a network in two dimensions on a chip. In combination with the parallel fabrication and integration possible with nano-photonics, this is a promising route towards realizing complex nano-optical circuits with several atomic qubits. Potential applications range from quantum nonlinear optics to quantum networks and novel many-body systems [76, 77].

Beyond realizing these novel quantum optical systems, this trapping technique can be applied to other systems where it is beneficial to control atoms near surfaces, such as

quantum interfaces between ultra-cold atoms and mechanical oscillators [29] or electromagnetic circuits on a chip [78]. It can also be used for nanoscale sensing, or to probe atom-surface interactions at sub-micron scales. Finally, by starting from a quantum-degenerate gas it may be possible to simultaneously load multiple near-field traps separated by distances considerably smaller than $\lambda/2$ [79, 80]. This will allow studies of strongly correlated states to be extended into a new regime of high atomic densities and strong, long-range interactions.

Chapter 4

Quantum nanophotonic phase switch with a single atom

4.1 Introduction

In analogy to transistors in classical electronic circuits, a quantum optical switch is an important element of quantum circuits and quantum networks [63, 81, 82]. Operated at the fundamental limit where a single quantum of light or matter controls another field or material system [83], it may enable fascinating applications such as long-distance quantum communication [84], distributed quantum information processing [63] and metrology [85], and the exploration of novel quantum states of matter [86]. Here, by strongly coupling a photon to a single atom trapped in the near field of a nanoscale photonic crystal cavity, we realize a system where a single atom switches the phase of a photon, and a single photon modifies the atom's phase. We experimentally demonstrate an atom-induced optical phase shift [87] that is nonlinear at the two-photon level [88], a photon number router that separates individual photons and photon pairs into different output modes [89], and a single-photon switch where a single "gate" photon controls the propagation of a subsequent probe field [10, 90]. These techniques pave the way towards integrated quantum nanophotonic networks involving multiple atomic nodes connected by guided light.

A quantum optical switch [13, 61, 90–92] is challenging to implement because the interaction between individual photons and atoms is generally very weak. Cavity quantum electrodynamics (cavity QED), where a photon is confined to a small spatial region and made to interact strongly with an atom, is a promising approach to overcome this challenge [83]. Over the last two decades, cavity QED has enabled advances in the control of microwave [93–95] and optical fields [12, 13, 62, 96, 97]. While integrated circuits with strong coupling of microwave photons to superconducting qubits are currently being developed [98], a scalable path to integrated quantum circuits involving coherent qubits coupled via optical photons has yet to emerge.

4.2 Experimental approach

Our experimental approach, illustrated in Figure 4.1 a, makes use of a single atom trapped in the near field of a nanoscale photonic crystal (PC) cavity that is attached to an optical fiber taper [17]. The tight confinement of the optical mode to a volume $V \sim 0.4\,\lambda^3$, below the scale of the optical wavelength λ, results in strong atom-photon interactions for an atom sufficiently close to the surface of the cavity. The atom is trapped at about 200 nm from the surface in an optical lattice formed by the interference of an optical tweezer and its reflection from the side of the cavity (see Appendix B and Fig. 4.1a,b) Compared to transient coupling of unconfined atoms [12, 13], trapping an atom allows for experiments exploiting long atomic coherence times, and enables scaling to quantum circuits with multiple atoms.

We use a one-sided optical cavity with a single port for both input and output [87]. In the absence of intracavity loss, photons incident on the cavity are always reflected. However, a single, strongly-coupled atom changes the phase of the reflected photons by

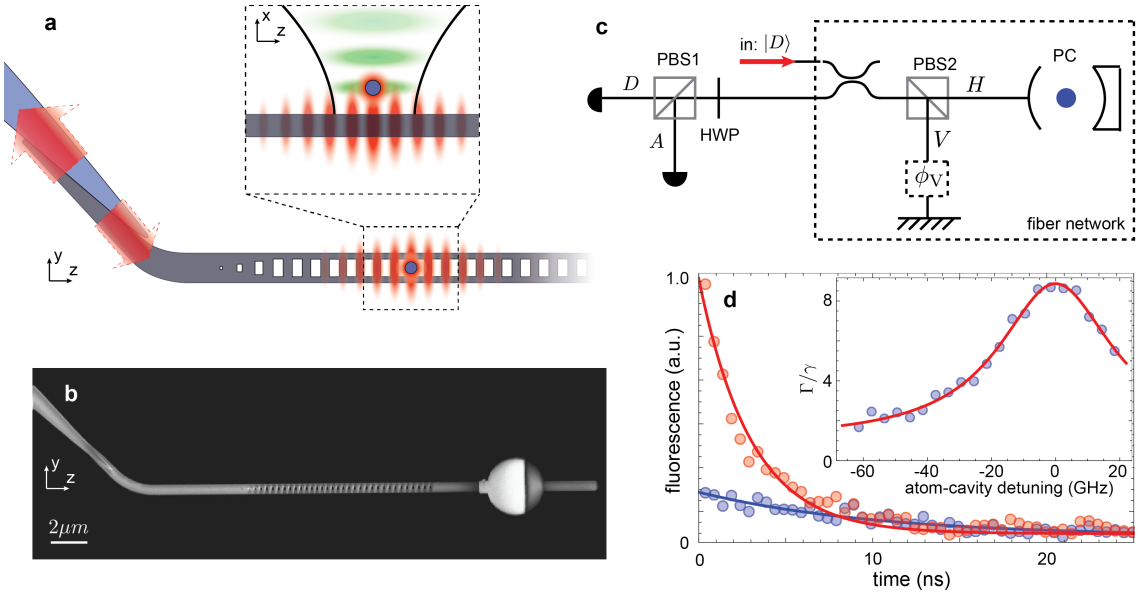

Figure 4.1: **Strong coupling of a trapped atom to a photonic crystal cavity. a.** A single ^{87}Rb atom (blue circle) is trapped in the evanescent field (red) of a PC (gray). The PC is attached to a tapered optical fiber (blue), which provides mechanical support and an optical interface to the cavity. The tapered fiber-waveguide interface provides an adiabatic coupling of the fiber mode to the waveguide mode. The inset shows the one-dimensional trapping lattice (green), formed by the interference of an optical tweezer and its reflection from the PC. The lattice is loaded with $> 90\%$ probability. **b.** Scanning electron microscope (SEM) image of a single-sided PC. The pad on the right-hand side is used to thermally tune the cavity resonance by laser heating. **c.** The PC is integrated in a fiber-based polarization interferometer. A polarizing beamsplitter (PBS2) splits the D-polarized input field into an H-polarized arm containing the PC and a V-polarized arm with adjustable phase ϕ_V. Using a polarizing beamsplitter (PBS1) and half wave plate (HWP) the outgoing D and A polarizations are detected independently. **d.** Excited-state lifetime at an atom-cavity detuning of 0 GHz (red) and -41 GHz (blue). The excited state lifetime is shortened to $\tau = \Gamma^{-1} = 3.0(1)$ ns from the free space value of $\gamma^{-1} = 26$ ns, yielding a cooperativity $\eta = 7.7 \pm 0.4$. The difference in the fluorescence signal at $t = 0$ for the two detunings is consistent with the change in cavity detuning. The inset shows the enhancement of the atomic decay rate versus atom-cavity detuning.

π compared to an empty cavity. More specifically, in the limit of low incident intensity, the amplitude reflection coefficient of the atom-cavity system is given by [99]:

$$r_{\mathrm{c}}(\eta) = \frac{(\eta - 1)\gamma + 2i\delta}{(\eta + 1)\gamma - 2i\delta} \tag{4.1}$$

where $\eta = (2g)^2/(\kappa\gamma)$ is the cooperativity, $2g$ is the single photon Rabi frequency, δ is the atom-photon detuning, and the cavity is taken to be resonant with the driving laser. In our apparatus, the cavity intensity and atomic population decay rates are given by $\kappa = 2\pi \times 25\,\mathrm{GHz}$ and $\gamma = 2\pi \times 6\,\mathrm{MHz}$, respectively. The reflection coefficient in Eq. 4.1 changes sign depending on the presence ($\eta > 1$) or absence ($\eta = 0$) of a strongly-coupled atom. If the atom is prepared in a superposition of internal states, one of which does not couple to the cavity mode (*e.g.* another hyperfine atomic sublevel), the phase of the atomic superposition is switched by π upon the reflection of a single photon. By also adding an auxiliary photon mode that does not enter the cavity (*e.g.*, an orthogonal polarization), this operation can be used to realize the Duan-Kimble scheme for a controlled-phase gate between an atomic and a photonic quantum bit [87]. The property of the atom-cavity system that a single photon and a single atom can switch each other's phase by π is the key feature of this work.

We quantify the single-atom cooperativity η by measuring the lifetime τ of the atomic excited state when it is coupled to the cavity. We excite the atom with a short (3 ns) pulse of light co-propagating with the optical trap and resonant with the $|5S_{1/2}, F = 2\rangle \rightarrow |5P_{3/2}, F' = 3\rangle$ transition (near 780 nm). The atomic fluorescence is collected through the cavity to determine the reduced excited-state lifetime $\tau = \Gamma^{-1}$, as shown in Fig. 4.1d, which yields the cooperativity $\eta = (\Gamma - \gamma)/\gamma$. Fitting a single exponential decay gives

$\tau = (3.0 \pm 0.1)$ ns, corresponding to $\eta = 7.7 \pm 0.3$ and a single-photon Rabi frequency of $2g = 2\pi \times (1.09 \pm 0.03)$ GHz.

4.3 Experimental results

To probe the optical phase shift resulting from the atom-photon interaction, we integrate the cavity into a fiber-based polarization interferometer, which converts phase shifts into polarization rotations (Figure 4.1c). The H-polarized arm of the interferometer contains the cavity, while the V-polarized arm is used as a phase reference. For an input photon state $|\psi_{in}\rangle$ in the polarization basis $\{|H\rangle, |V\rangle\}$, the state exiting the interferometer is given by $\mathcal{R}|\psi_{in}\rangle$, where $\mathcal{R} \equiv r_{\mathrm{V}} e^{i\phi_{\mathrm{V}}} |V\rangle\langle V| + r_c(\eta)|H\rangle\langle H|$ and r_{V}, ϕ_{V} are the amplitude and phase of the reflection of the reference arm. We choose the reflectivity r_V of the reference arm to match that of the empty (lossy) cavity (see Appendix B), such that in the absence of an atom, the light emerges in the incident polarization state $|D\rangle \equiv (|V\rangle + |H\rangle)/\sqrt{2}$. In the presence of an atom, for $\phi_V = 0$ and $\eta \gg 1$, input light exits the interferometer predominantly with the orthogonal polarization $|A\rangle \equiv (|V\rangle - |H\rangle)/\sqrt{2}$.

Figure 4.2a demonstrates the optical phase shift arising from an atom coupled to the cavity. A weak D-polarized probe field is applied at the interferometer input, and the output power in the A and D ports is recorded as a function of the reference phase ϕ_V. The phase of the reflected light is shifted by $(1.1 \pm 0.1)\pi$ relative to the case with no atom, and the visibility of the oscillation with ϕ_V is $(44 \pm 2)\%$ and $(39 \pm 2)\%$ in the A and D ports, respectively. By repeating this measurement for a range of atom-photon detunings δ, we observe a 2π change in the reflection phase across the atomic resonance (Figure 4.2b), in agreement with Eq. (4.1). For the data presented, the events where an atom was not present in the cavity (*e.g.* by escape from the trap) were excluded. The remaining

contributions to the reduced fringe visibility are imperfect balancing of the interferometer ($\sim$ 5%), atomic saturation effects ($\sim$ 10%), state-changing scattering processes that leave the atom in a different final state and therefore reveal which-path information in the interferometer ($\sim$ 20%) and thermal motion of the atom ($\sim$ 20%) (see Appendix B).

The saturation behavior of the atom-cavity system is examined in Figure 4.3a, which shows the fraction of the output power in the A and D ports as a function of the input power. We set the reference phase $\phi_V \simeq 0$ such that the A port is dark in the absence

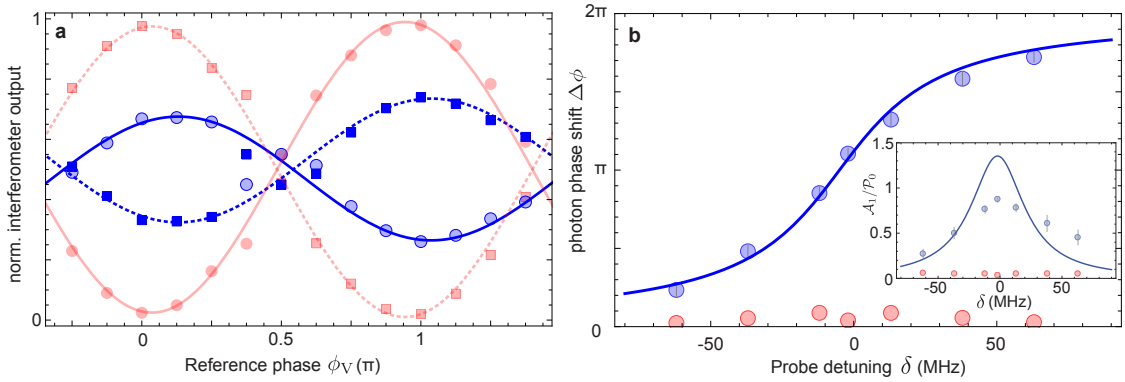

Figure 4.2: **Photon phase shift produced by a single atom. a.** Normalized interferometer output versus reference phase ϕ_V. The blue circles, blue squares, red circles, red squares correspond to $\mathcal{A}_1/\mathcal{P}_1$, $\mathcal{D}_1/\mathcal{P}_1$ (with atom) and $\mathcal{A}_0/\mathcal{P}_0$, $\mathcal{D}_0/\mathcal{P}_0$ (without atom) where $\mathcal{A}$ and $\mathcal{D}$ are the powers in the A and D output ports and $\mathcal{P} \equiv \mathcal{A} + \mathcal{D}$. The measurement is performed near resonance ($\delta = -2\,\mathrm{MHz}$) and the lines are sinusoidal fits resulting in a phase shift of $(1.1 \pm 0.1)\pi$. The maximum fringe visibility with and without an atom is $(44 \pm 2)\%$ and $(97 \pm 1)\%$, respectively. **b.** Measured phase shift versus detuning in the presence (blue) and absence (red) of an atom. The curve includes cavity losses in Eq. 4.1 (see Appendix B), and corresponds to a cooperativity of $\eta = 7.7$ and a small (5 MHz) offset from the free-space resonance. The inset shows the power in the D port normalized to the total power in the absence of an atom measured at $\phi_V = \pi$. The solid line is the expected amplitude corresponding to the fit of the phase. The expected increase in reflectivity in the presence of an atom ($\mathcal{P}_1/\mathcal{P}_0 > 1$) arises because the atom reduces the field amplitude in the lossy cavity (see Appendix B). In our experiment we observe $\mathcal{P}_1/\mathcal{P}_0 \simeq 1.2$. The error bars reflect $\pm 1\sigma$ statistical uncertainty.

of the atom. The distribution of the output is power-indepedent for low input powers, as expected for a linear system. At higher powers, the atomic response saturates and the output fraction at the A port decreases. The saturation becomes evident when the input photon rate approaches the enhanced excited state decay rate Γ, in agreement with theoretical predictions (see Appendix B). This nonlinearity results in different reflection phases for single photons and photon pairs. In a Hanbury-Brown-Twiss experiment, we measure the photon-photon correlation functions $g^{(2)}(\tau)$ at low input power. We observe strong anti-bunching of $g_A^{(2)}(0) = 0.12(5)$ and bunching of $g_D^{(2)}(0) = 4.1(2)$ in the A and D ports respectively, indicating that the atom-cavity system acts as an effective photon router by sending single photons into output A and photon pairs into output D [100].

To realize a quantum switch where the state of a single atom controls the propagation of many probe photons, we use two atomic hyperfine states, $|c\rangle \equiv |F = 2, m_F = 0\rangle$ and $|u\rangle \equiv |F = 1, m_F = 0\rangle$ (see Figure 4.4a) which can be coherently manipulated with microwaves. While the atom-photon interaction strength is similar for all of the sublevels in a given hyperfine manifold, the $F = 1$ levels (including $|u\rangle$) are effectively uncoupled because the probe is far-detuned from all optical transitions originating from this level. In Fig. 4.4b, we show the output signal at the A port for a D-polarized probe field with an atom prepared in $F = 1$ or $F = 2$. The switch is "on" and the input light goes mostly to the A port when the atom is in $F = 2$, while the switch is "off" and the A port is dark when the atom is in $F = 1$. We estimate that up to $\bar{n}_A \simeq 75$ photons could be transmitted to the A port in the "on" state before the atom is optically pumped out of the $F = 2$ manifold. In the experiments shown in Figure 4.4, a smaller number of photons ($\bar{n}_A = 6.2$) was used to increase the rate of data acquisition by allowing a greater number of measurements with the same atom. This photon number allows us to distinguish the switch state with an average fidelity of 95%.

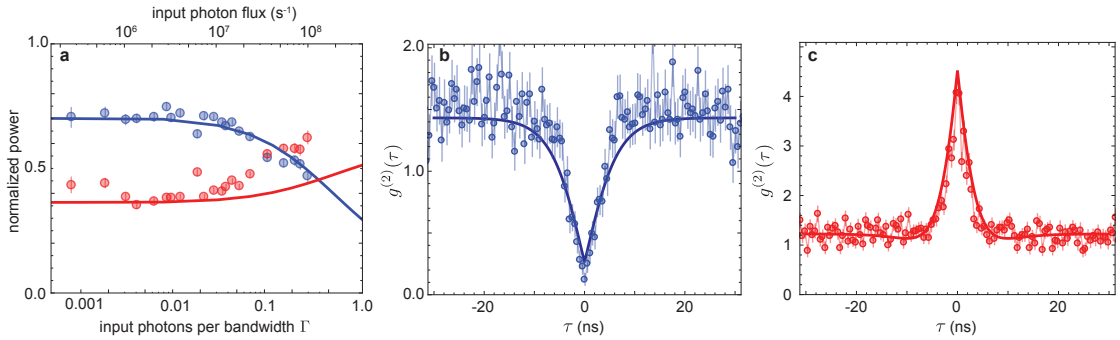

Figure 4.3: **Quantum nonlinear optics with the atom-PC system a.** Interferometer output as a function of the photon rate incident on the interferometer. The outputs $\mathcal{A}_1/\mathcal{P}_0$ (blue) and $\mathcal{D}_1/\mathcal{P}_0$ (red) are normalized to the case without an atom. The incident photon rate is normalized to the enhanced atomic decay rate $\Gamma = (\eta + 1)\gamma$. The interferometer is tuned such that port A is dark in the absence of the atom and the output in port A starts to saturate at a rate below one photon per bandwidth Γ. Unlike the data in Figure 4.2 and 4.4 these measurements were performed in the presence of the dipole trap which reduces $\mathcal{A}_1/\mathcal{P}_1$ at low driving intensities (see Appendix B). **b-c.** Photon-photon correlation functions $g^{(2)}(\tau)$ for the A (**b**) and D (**c**) ports. Port A shows clear anti-bunching with $g_R^{(2)}(0) = 0.12(5)$, while port D exhibits a strong bunching of $g_T^{(2)}(0) = 4.1(2)$. The solid lines in figures **a-c** are obtained from a model including inhomogeneous light-shift broadening arising from the dipole trap (see Appendix B). The error bars reflect $\pm 1\sigma$ statistical uncertainty.

As the effect of an atom on a photon and of a photon on an atom are complementary, it follows from Eq. 4.1 that a single photon can shift the phase of the coupled state $|c\rangle$ by π. This phase shift can be converted into a flipping of the atomic switch, $|c\rangle \leftrightarrow |u\rangle$, using an atomic Ramsey interferometer [94]. An atom is first prepared in the $|u\rangle$ state via optical pumping and rotated to the superposition $(|u\rangle + |c\rangle)/\sqrt{2}$ by a microwave $\pi/2$ pulse (see Appendix B). A single H-polarized "gate" photon flips the atomic superposition to $(|u\rangle - |c\rangle)/\sqrt{2}$. As reflection of the gate photon does not reveal the atomic state, the atomic superposition is not destroyed. Finally, a second microwave $\pi/2$ pulse rotates the atomic state to $|c\rangle$ or $|u\rangle$ depending on the presence or absence of the gate photon,

leaving the switch on (atom in $|c\rangle$) or off (atom in $|u\rangle$). A similar technique was recently explored for nondestructive photon detection in a Fabry-Perot cavity [10].

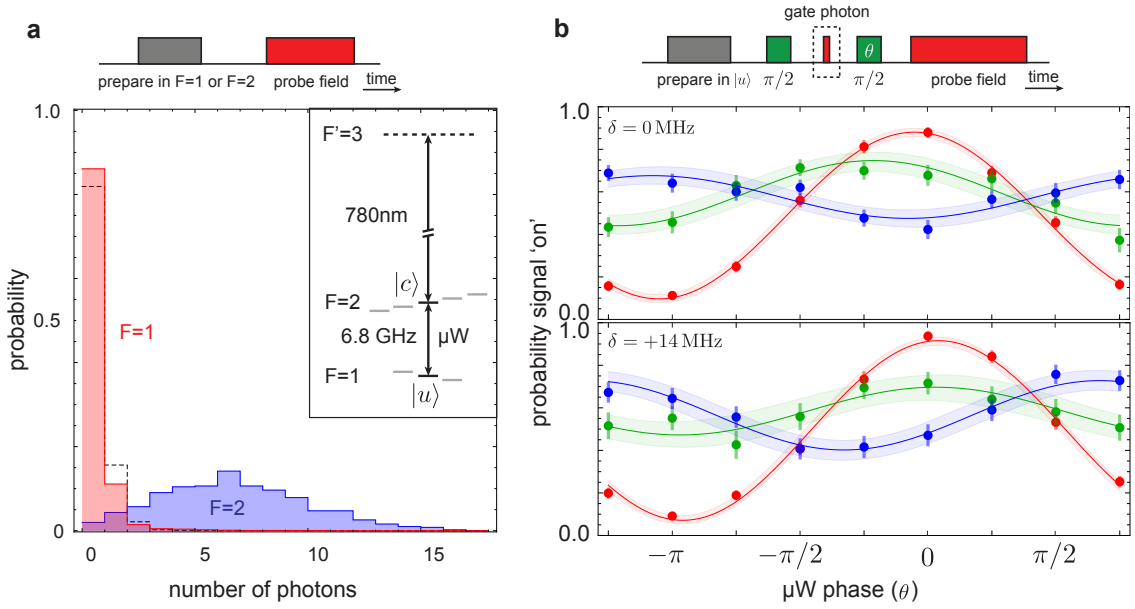

Figure 4.4: **Realization of a quantum phase switch a.** Number of probe photons detected in port A as a function of the internal atomic state. If the atom is in the $F = 2$ manifold the switch field is "on", thereby routing $\bar{n}_A = 6.2$ photons to port A. If the atom is absent (dashed line) or in the $F = 1$ manifold, $\bar{n}_A = 0.2$. The input photon number is the same in all cases, corresponding to a peak rate much smaller than Γ. The separation between the two distributions allows the switch states to be distinguished with 95% average fidelity. The inset shows the relevant levels for the quantum switch. The laser is tuned to the $F = 2$ to $F' = 3$ transition, which couples only to $|c\rangle$. **b.** (top) The switch sequence (see text). (bottom) The probability P_{on} of finding the switch "on", as a function of the phase θ of the second microwave pulse ($\delta = 0$ (top panel) and $\delta = 2\pi \times 14\,\mathrm{MHz}$ (bottom panel)). P_{on} is shown: without a gate field (P^0_{on}, red), conditioned on a gate photon (P^1_{on}, blue) and unconditioned (P^{uc}_{on}, green). The error bars reflect $\pm 1\sigma$ statistical uncertainty in the data, while the shaded region shows the range of curves with fit parameters within 1σ of the best fit.

In our measurement, we mimic the action of a single gate photon by applying a weak coherent field with $\bar{n} \approx 0.6$ incident photons and measuring the probe transmission con-

ditioned on the detection of a reflected gate photon at either interferometer output. Fig. 4.4c shows the probability P_{on} to find the switch in an "on" state as a function of the phase of the second microwave pulse. The dependence of P_{on} on the microwave phase when a reflected gate photon is detected shows that the superposition phase is shifted by $(0.98 \pm 0.07)\pi$. The atomic coherence is reduced but not destroyed. The absence of a phase shift in the unconditioned data (green curve in Fig. 4.4c) confirms that the switch is toggled by a single photon. The phase shift depends on the gate photon detuning: tuning the laser to $\delta = 2\pi \times 14\,\mathrm{MHz}$ results in a phase shift of $(0.63 \pm 0.15)\pi$, in good agreement with the detuning dependence of the photon phase shift (Figure 4.2b).

For an optimally chosen phase of the second microwave pulse, we find that the switch is in the "on" state with probability $P_{on}^1 = 0.64 \pm 0.04$ if a gate photon is detected, $P_{on}^0 = 0.11 \pm 0.01$ if no gate field is applied, and $P_{on}^{uc} = 0.46 \pm 0.06$ without conditioning on single photon detection. The finite $P_{on}^0 > 0$ without a gate field arises from imperfect atomic state preparation and readout fidelity (see Appendix B). P_{on}^1 is also affected by the finite probability for the gate field to contain two photons, of which only one is detected. This results in a decrease (increase) of P_{on}^1 (P_{on}^{uc}) by about 20% in a way that is consistent with our measurements (see Appendix B). We attribute the 8 % positive offset in P_{on}^1 and P_{on}^{uc} to spontaneous scattering events of the gate photon, which cause atomic transitions to a final state other than $|c\rangle$ within the $F = 2$ manifold. Lastly, we estimate that fluctuations in η arising from thermal motion do not change P_{on}^1 by more than 10%, since the atom-photon interaction scheme used here [87] is inherently robust to variations in η for $\eta \gg 1$. The imperfect fringe visibility in Figure 4.2 and 4.4, due to the technical imperfections discussed above, can be improved by better atomic state preparation, alignment of the cavity polarization with the magnetic field defining the quantization axis, and improved atom localization. The fringe visibility does not directly depend on the coop-

erativity and perfect fringe visibility should be achievable if these parameters are chosen optimally; however, the probability of gate photon loss is reduced inversely with cooperativity (see Appendix B).

4.4 Outlook

Our experiments open the door to a number of intriguing applications. For instance, efficient atom-photon entanglement for quantum networks can be generated by reflecting a single photon from an atom prepared in a superposition state. The quantum phase switch also allows for quantum non-demolition measurements of optical photons [9, 10]. With an improved collection efficiency of light from the PC cavity and reduced cavity losses, it should be possible to make high-fidelity non-demolition measurements of optical photon number parity to create non-classical "cat"-like states [101], with possible applications to state purification and error correction. Most importantly, the scalable nature of both nanofabrication and atomic trapping allow for extensions of this work to complex integrated networks with multiple atoms and photons.

Chapter 5

Efficient fiber-optical interface for nanophotonic devices

5.1 Introduction

The field of nanophotonics [102] has opened new avenues for applications such as nanophotonic integrated circuits [103, 104], sensing [105–108] and scalable quantum information processing [63, 109, 110]. In particular, sub-wavelength confinement of optical fields has led to significant advances in strong light-matter interaction at the single quantum level [18, 111]. A major challenge in the field is to efficiently integrate the nanophotonic devices with conventional optical fiber networks. This challenge arises from a large mismatch between the size of the fundamental mode of the optical fiber and that of the optical modes of nanophotonic devices. This mismatch has to be bridged in order to achieve efficient coupling. Highly efficient coupling is crucial for applications such as quantum repeaters [84] or quantum networks [63] since the performance of these systems, in the limit of many nodes, deteriorates near-exponentially with photon loss between individual nodes. Additionally, highly efficient coupling enables distribution of non-classical states of light which are extremely fragile to photon loss.

A wide range of coupling techniques are currently being explored, including grating coupling [103] and end-firing from macroscopic fibers [112] where coupling efficiencies

of up to 70-80% to on-chip waveguides have been achieved. More recently, on-chip photonic waveguides have been coupled to the waist of a biconical fiber taper [113] with an efficiency as high as 95%.

In this chapter, we demonstrate a novel method to efficiently couple a single mode fiber to a dielectric nanophotonic waveguide using a conical tapered fiber tip. The coupling is based on an adiabatic transfer of the fundamental mode of the optical fiber to the fundamental mode of the nanophotonic waveguide. Our method can be applied to general dielectric one-dimensional waveguides. In contrast to biconical tapered fibers [113], our devices are single-sided, thereby offering alternative geometries and mechanical support for nanophotonic devices [17, 18] and opening the door for new applications.

5.2 Adiabatic coupling

Adiabatic mode transformation is widely used to obtain efficient power transfer through nonuniform optical waveguides [114]. The key idea is to change the waveguide cross-section slowly along the propagation direction of the light such that all the optical power remains in a single eigenmode of the composite waveguide, while the coupling to other modes is suppressed. More specifically, two eigenmodes ν and μ with effective indices n_ν and n_μ have a characteristic beat length given by $z_b = 2\pi\lambda/(n_\nu - n_\mu)$, where λ is the wavelength in vacuum. In order to achieve adiabatic transfer, the characteristic length scale z_t over which the waveguide dimensions change has to be large compared to z_b [115]. While the exact coupling strength depends on the details of the spatial mode profiles, we design our devices according to this intuitive length-scale argument and use numerical simulations to verify the design.

Figure 5.1a shows a schematic of a typical device. A fiber is tapered down to a coni-

cal tip and an inversely tapered silicon nitride (Si_3N_4) waveguide is attached over a length of 7.5 μm. In what follows, we separate the device in two regions (see Fig. 5.1a): the adiabatic fiber-waveguide coupler (I) and the fiber taper (II), separated by a plane P at the start of the waveguide. In both regions we design our devices according to the adiabaticity criterion by ensuring $z_t > z_b$. In region I the optical modes of the fiber and waveguide are coupled through their evanescent fields and form a set of hybridized supermodes. z_b is determined by the difference between the effective indices of the fundamental supermode and the higher order supermode with the closest propagation constant (in this case radiation mode) while z_t is limited by the length of the coupling region. In region II the fiber is tapered down from a standard single mode fiber, adiabatically transforming the core-guided HE11 mode to a cladding-guided HE11 mode. We ensure that the local taper angle $\Omega(z) \equiv \rho(z)/z_t \ll \rho(z)/z_b$, where $\rho(z)$ is the fiber radius at position z along the taper. In region II z_b is determined by the coupling of the fundamental fiber mode to the nearest higher-order mode. We follow the conventional design for biconical adiabatic fiber tapers where recently transmission efficiencies as high as 99.95 % [116] have been achieved (see also [115, 117] for details).

If the waveguide is tapered such that its cross section is zero in the plane P (as that shown in figure 5.1), then the transition from region I to region II is smooth, and needs no special attention. However, for a waveguide with a non-vanishing cross-section at P (such as the rectangular waveguide shown in figure 5.1d), the refractive index cross-section changes discontinuously, and we must evaluate what happens at this point. We approximate the power transfer through P by projecting the fundamental fiber mode on the fundamental supermode at P. This projection should be close to unity to have efficient coupling. This can be achieved by placing the transition point such that the diameter of the fiber is much larger than that of the waveguide, so the sudden appearance of

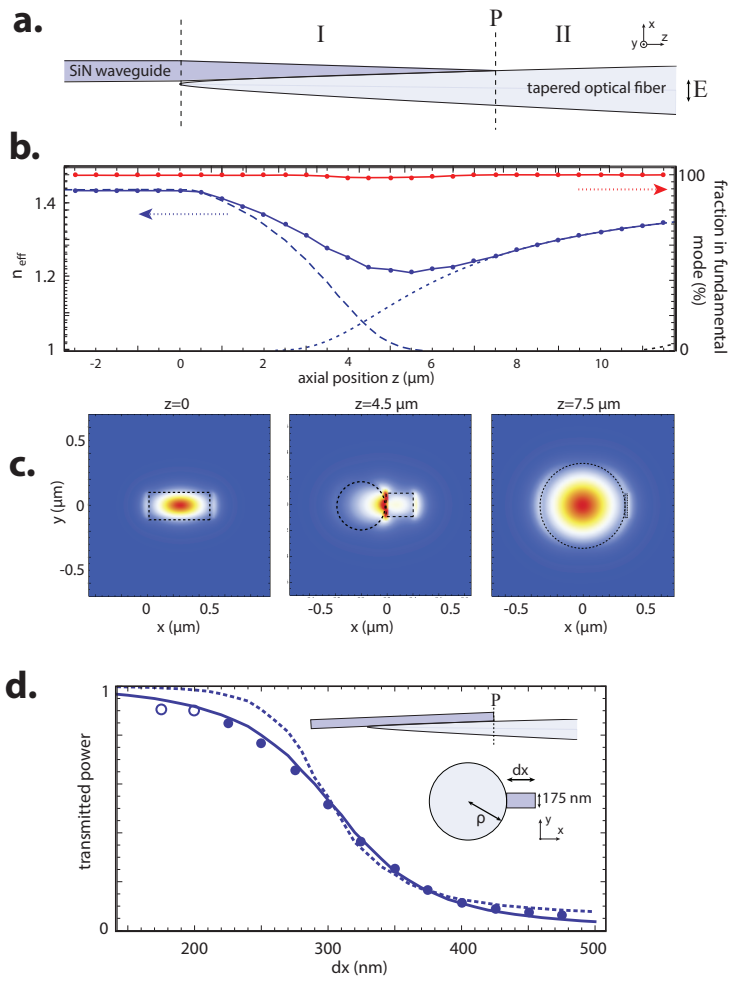

Figure 5.1: **Adiabatic transfer between fiber and waveguide modes. a.** Schematic of the fiber-waveguide coupling. The fiber (right) has a conical shape and is attached to a tapered Si_3N_4 rectangular waveguide (left), and we consider modes polarized along $\hat{x}$. **b.** Effective index n_{eff} of the fiber and waveguide modes for an opening angle of the fiber (waveguide) of 5° (4°). The blue dotted (dashed) lines are the separate fiber (waveguide) modes and the blue solid line corresponds to the fundamental supermode of the combined structure. The red line shows the power in the fundamental supermode obtained from an FDTD simulation of the coupler (see text). **c.** Cross sections of $|E|^2$ obtained from the FDTD simulation at various points along the coupler. *(continued on next page)*

Figure 5.1: *(continued)* **d.** The fraction of the power in the fundamental supermode of the combined structure as a function of the waveguide width dx, obtained from a mode decomposition (solid line). The transmission through a tapered coupler (see *inset*) obtained with an FDTD simulation (circles) agrees well with the estimated transmission obtained from the mode decomposition. The two data points for $dx \leq 200\,\mathrm{nm}$ (open circles) are calculated using a shallower fiber angle (2°) to ensure $z_t > z_b$. The dotted line shows the same geometry except that the fiber and waveguide are in contact on the xz-plane instead of the yz-plane. The fiber-waveguide cross-sections used for this simulation are shown in the *inset*, $\rho = 450\,\mathrm{nm}$.

the waveguide represents a minimal perturbation to the combined structure.

We next verify these design criteria using Finite Difference Time Domain (FDTD) simulations of complete structures. Figures 5.1b and 5.1c show simulations for the device presented in figure 5.1a. We consider a conical fiber with an opening angle $d(2\rho)/dz = 5°$ and a $dy = 175\,\mathrm{nm}$ thick Si_3N_4 waveguide with a taper angle $d(dx)/dz = 4°$ to a width of $dx = 500\,\mathrm{nm}$. We focus on TE-polarized ($\hat{x}$) modes, but we have verified that the same principles apply to TM-polarized modes as well. Figure 5.1b shows the effective indices of the fiber mode, the waveguide mode and of the hybridized mode of the combined structure (supermode). For this geometry, the latter has an effective index of $n_{\mathrm{eff}} > 1.2$ over the entire length of the coupler. The combined structure supports only one other mode of orthogonal polarization, which does not couple to the fundamental mode via the perturbation introduced by the taper. The relevant beat length is therefore set by the fundamental supermode and the free space modes ($n_0 = 1$), giving $z_b \simeq 4\,\mu\mathrm{m}$. We chose the length of the coupler ($z_t \simeq 7\,\mu\mathrm{m}$) to be longer than z_b. In order to verify adiabaticity we perform a FDTD simulation (see figure 5.1b,c), in which we excite the fiber taper at $z = 11\,\mu\mathrm{m}$ with the fundamental HE11 mode polarized along $\hat{x}$ and propagating along $-\hat{z}$. We decompose the optical fields in the basis of local eigenmodes of the combined fiber-waveguide structure and find that essentially all the optical power ($> 99\,\%$) remains

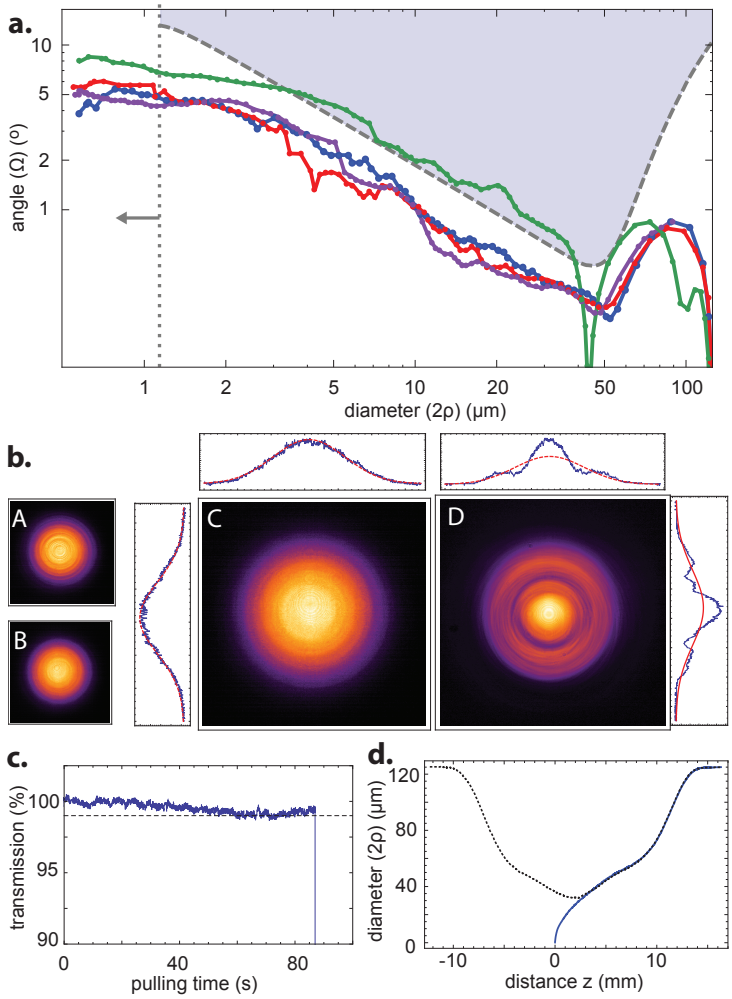

Figure 5.2: **Characterization of adiabatic tapers. a.** The fiber angle as a function of the local fiber diameter along the taper axis z. The dashed line and shaded area indicate the adiabaticity criterion $z_t > z_b$ as discussed in the text. Fiber tapers which have a profile below the dotted line are expected to be adiabatic. For a diameter smaller than 1.1 μm the HE12 mode is cutoff. The taper profiles for 4 tapers (blue (A), red (B), purple (C) and green (D)) are shown. **b.** Far field mode profiles. Tapers A, B and C show Gaussian profiles, while taper D has clear contributions from higher order modes. For tapers C and D cuts through the center of the profiles are shown together with a Gaussian fit. **c.** The transmission versus pulling time of a taper similar to A-C, the dashed line indicates 99% transmission. The sudden drop in transmission at $\simeq$ 87 s arises from the fast pull by the electromagnetic coil. *(continued on next page)*

Figure 5.2: *(continued)* **d.** The taper profile of taper C (blue) and of a biconical taper (dashed) using the same pulling parameters but without pulsing the electromagnet to create the tip.

in the fundamental mode across the complete structure.

In the case of a rectangular waveguide (Figure 5.1d), we model the sudden onset of the waveguide by decomposing the fundamental fiber mode in the basis of supermodes of the combined structure. This decomposition is performed using the fields of the eigenmodes of the fiber and the combined structure which we obtain using the MIT Photonic Bands (MPB) mode-solver [118]. To verify that the projection indeed describes the power transfer accurately, we compare the mode decomposition results with FDTD simulations. Figure 5.1d shows the power in the fundamental supermode of the combined structure as obtained from the mode decomposition and from an FDTD simulation for a rectangular Si_3N_4 waveguide with varying width dx and a fiber with radius $\rho = 450\,\mathrm{nm}$. We find that the loss of transmission through the coupler obtained from the FDTD simulation is well described by the mode decomposition. For the simulated conditions the losses can be made small for waveguide dimensions below 200 nm.

5.3 Design and fabrication

We next discuss the optimization and characterization of the tapered fiber tips in region II. For our experiments we use single mode fiber (Thorlabs 780HP), with a $4.4\,\mu\mathrm{m}$ ($125\,\mu\mathrm{m}$) core (cladding) diameter, and we optimize our design for a wavelength of $\lambda = 780\,\mathrm{nm}$. Figure 5.2a shows the critical angle ($\Omega_c(z) = \rho(z)/z_b(z)$) for achieving adiabatic propagation of the HE11 mode. When the fiber diameter is large ($d > 50\,\mu\mathrm{m}$), this angle is determined by the coupling between the HE11 core-guided mode and a number

of cladding-guided modes. For $d < 50\,\mu$m, the fundamental mode becomes the HE11 cladding-guided mode, and the adiabatic criterion is determined by coupling between this mode and the next highest mode of the same azimuthal order, HE21.

We fabricate fiber tapers using a conventional heat-and-pull setup [119, 120] where the fiber is heated using an isobutane torch (140 mL/min flow), with an effective flame length of $L = 4.3$ mm. The flame is continuously brushed back and forth to heat the fiber over a variable length, which is adjusted during the pulling to obtain the desired fiber profile (see Refs. [119, 121]). After creating a 24 mm long biconical fiber taper with a minimum diameter of $\sim 30\mu$m, we apply a fast pull to one of the fiber clamps, which quickly (~ 10 ms) pulls one end of the fiber out of the flame, creating a 14 mm long fiber taper with a conical tip (see figure 5.2d). The fast pull is produced by an electromagnet from the read/write head of a computer hard disk. A short current pulse through the electromagnet results in a constant acceleration of the fiber over the relevant time scale, creating a smooth fiber tip which is well described by a parabolic shape at larger fiber diameters and a constant opening angle over the last few tens of microns. We find that the acceleration changes linearly with the applied current over a range of 17 m/s^2 to 46 m/s^2. We typically use an acceleration of 33 m/s^2. By optimizing the heat-and-pull-parameters we realize the requirements of the taper angle for large diameters, while the electromagnet current and fiber diameter at which the pulse is applied controls the fiber taper angle at smaller diameter. We note that the resulting parabolic shape of the fiber taper conveniently has the same scaling ($\Omega \sim 1/\rho$) as the adiabaticity criterion at the relevant range of fiber diameters ($2 - 50\,\mu$m, see figure 5.2a). Additionally, since our fiber tips have subwavelength dimensions only over a length of $\sim 10\,\mu$m, the requirements on the cleanliness of the flame and the fabrication environment are less stringent than those for creating efficient biconical tapered fibers [116, 120].

5.4 Characterization

We characterize our devices with several measurements. First, we measure the taper profiles to ensure the local angle is smaller than the critical angle set by the adiabaticity condition. Figure 5.2 shows three fibers (A, B, C) which are made under the same conditions, while fiber D is made using different pulling parameters for the purpose of illustrating the performance of a sub-optimal fiber taper. In figure 5.2a we show the fiber profiles for each fiber, which are measured using optical and scanning electron microscopy (SEM). Fibers A, B and C show nearly identical profiles which satisfy the adiabaticity criterion, indicating that our fabrication method yields reproducible fiber tapers. Fiber D has a somewhat steeper angle for fiber diameters around $\sim 3 - 30\,\mu$m and is therefore expected to be non-adiabatic. Second, in figure 5.2b we show the far-field profiles of the fiber mode imaged directly on a CMOS camera. The optical modes of fibers A, B, C are all nearly Gaussian, indicating that at the end of the taper, most of the power is in the fundamental HE11 mode. Fiber D appears to have light leaving the tip in several spatial modes, in agreement with our expectation that this taper does not match the adiabaticity criterion. To quantify the single mode character of the profiles we calculate the coefficient of determination (R^2) of the Gaussian fits, resulting in $R^2 = 0.98, 0.99, 0.99, 0.87$ for tapers A, B, C and D, respectively. We find this method of measuring the far field profiles to be a very fast, sensitive and reliable for verifying the single mode character of our fiber tips. In figure 5.2c, we show the transmission through the fiber during the pulling process, and observe that it is greater than 99% until the fast pull is applied.

After confirming that our fiber tapers support adiabatic propagation to the tip, we measure the coupling efficiency (η_c) to a tapered Si_3N_4 waveguide (see Appendix C for details of the device fabrication). The waveguide we use contains a photonic crystal sec-

tion, which is highly reflective ($R \approx 1$) for frequencies within the optical bandgap, and we use this reflection to characterize the coupling efficiency by looking at the returned power that has passed through the fiber-waveguide coupling two times. We measure the reflected power P_{r} and divide it by the power P_{in} in the fiber before the taper is pulled (see Fig. 5.3a). This normalized reflection is given by $P_{\mathrm{r}}/P_{\mathrm{in}} = \eta_c^2 \eta_m \eta_{bs} \eta_{FC}$, where η_{bs} and η_{FC} are the fiber beamsplitter and FC-FC coupling efficiencies and η_m is the Bragg mirror reflectivity. Figure 5.3d shows measurements of the coupling efficiency for waveguide angles of $2^\circ \leq \alpha \leq 8^\circ$ and for rectangular waveguides with a width ranging from: $100 < dx < 250\,\mathrm{nm}$, all waveguides have a $dy = 175\,\mathrm{nm}$ thickness. For all of these measurements the, the waveguides are only attached to the substrate on one side (opposite the fiber coupling), to allow the waveguide to move slightly to contact the fiber. We observe that the coupling efficiency for most of these devices is $\geq 95\,\%$, with a maximum value of $\eta_c = 0.97(1)$. The coupling efficiencies for $dx \leq 150\,\mathrm{nm}$ are slightly lower, consistent with a not fully adiabatic coupler ($z_b > z_t$) since for decreasing waveguide width z_b increases while in our measurement we keep z_t constant. In comparison, we observe coupling efficiencies of $\eta_c \simeq 0.5 - 0.6$ for fiber tips with parameters such as fiber D.

Similar coupling efficiencies can be achieved with waveguides that are removed from the surface and attached to the optical fiber taper in mid-air (as used in our experiments described in Chapters 3 and 4). A typical device attached in free space is shown in figure 5.3c for which we measure a coupling efficiency of $\eta_c = 0.96(1)$.

5.5 Characterization of spurious reflections

In addition to coupling efficiency, another important parameter characterizing the fiber-waveguide interface is spurious reflections. In addition to interfering with measurements

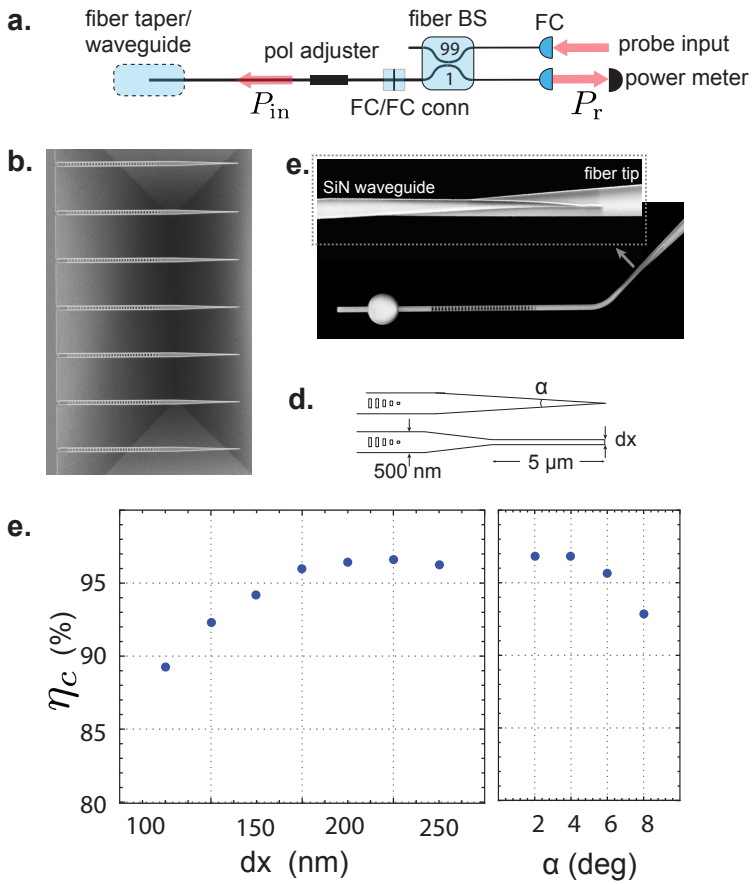

Figure 5.3: **Coupling to photonic crystal waveguide cavities. a.** Setup to measure fiber-waveguide coupling efficiency. A tunable probe laser is coupled weakly to the fiber connecting to the device using a 99:1 fiber beamsplitter. The polarization at the waveguide is adjusted by means of a fiber polarization controller and the light is in and out coupled of the fiber network using fiber collimators (FC) **b.** SEM image of an array of singly-clamped photonic crystal waveguide cavities used for on-chip measurements. **c.** SEM image of a photonic crystal cavity attached to the fiber tip, *inset* shows a zoom of the fiber-waveguide coupler. **d.** Schematic of the various waveguide geometries. **e.** Coupling efficiencies for a range of waveguides; the devices are either a tapered waveguide with an opening angle α or rectangular waveguides with a varying width dx and $5\,\mu$m long before adiabatically expanding to the photonic crystal cavity. All waveguides are 175 nm thick and attached to the chip as in panel **b**.

of the coupling efficiency, they are also problematic for applications that are sensitive to background light or multipath effects. To characterize spurious reflections in our coupler we perform a measurement using a photonic crystal waveguide containing a two-sided defect cavity, for which we expect $R \approx 1$ on resonance but $R = 0$ on resonance. We choose a low quality factor ($Q \simeq 2000$) in order to minimize the effect of cavity losses and detach the cavity from the chip to avoid additional reflections from the chip. For the device measured in Fig. 5.4, we observed a coupling efficiency of $\eta_c = 0.87$ and an on-resonance reflection of $2.0(4) \times 10^{-3}$, which provides an upper bound on spurious reflections from other parts of the taper or waveguide. Additionally, we do not observe any reflection ($0.1(3) \times 10^{-3}$) of the fiber tip when no cavity is attached. With TM polarized light in similar devices, we have measured a reflection of $4(1) \times 10^{-3}$ (at these frequencies, there is no bandgap for TM light).

5.6 Methods

For all measurements we assume perfect reflection from the Bragg mirror ($\eta_m \equiv 1$) and we correct for the independently calibrated beamsplitter ratio ($\eta_{bs} = 0.99$) and the FC-FC fiber coupling (with a typical value of $\eta_{FC} = 0.89$). We note that our results for η_c are conservative since we observe a small amount of scattering from the entrance Bragg mirror (implying $\eta_m < 1$) and did not account for propagation losses through the $\simeq 5\,\mathrm{m}$ of fiber. We estimate these combined losses to be on the percent level, however, our current method does not have sufficient accuracy to determine η_c to a higher precision.

We position the fiber on the waveguide by mounting the fiber at an angle of $\sim 10 - 20^\circ$ to the chip surface and aligning it under an optical microscope using a micrometer stage with fine piezo adjustment. The fiber and waveguide stick when brought together,

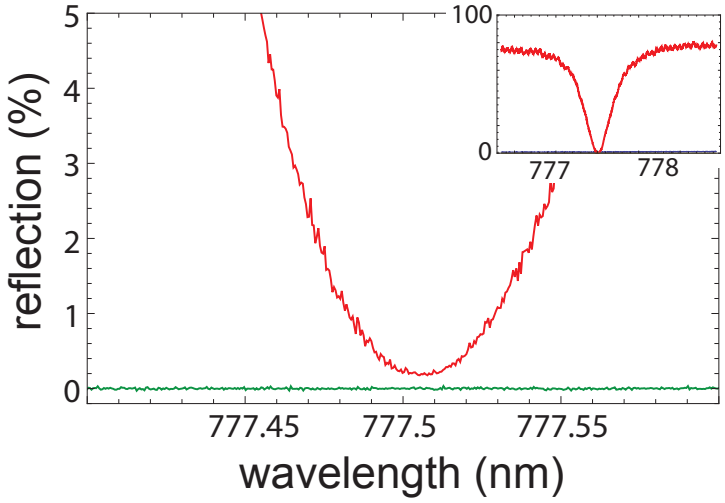

Figure 5.4: **Spurious reflections from coupler.** Reflection spectrum of a two-sided cavity (*Inset* shows full spectrum) for TE-polarized light (red) and for the bare fiber taper without a cavity attached (green). The cavity reflection should be zero on resonance, so the remaining reflected light gives an upper bound on spurious reflections from the fiber taper and other parts of the waveguide.

allowing stable alignment to be maintained for long periods of time. They can be released from each other by pulling them apart with the translation stage, apparently without damage. While we have not investigated the mechanism of the sticking, we note that "stiction" is very common and has been extensively studied in the context of micro- and nano-mechanical systems.

We obtain the optimal fiber-waveguide coupling by sticking them together and then sliding the fiber along the waveguide axis to fine-tune the position while monitoring the reflected power. Optimal coupling is typically achieved by lifting the fiber up slightly after contacting it to the waveguide, which we believe allows the waveguide to bend and better conform to the shape of the fiber taper. The procedure to detach cavities from the chip and attach them to the fiber taper is as follows (see also Appendix A): we break

off and pick up a waveguide using a tungsten tip and transfer it to the fiber tip in free space using three axis translation mounts for both the fiber and tungsten tip. We move the waveguide using the tungsten tip while optimizing for optimal reflection.

5.7 Outlook

We have presented a method for highly efficient fiber coupling to nanophotonic waveguides. Our measurements indicate coupling efficiencies as high as 97(1)% for a range of devices. These results open the door to a range of unique applications in quantum optics and nano-photonics. In particular, in combination with our recent results demonstrating strong coupling of a single atom to photonic crystals [17, 18], efficient coupling to fibers can enable the creation of highly non-classical Schrödinger cat states of light [101] and realization of efficient protocols for scalable quantum networks [63]. Moreover, the flexible geometries as well as the fiber-based mechanical support for nanophotonic devices, allowed by this approach open the door for new applications in nanoscale biosensing [107, 108, 122].

Chapter 6

Outlook

There are several major directions that this work could take in the future. The first application, which is implicitly the subject of most of the work we have already done, is to quantum networks. In the simplest form, this could mean using single atoms in cavities as quantum memories for a quantum repeater, with photon-mediated gate operations between two atoms in the same node [123] used to perform deterministic entanglement swapping [82]. One can also imagine more complicated schemes where multiple atom-atom or atom-photon gates are used to implement more sophisticated error correction.

The second direction is quantum simulation, inspired by the large body of work on realizing many-body quantum dynamics with trapped ultracold atoms [124]. An outstanding goal in this field is to produce atom-atom interactions that are stronger and longer-ranged than what is possible with superexchange [125], and also for these interactions to be long-range or variable-range. There is ongoing work to achieve this with ultracold dipolar molecules [126] and Rydberg atoms [127], as well as with photons in optical cavities [128]. It is possible that atoms trapped near nanophotonic structures could play a role in this field, with the particular advantage that the tunable dispersion properties of photonic crystal waveguides allows the interaction properties to be adjusted [129, 130].

There are abundant challenges on both frontiers, but none of them are fundamentally insurmountable. In the case of quantum networks, improvements to the atomic qubit coherence will be necessary (it is currently limited by the deep optical potential in several ways), as well as the lifetime of the atoms in the trap and the duty cycle with which they can be maintained there. In the case of quantum simulation, the trapping techniques will have to be revised to be able to trap much larger arrays of atoms near the surface, and new fabrication, tuning and characterization methods may be needed to produce larger arrays of photonic crystals. In both cases, there would be a benefit from improved cooperativity. As outlined above, the cooperativity can be expressed as $\eta = \frac{3}{4\pi^2}\frac{Q}{V} \times f$. For the structures we have already built, Q approaches 10^6 and $V < 0.5$, which is essentially state-of-the art, and should give $\eta > 10^5$. However, we trap the atoms at a position where f is less than $1/500$, and because the atom moves around it is on average worse and sometimes zero. Although it is probably possible with continued technological improvements to get more out of Q, there is also a very significant advantage to improving the localization of the atom and moving it closer to the surface or into the holes, where f can be 1.

Appendix A

Apparatus and methods used for the experiments presented in Chapter 3

A.1 Experimental apparatus and protocol

Our apparatus (depicted schematically in Fig. A.1) consists of a single stainless steel ultra-high vacuum (UHV) chamber housing a vapor-loaded ^{87}Rb magneto-optical trap. The optical tweezer trap is formed at the focus of an aspheric lens with a numerical aperture NA = 0.5 and a design wavelength of 780 nm. The lens itself is used as a vacuum window, avoiding aberrations and distortion from additional surfaces. To achieve this, it is glued (Varian TorrSeal) in a mount on a stainless steel edge-welded bellows segment, which is mounted to a standard vacuum flange on the other end. This arrangement has the additional benefit that the lens can be positioned using air-side translation stages, over a range of several cm along the optical axis (with a piezo for fine adjustment), and several mm in the other two directions. The optical tweezer position can be rapidly and precisely adjusted over a smaller range in a single plane using a scanning galvanometer mirror, as performed previously in [15]. The optical setup is discussed in more detail in Fig. A.1.

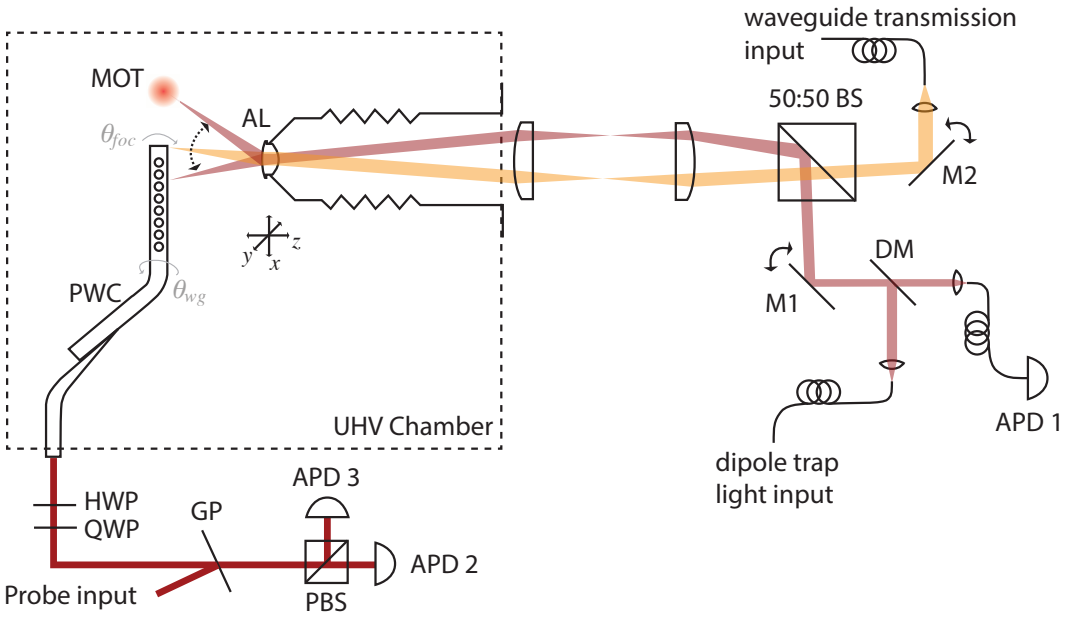

Figure A.1: **Schematic drawing of the apparatus** The core of the apparatus is a homebuilt two-channel scanning confocal microscope with a focal plane inside an ultra-high vacuum (UHV) chamber containing a MOT and the PWC. The aspheric lens (AL) is the microscope objective. Scanning mirrors (M1: Cambridge NanoTech 6215, M2: Physik Instrumente S-330.45) allow two beams to be independently positioned in the same focal plane; the beams are combined on the beamsplitter 50:50 BS. The M1 path steers the dipole trap beam and is moved back and forth between the MOT region and the waveguide. Fluorescence from the atom is collected along the same path into a single mode fiber, separated from trap light using a dichroic mirror (DM) and then detected on an avalanche photodiode (APD1). The M2 path is focused on the tip of the waveguide and is used to in-couple light for the transmission measurements shown in Figure 3.4 of the main text. The fiber connected to the PWC leaves the UHV chamber through a fiber feedthrough, and a series of waveplates is used to correct for birefringence in the fiber, such that (horizontal, vertical) polarizations referred to the optical table are coupled to $(\hat{y},\hat{z})$ polarizations in the PWC. The optical pumping light used for the measurements in Figure 3.3 of the main text is coupled in on a glass plate (GP) at a small angle of incidence. Fluorescence from the atom, and the cavity transmission signal from Figure 3.4, are detected on APD2/3, which detect light originating in the PWC $\hat{y}/\hat{z}$ modes separately. Only the $\hat{z}$-polarized signal is shown in Fig. 3.4, since this is the polarization of the cavity mode near the Rb resonance frequency.

The nanostructure to be studied is mounted on the end of a tapered optical fiber tip and inserted into the chamber through an airlock with a fiber feedthrough. After installing a new nanostructure, the position of the MOT is adjusted to bring it close to the fiber tip, by changing the alignment of the cooling lasers. The aspheric lens is also adjusted to focus on the fiber tip and center it in the field of view.

A typical experimental sequence begins with the optical tweezer at the loading position, 40μm away from the fiber tip. This distance is necessary to reduce the amount of background signal on the APD arising from the cooling and repumping lasers scattering off of the fiber and nanostructure. This background must be low enough that the fluorescence from single atoms can be reliably detected (signal sizes are typically $50 - 100 \times 10^3$ counts/second). The fluorescence is monitored in real-time; once it has risen above a threshold indicating the presence of a single atom, the cooling and repumping beams are extinguished to prevent further loading. Then, a period of Raman sideband cooling is performed to cool the atom near the ground state of the optical tweezer [16, 56]. After cooling, the tweezer is translated quickly (2μm/ms) from the loading point to a waypoint several microns from the nanostructure, and from there moved more slowly ($\leq 1\mu$m/ms) to the final position over the nanostructure. This entire sequence, from loading an atom to positioning it over the nanostructure, takes about 200 ms.

Once positioned over the nanostructure, we perform experiments as discussed in the main text. In cases where the final observable is the hyperfine state of the atom, this measurement is performed by bringing the atom back to the loading point using the same motion sequence in reverse, and removing the atom if it is in $F = 2$ by applying an intense 5μs push-out pulse resonant with the $F = 2 \rightarrow F' = 3$ transition. The presence of the atom is then detected by turning on the cooling and repumping beams again and recording fluorescence for 20 ms. A high level indicates that the atom is still present and

was therefore in $F = 1$. The same sequence can be applied without a push-out pulse to measure the total survival probability instead, from which the $F = 2$ population can also be extracted. Imperfections in the push-out process, depolarization from off-resonant scattering of the dipole trap laser, and vacuum losses limit the fidelity of this read-out, such that the contrast of the state detection is only about 80%, for experiments conducted with the PWC. For the experiments with the fiber alone presented in Fig. 3.2, the vacuum losses were significantly higher, resulting in slightly less than 50% contrast.

A significant challenge in this experiment is correcting for thermal or other drifts that cause the PWC and the two optical paths (M1 and M2, see Fig. A.1) to move with respect to each other. To perform this correction this, we pause the experiment every 5 minutes and shine a small amount of light at the frequency of the dipole trap laser into fiber holding the PWC; this light propagates through the PWC and is scattered into free space at the tip. While the light is applied, we scan the mirrors M1 and measure the intensity coupled back into the single mode fiber that normally supplies the dipole trap light. This image allows us to determine the position of the tip of the waveguide in the coordinate system of the mirror M1, so we can position the dipole trap accurately. Drift in the $\hat{z}$ direction is measured by taking several such images in different focal planes and cross-correlating them with reference images. The M2 path is corrected separately using a similar technique. Without this feedback, the drift rate of the PWC in the M1 coordinate system is typically 100 nm/hr in x, y and 300 nm/hr in z.

A.2 Photonic crystal device fabrication and characterization

A.2.1 General procedures

To fabricate our silicon nitride PWCs, we begin with $\langle 100 \rangle$ Si wafers with 200 nm of LPCVD stoichiometric ($n = 2.0$) silicon nitride on top. The wafers are coated with 400 nm of ZEP electron beam resist (Zeon Chemicals), and exposed using an electron beam lithography system (Elionix ELS-F125). After developing the resist in o-xylene, the photonic crystal pattern is transferred into the silicon nitride layer using reactive ion etching (RIE; Surface Technology Systems LPX/MPX) with an SF_6/C_4F_8 plasma. The silicon underneath the beams is then removed using an anisotropic silicon etch (20% KOH in water, 80°C), leaving the beams suspended over a $\sim 20\mu$m deep trench. A final cleaning and surface preparation step is performed in a mixture of H_2SO_4:H_2O_2.

The tapered optical fiber tips are fabricated using a standard heat-and-pull setup consisting of a torch and computer-controlled stepper motor stages. Once the fiber has been tapered down to a diameter of 18 μm, the tip is formed by pulling hard on the fiber with an electromagnet. The taper angle at the apex of the tip is about 8°, but is much more gradual at larger fiber diameters.

A PWC is removed from the substrate using a sharp tungsten tip (Omniprobe) attached to a micrometer stage (PI P-611.3S), and then attached to the fiber tip by touching them together in mid-air. The tungsten tip can then be used to nudge the waveguide around on the fiber tip until it is in the correct orientation. No special treatments are necessary to cause the waveguide to stick to the tungsten tip or to the fiber. This procedure is performed under an optical microscope with a long working distance objective (NA=0.7) to provide the necessary resolution and working space.

The optical interface between the single mode fiber and the PWC can be understood

as an adiabatic taper coupler. This allows the power coupling efficiency η_{wg} to be high (in theory, perfect) and insensitive to the exact overlap lengths and waveguide dimensions. The coupling efficiency can be accurately measured by taking the reflection spectrum of the PWC through the fiber. For a symmetric cavity with no loss channels other than coupling to the waveguide, the power reflection coefficient of the cavity should be $R = 0$ on resonance, and $R \to 1$ off resonance (but still in the stop-band). The amount of power from the fiber that is back-reflected is then simply η_{wg}^2, at frequencies near, but not at, the cavity resonance. This model can be extended to measure cavity asymmetry or the presence of other loss channels, and we find that these effects are not significant for devices with quality factors near those presented here.

The properties of the cavity resonances are estimated from the fabrication parameters using finite-difference time-domain (FDTD) simulations. These allow the resonance frequency, quality factor and spatial shape of the mode to be extracted. The spatial mode profile allows us to compute the mode volume, a measure of the degree of confinement of the optical mode, using the expression:

$$V_m = \frac{\int \epsilon(\mathbf{r}) \left|\mathbf{E}(\mathbf{r})\right|^2 d^3\mathbf{r}}{\left|\mathbf{E}_{max}\right|^2} \tag{A.1}$$

where $\mathbf{E}_{max}$ is the maximum electric field at any point in the optical mode and $\epsilon(\mathbf{r})$ is the dielectric constant at the position $\mathbf{r}$.

A.2.2 Specific properties of device used for Figures 3.3 and 3.4

The device used in the experiments in the main text is formed from a waveguide with dimensions of $w_x = 433$ nm, $w_y = 200$ nm. The lattice constant in the central cavity region is $a_{cav} = 270$ nm, and it increases quadratically to $a_{mir} = 290$ nm in the mirror segment.

The number of holes in the cavity region is 14, and on either side there are additionally 8 mirror holes and 2 smaller holes forming a taper back into the waveguide mode on each side. This gives a total of 34 holes overall. The hole radius is $r = 70$ nm.

The mode studied here at 779.5(1) nm is the second-order longitudinal mode of this cavity; the fundamental mode is located at 758 nm as seen in the complete spectrum in Fig. A.2A. The quality factor of the 779.5 nm mode is about $Q = 460(40)$. The frequencies and quality factors of both modes are consistent with finite-difference time-domain (FDTD) simulations of the fabricated structure. The simulated mode volume of the fundamental mode is $V_m = 0.42\lambda^3$, and the second order mode used in this work has $V_m = 0.89\lambda^3$. The coupling efficiency between the waveguide and the optical fiber was measured to be $\eta_{wg} = 0.06$. This low efficiency is not intrinsic to this coupling scheme; in similar devices we have measured efficiencies above $\eta_{wg} = 0.5$.

The device was (unintentionally) installed into the UHV apparatus at a slight angle with respect to the optical tweezer axis. Specifically, relative to the orientation shown in Fig. A.1, the waveguide is rotated by an angle $\theta_{wg} \approx 36^\circ$ around its own axis and an angle $\theta_{foc} \approx 17^\circ$ out of the focal plane, as determined by a combination of images through the high-NA lens and measurements with the atom. These angles, especially θ_{wg}, modify the distance between the trap and the surface considerably. With $\theta_{wg} = \theta_{foc} = 0$ we would expect a trap distance $z_0 = 191$ nm; with these angles we estimate $z_0 = 259$ nm, which results in a considerably smaller coupling constant. The trapping potential and the trajectory of the atom plotted over the mode of the photonic crystal cavity are shown in Fig. A.2B,C.

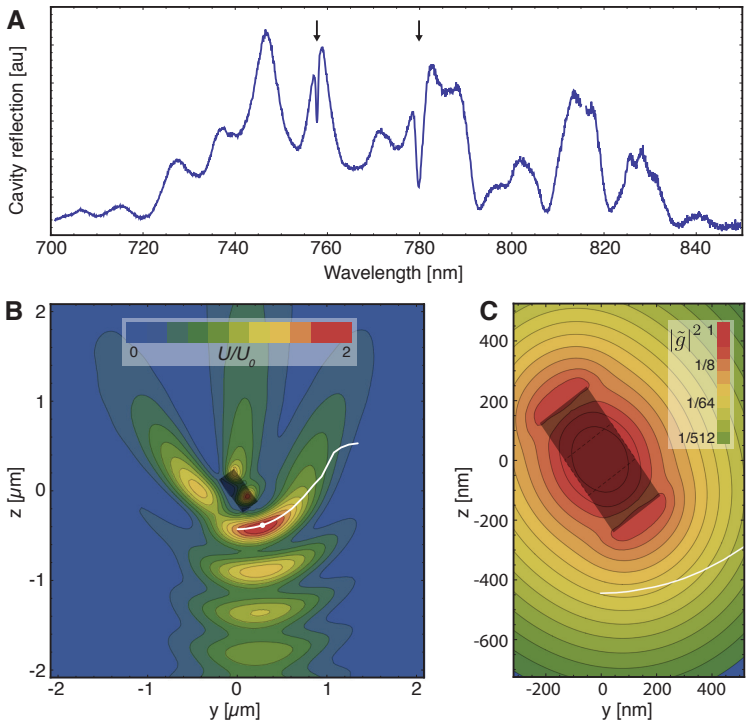

Figure A.2: **Properties of the device used in the experiments** (A) Complete reflection spectrum showing fundamental and second-order cavity resonances at 758 and 779.5 nm, respectively (indicated by arrows). The apparent quality factor of the fundamental resonance is limited by the spectrometer resolution. (B) Color map shows the trap depth $U(\mathbf{r})$ for the optical tweezer position that places the trap closest to the waveguide, normalized to the depth of the tweezer in free space U_0. The shaded area is a cross-section through the PWC, which is rotated by $\theta_{wg} = 36°$ as described in the text (the rotation θ_{foc} out of the plane is also present, but not visible). The white line shows the trajectory of the trap minimum (where $\nabla U(\mathbf{r}) = \mathbf{0}$) as the focus of the tweezer is scanned over the PWC. Surface forces are not included in this plot: $U(\mathbf{r})$ reflects the dipole potential alone. (C) Trajectory of the trap position as it passes close to the waveguide, plotted over a color map indicating the coupling strength to the cavity. Contours show factors of 2 in $|\tilde{g}(\mathbf{r})|^2 \equiv |g(\mathbf{r})/g_{max}|^2$, where $2g_{max}/(2\pi) = 14.0$ GHz is the maximum coupling strength for a cavity with a mode volume of $V_m = 0.89 \times \lambda^3$, for the full Rb dipole moment. The estimated trap position has a coupling of $2g/(2\pi) = 1.0$ GHz, which is reduced to 0.62 GHz by substituting the largest linearly polarized dipole moment, found on the $|2,0\rangle \rightarrow |3,0\rangle$ transition.

A.3 Tuning the trap-to-surface distance z_0

The distance from the closest lattice site to the surface of the nanostructure is determined by the phase shift of the scattered light. This phase depends strongly on the dimensions and dielectric properties of the nanostructure, and can therefore be tuned by tailoring the nanostructure. Surface forces can also pull the trap closer if they are significant compared to the trap depth, but we will first consider the optical potential alone.

To develop some intuition for the behavior of the trap distance, consider first the case of a plane wave incident on the interface between vacuum and a half-infinite space filled with a lossless dielectric. In terms of the fields labeled in Fig. A.3A, the reflection coefficient is $E_r/E_0 = |r|e^{i\phi_r} = (1-n)/(1+n)$, which implies a reflection phase $\phi_r = \pi$ for all $n > 1$. The intensity on the vacuum side is:

$$|E|^2 = |E_0|^2 \left| e^{ikz} + \frac{1-n}{1+n} e^{-ikz} \right|^2 \tag{A.2}$$

which is a standing wave with an intensity maximum at a distance $\lambda/4$ from the interface. For red-detuned trapping light, this results in a trapping potential with a minimum at $z_0 = \lambda/4$.

The addition of a second interface to form a slab (Fig. A.3B) allows ϕ_r to be controlled by changing the slab thickness. In this case, the magnitude of the reflected field also varies with the thickness, such that the trap depth (i.e., the contrast of the standing wave) and distance z_0 are coupled. Solving Maxwell's equations with appropriate boundary conditions for a slab with thickness L yields a reflection coefficient:

$$\frac{E_r}{E_0} = \frac{(1-n^2)\sin(nkL)}{2in\cos nkL + (1+n^2)\sin nkL} \tag{A.3}$$

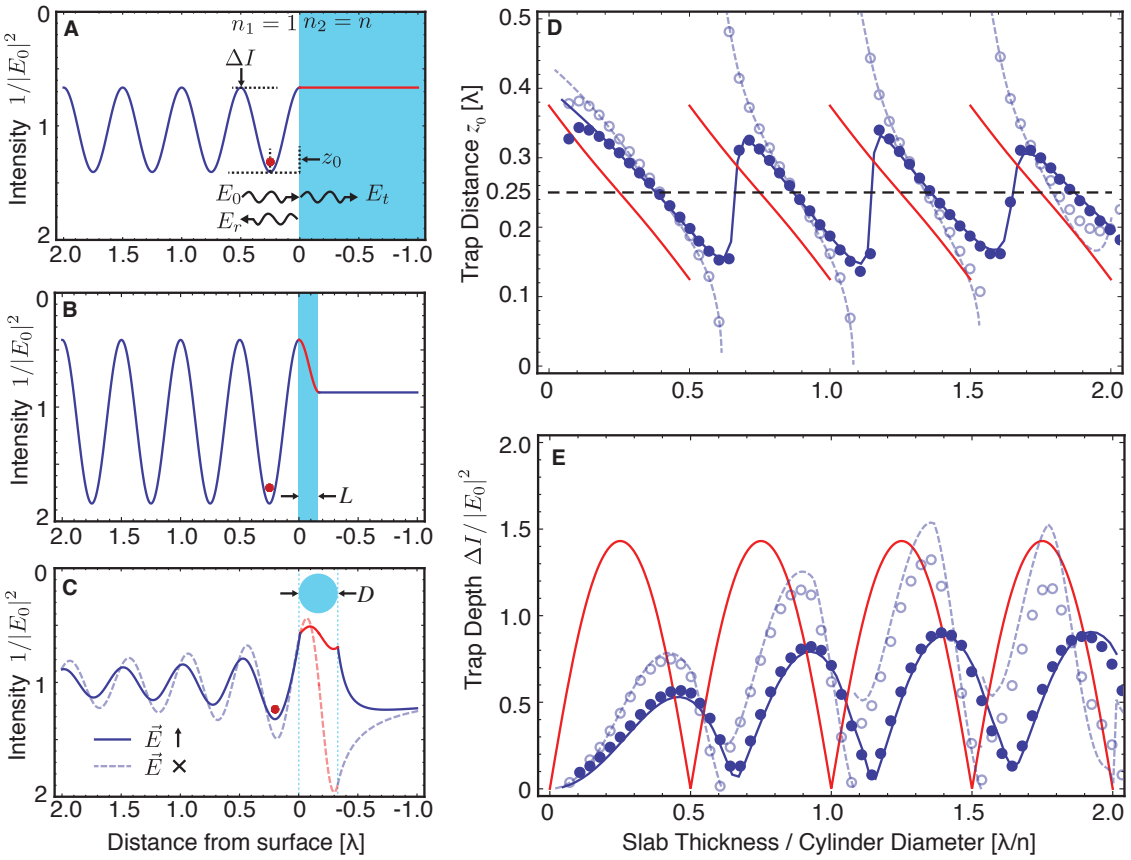

Figure A.3: **Controlling the distance between the trap and the surface** (A) Reflection from a semi-infinite dielectric slab. Note the inverted scale on the vertical axis, implemented so the curves resemble the potential seen by the atom $U \propto -I$, for red-detuned light. Red dots denote the position of the potential minimum. Plane wave components are labeled as referred to in the text. The trap-to-surface distance z_0 and trap depth, ΔI, are also defined. In all panels, refractive indices of $n_1 = 1$ and $n_2 = n = 1.454$ are used. (B) Reflection from a dielectric slab with thickness $L = 0.25\lambda/n$. (C) Reflection of a plane wave from a cylinder with diameter $D = 0.46\lambda/n$. (Solid, dashed) lines show result for electric field polarization (perpendicular, parallel) to the cylinder axis. *(continued on next page)*

Figure A.3: *(continued)* (D) Trap-to-surface distance z_0 vs. structure size for a dielectric slab (red) and a cylinder (blue). For the cylinder, the curve indicates the analytic model with a plane wave, while the points are a 3D FDTD simulation with a gaussian beam with waist 900 nm and wavelength $\lambda = 815$ nm.Solid blue curve and filled circles shows results for electric field polarization perpendicular to the cylinder axis; dashed line and open circles, parallel. Structure size refers to the slab thickness L or the cylinder diameter D; in both cases, the lengths are given in units of the wavelength in the higher dielectric region, λ/n. (E) Trap depth ΔI for the same conditions as panel D. Note that for the cylinder cases the trap depth is taken to be the minimum of the barrier height to the left, into the second lattice site, and the barrier height to the right, into the surface (see panel C).

The reflection amplitude is maximized and $\phi_r = \pi$ when $L = (1, 3, ...)\lambda/4n$; in this case, the trap is again at $z_0 = \lambda/4$. However, varying L allows the trap position to be tuned over the range $\lambda/8 < z_0 < 3\lambda/8$, at the expense of reduced trap depth. For trapping light at $\lambda = 815$ nm, this implies a range from $100 - 300$ nm. All behavior is periodic in L, with period $\lambda/2n$. As seen from Fig A.3D-E, about half of this range can be reached with only a factor of two reduction in trap depth ΔI (not including surface forces).

A more realistic model for the experiments presented here is a plane wave incident on a cylinder. This model is also analytically solvable. The resulting trap depths and distances z_0 exhibit rough quantitative agreement with fully vectorial three-dimensional electromagnetic finite-difference time-domain (FDTD) simulations of a tightly focused Gaussian beam ($1/e^2$ radius $w = 900$ nm) illuminating a cylinder. The fields obtained from the analytic model are plotted in Fig. A.3C for two cases: electric field polarization perpendicular and parallel to the cylinder axis.

In Fig. A.3D-E, z_0 and the trap depth ΔI are shown for a range of cylinder diameters, extracted using both the analytic model and the FDTD simulations. The behavior for the perpendicular polarization is very similar to that of the slab, in that the trap dis-

tance oscillates within the range $\lambda/8 < z_0 < 3\lambda/8$ as the cylinder diameter is increased, with a period in D of about $\lambda/2n$. The oscillations are shifted by $\Delta D \sim \lambda/8n$ from the slab case, because of the behavior of the cylindrical basis functions near the origin.

The case of parallel polarization is rather different: here, z_0 can be tuned over nearly the entire interval $0 < z_0 < \lambda/2$. This allows traps to be formed very close to the surface if sufficient trapping laser intensity can be used to overcome surface forces, as discussed in the following section.

An additional, important difference between the two polarization cases concerns the polarization of the resulting dipole trap. If the incident field is polarized parallel to the cylinder axis, the reflected field will have the same polarization and the total field will be linearly polarized everywhere. However, if the incident field is polarized perpendicular to the cylinder axis, the reflected field will have spatially varying polarization, so the total field will be elliptically polarized. This will produce extremely steep effective magnetic field gradients for the atom (vector light shifts), which can lead to significant dephasing and fluctuating dipole force heating [16]. This is not particular to the cylinder, but is a consequence of the separability of TE and TM modes in two-dimensional systems.

So far, we have not considered the angular spectrum of the scattered field from the cylinder. This is captured by decomposing the total field in a series of partial waves with azimuthal dependence $e^{im\phi}$, where ϕ is an angle in the plane normal to the cylinder axis. The incident plane wave is a sum of all partial waves. For small cylinders with $D \ll \lambda$, only the $m = 0$ wave is reflected, which gives a simple structure to the angular spectrum of the total field. However, for larger cylinders, additional partial waves are reflected and the angular spectrum is more complex. Decomposing the scattered field in this way is not important to understand the trap position when the tweezer is pointed directly at the nanostructure; however, it is quite important for understanding the behavior of the trap

as the tweezer is scanned onto the structure from the side, as part of the loading procedure discussed in the main text. In particular, it is only guaranteed that this process can be performed adiabatically in the case of small cylinders with $D \ll \lambda$, where the reflection is dominated by the first partial wave.

We have made several experimental observations in support of this model. First, the amount of optical tweezer light reflected backwards from a tapered fiber tip is a strong function of the local fiber diameter. This can be seen in images of the reflected tweezer light obtained by rastering the dipole trap across the fiber tip, as shown in Fig. A.4A. Second, we have loaded an atom into the lattice along a tapered fiber at various diameters, as shown in Fig. A.4C. At certain diameters, the atom does not survive the tweezer being scanned onto the fiber, which we interpret as evidence of reduced trap depth at these diameters. Note that this particular data was recorded under conditions where the atom was most likely in the second lattice site away from the surface.

Other shapes, such as the PWC, are not easily modeled analytically. However, we have performed extensive FDTD simulations of these types of geometries, and find that the behavior described above for a cylinder is qualitatively preserved, including the differences between parallel and perpendicular polarizations. An additional question that arises with the PWC is whether it is possible to tune the trap distance z_0 to the desired value while maintaining the photonic crystal bands at the correct frequency. This is a complex optimization problem in a high dimensional space, but it can be solved using numerical methods. We have found that a good approach is to fix the lattice constant a_{cav} (defined below) and the waveguide thickness (w_y), then compute the hole size r that achieves the desired band edge frequency for a series of waveguide widths w_z. This yields a one-dimensional curve in parameter space that can be used to select the trap distance while maintaining a fixed band edge frequency.

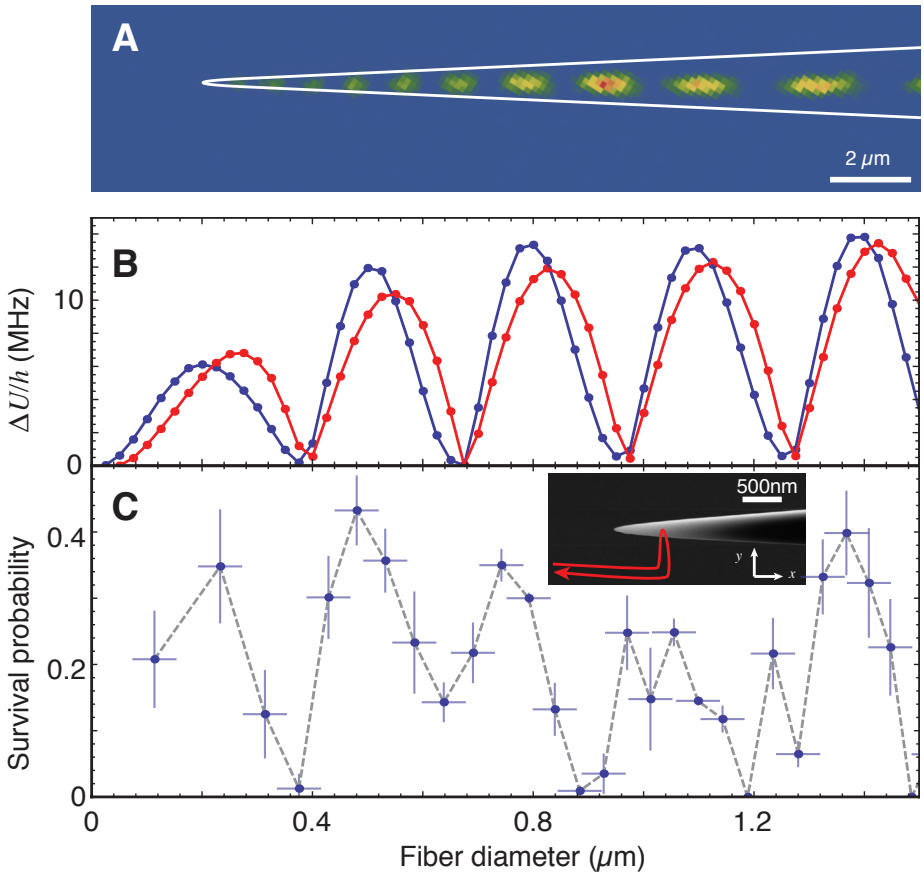

Figure A.4: **Modulation of the trap depth along a tapered optical fiber** (A) Raster scan of reflection of the optical tweezer from a fiber taper similar to the one shown in the inset of panel C. Periodic bright and dark spots show the modulation of the reflection coefficient with the fiber diameter. The white outline is schematic and not to scale. (B) Trap depth vs. fiber radius including surface forces, assuming a tweezer depth of $U_0/\hbar = 2\pi \times 20$ MHz in free space. The (blue, red) curves show the trap depth in the (first, second) lattice sites, computed using FDTD simulations and surface forces from Model II (see text). (C) Experimental data showing the probability that an atom survives an attempt to load into the lattice at various positions along the fiber taper, corresponding to various fiber diameters. The trap trajectory and an SEM image of the fiber taper are shown in the inset. This data was recorded under conditions where the atom was most likely loaded into the second lattice site, when it did survive. The similarity of the curves in panels B and C provides support for the model discussed in the text.

A.4 Loading the lattice from an optical tweezer

In addition to creating the potential near the surface, it is important to be able to load it with atoms. Before we began this work, it had already been demonstrated that it is possible to load single atoms directly into near-surface traps from a magneto-optical trap (MOT) [27]. However, this technique requires that the nanostructure does not significantly perturb the magneto-optical trap, which mostly means that it should have a very small surface area. This condition is clearly satisfied by the optical nanofibers used in [27, 67, 131]. It is less obviously satisfied in our current work, because of the large taper angle of the optical fiber supporting the photonic crystal. It is clearly not satisfied in the case of using on-chip photonic structures, because of the presence of an entire plane of surface. With this direction for future experiments in mind, we decided to pursue an alternative approach.

Instead, we would like to be able to load a single atom into an optical tweezer far away from the surface, and then translate the optical tweezer using a steering mirror until it is pointed directly at the surface. Ideally, this the transformation from the unperturbed tweezer potential to the standing wave discussed in the last section should be adiabatic, such that an atom in the tweezer always makes it into the lattice. By spatially separating the loading zone from the nanostructure, this technique relaxes the restriction on the surface area and is compatible, in principle, with trapping atoms over large planar substrates. Our current experiments do not really exploit this separation, however, since the $\sim 30\,\mu$m distance between the loading zone and the nanostructure is not significant compared to the length scale of a MOT.

Fig. A.5 shows a series of snapshots of the optical tweezer potential as the beam is translated over cylinders of two diameters, $d = 280$ nm and $d = 560$ nm. In the case of

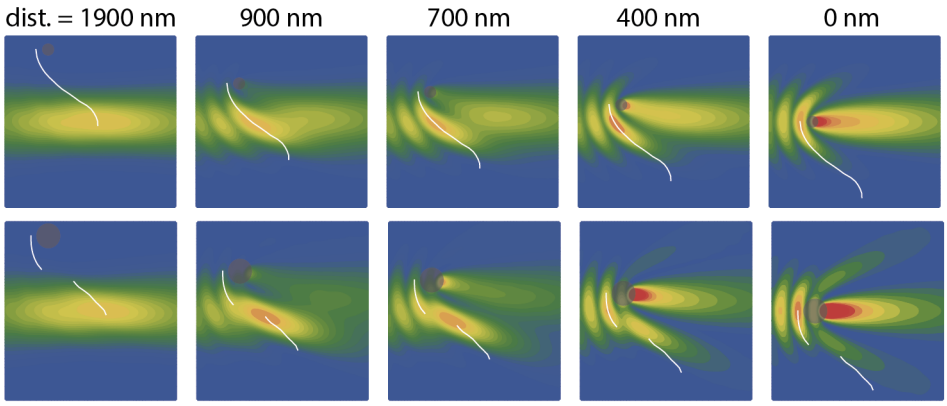

Figure A.5: A series of snapshots of the optical tweezer as it is scanned over a dielectric cylinder with $n = 1.454$ and diameter $D = 280$ nm (top) and $D = 560$ nm (bottom). The optical tweezer has a $1/e^2$ radius of 900 nm, and a wavelength of 815 nm. The position of the cylinder is shown in each picture as a gray cylinder. The white lines show the trajectory of one of the potential minima (intensity maxima) as the beam position is moved. Above each column, the distance between the center of the cylinder and the optical axis of the gaussian beam is indicated. In the top panels with a small cylinder, the maximum of the gaussian beam is smoothly connected to lattice site closest to the surface. In the bottom panels, this is not the case. For offset distances less than 700 nm, two stable potentials exist: one that will become the closet lattice site, and one which is smoothly connected to the gaussian beam. They never overlap, so an atom may not be transferred smoothy between them. The gap in the white line indicates that there is never a potential minimum at this position for any value of the offset distance. In both cases, the optical tweezer is focused about 1μm behind the cylinder, as this gives the smoothest connection to the closet lattice site. By focusing in front of the cylinder, it is possible to connect the gaussian beam to the second lattice site for both fiber diameters (not shown).

the small diameter cylinder, it is apparent that the optical potential deforms smoothly from the unperturbed gaussian beam into the lattice, with the potential minimum following a continuous path leading to the closest lattice site. This does not occur with the larger cylinder: in this case, the closest lattice site does not connect to the unperturbed tweezer. Instead, it appears suddenly, while the tweezer only connects to the second lattice site. As discussed in the next chapter, the atom-photon coupling decays exponen-

tially with distance, and for reasonable parameters the coupling in the second site is 500 times smaller than in the first site. Therefore, it is safe to say that the second site is uninteresting, and that the behavior of the trap behavior show in Fig. A.5b is not useful.

A deep analytic understanding of this behavior has eluded us, but some insight can be had from looking at the angular spectrum of a plane wave scattered from a cylinder. This is captured by decomposing the total field in a series of partial waves with azimuthal dependence $e^{im\phi}$. The incident plane wave is a sum of all partial waves. For small cylinders with $D \ll \lambda$, only the $m = 0$ wave is reflected, which gives a simple structure to the angular spectrum of the total field. However, for larger cylinders, additional partial waves are reflected and the angular spectrum is more complex. The first point in Fig. A.3D/E where the trap depth ΔI vanishes (at $d \approx 0.6\lambda/n$) is precisely the point where the reflection from the $m = 0$ and $m = 1$ partial waves destructively interfere, which is to say, where they become equal in magnitude. This is the boundary of the region where the reflected $m = 0$ wave dominates. We find from numerical simulations that this is also the boundary of the region where the first lattice site is connected to the unperturbed optical tweezer.

This leads us to the conclusion that higher-order partial waves interfere with the loading process. This is intuitively reasonable: if the only reflection is $m = 0$, then the pattern of the scattered light has no angular dependence. On the other hand, once $m = 1$ reflection is added, there is a strong angular dependence of the reflected field (both in amplitude and phase), which causes the position and depth of the trap to vary as a function of angle. Since the position of the trap must rotate nearly 90° around the fiber during the loading process, this angular dependence can cause the trap to get "stuck" or to disappear and reappear, as visible in Fig. A.5b.

A.5 Surface forces and minimum achievable z_0

The van der Waals/Casimir-Polder force between the atom and the substrate is significant compared to typical trapping forces at the length scales under consideration here. As discussed above, the minimum of the optical potential can be moved continuously until z_0 is nearly zero. Therefore, the ultimate atom-surface distance that can be achieved with this technique will be determined solely by the acceptable optical potential depth, and how tightly it can hold the atom against surface forces. Factors to consider in determining the achievable potential depth are heating or decoherence from photon scattering, light shifts or damage to the nanostructure resulting from high optical powers.

We have used two models to estimate the interaction between the atom and the surface. The first, simpler estimate is made by approximating the surface as a semi-infinite space of dielectric (Model I). The atom-surface distance d is taken as the distance between the atom and the closest point on the real structure. To calculate the force in the intermediate regime where $d \sim \lambda/2\pi$, we use the QED calculation outlined in [132]. In the regime where thermal effects are not present, $z \ll \hbar c/k_B T \approx 7\mu$m (at 300 K), we find that the resulting potential can be fit to an effective form $U(z) = -C_3\lambda_{\text{eff}}/(2\pi)/\left[z^3(z+\lambda_{\text{eff}}/(2\pi))\right]$. This fit tracks the QED calculation results to better than 5% for $d < 500$ nm. For Rb and (glass, silicon nitride) we find $C_3/\hbar = 2\pi \times (860, 1500)\,\text{Hz}\,\mu\text{m}^3$ and $\lambda_{\text{eff}} = (710, 650)$ nm. For this calculation, atomic polarizabiltiy data (at imaginary frequencies) was taken from [133], and dielectric data (at real frequencies) from [134] (glass) and [134, 135] (silicon nitride). The glass dielectric data was extrapolated to imaginary frequencies by fitting to a four oscillator model, while the silicon nitride data was fit to a five oscillator model. In the latter case, the fit is rather poor. However, the values for silicon nitride are not used in the present analysis, and are presented for comparison only.

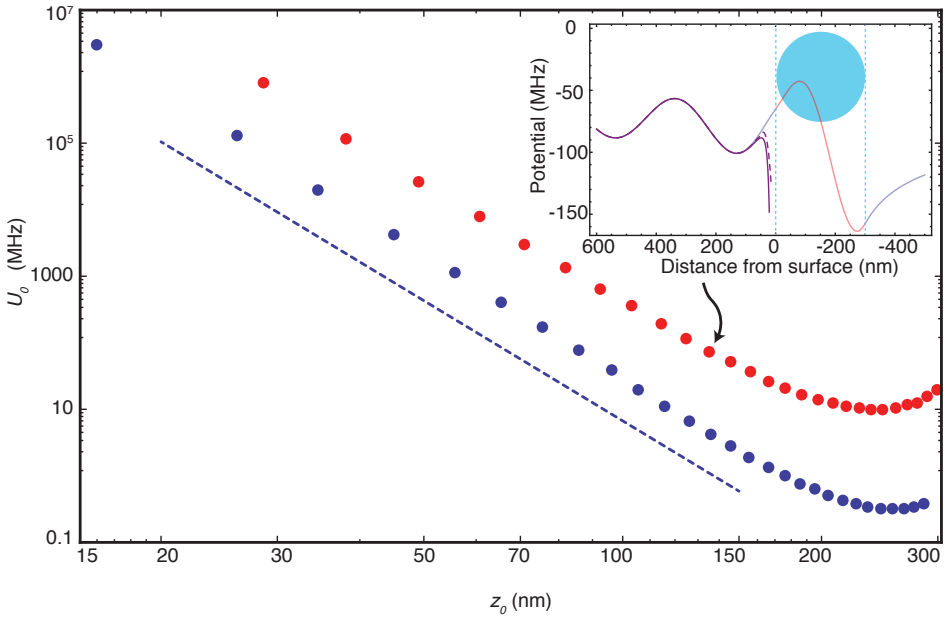

Figure A.6: **Trap depth required to approach the surface** (Blue, red) curves show the optical tweezer trap depth U_0 required to have at least (one, twenty) bound states at a given distance z_0 from the surface of a glass ($n = 1.454$) optical fiber. Each point represents a different fiber diameter, in the range $84\,\text{nm} < D < 344\,\text{nm}$. The calculations were performed using the analytic model for the optical potential presented in Fig. A.3 and surface forces from Model I (see text). The electric field is polarized parallel to the cylinder axis. The dashed line shows the approximate scaling $U_0 \propto z_0^{-6}$, which holds for $z_0 < 200$ nm. At larger z_0, the standing wave contrast decreases more rapidly than the surface forces. (Inset) Line cut through the potential for a cylinder with diameter $D = 300$ nm, where $z_0 = 130$ nm, showing the total potential for $U_0/\hbar = 2\pi \times 80$ MHz . The two purple lines show the potential including surface forces (solid: Model I, dashed: Model II). As expected, the surface forces are slightly less for the model incorporating the finite size of the fiber. The light colored lines show the electric field intensity, following Fig. A.3

In the second method, we remove the approximation of the fiber as a dielectric half-space by calculating the dyadic Green's tensor at imaginary frequencies for the actual fiber geometry [136] (Model II). This is performed using the freely available SCUFF-EM software [**?**] which implements a boundary element method. The environment is taken to have zero temperature, which is accurate in the distance range considered here. The second method gives a slightly reduced surface potential, as expected, because the amount of polarizable material contributing to the surface forces is less.

In Fig. A.6, we show that the power required to maintain a trap with a given number of bound states scales as approximately $U_0 \sim z_0^{-6}$. A harmonic trap translated into the surface without distortions (other than surface forces) would require $U_0 \sim z_0^{-5}$; the additional factor of $1/z_0$ here arises from distortions to the standing wave in the near-field region around the nanostructure.

To give a realistic estimate of the distance that can be achieved in an apparatus like ours, we note that both the fibers and PWCs used in our experiments have shown no effects from exposure to 5 mW of laser power from the optical tweezer. We have not probed higher powers. At our trap wavelength, this corresponds to a depth (in the absence of the nanostructure) of $U_0/\hbar = 2\pi \times 80$ MHz (3.8 mK). At this depth, one bound state is maintained until $z_0 \approx 80$ nm. For the type of experiments presented here, it is useful to have many bound states (so the atom can heat from photon recoil and still remain trapped); at $z_0 = 130$ nm, this trap depth gives around 20 bound states.

Experiments with atomic condensates have observed attractive surface forces from atoms adsorbed onto the surface that are significantly larger than what is expected for the van der Waals/Casimir-Polder force alone [137]. The scaling of these forces with distance depends on the geometry of the substrate. These forces will increase the minimum achievable atom-surface distance; however, they can be mitigated by minimizing the num-

ber of atoms deposited on the substrate (which is fully compatible with a single-atom trap) or by periodically removing adsorbed atoms. In our experiments with the nanofiber alone, we found that trapping in the first lattice site was only possible if we periodically (every 5 minutes) illuminated the fiber tip with around 20 μW of blue light at 473 nm (for several seconds), following the ideas in [138]. However, in the case of the PWC, we found the opposite result: applying blue light made it impossible to trap in the closest lattice site, with the effect persisting for approximately one hour after the application of the light. Therefore, the blue light was not used in the experiments with the PWC. We have performed no further experiments to understand this effect, but have not had any difficulties with loading consistently into the first lattice site without blue light.

A.6 Peak assignments in figure 3.2C

We now discuss the measurement behind Fig. 3.2c in more detail. An atom is prepared in $|1,0\rangle$ in the free-space optical tweezer, and loaded into the lattice. Then, a laser field tuned in between the $F = 1$ and $F = 2$ D2-line transitions (Fig. 3.2C, inset) is applied through the fiber, which produces opposite light shifts for the $|2,0\rangle$ and $|1,0\rangle$ states. At the same time, a microwave pulse drives the $|1,0\rangle \leftrightarrow |2,0\rangle$ transition. After moving the atom away from the fiber, the $F = 1$ population is measured as discussed above. This sequence is repeated for many microwave frequencies, to map out the spectra shown in Fig. 3.2C.

This technique clearly shows the discrete nature of the optical lattice. However, because of the nearly-exponential functional form of the evanescent field producing the AC Stark shift, only the relative distance between lattice sites can be determined with this technique, in principle.

To determine whether the site with the largest AC Stark shift is in fact the first lattice site, we have also measured the absolute emission rate of the atom into the fiber. This is done by loading the atom into the supposed first lattice site, and driving fluorescence with a probe beam co-propagating with the tweezer, resonant with the $F = 2 \rightarrow F = 3$ transition. The laser intensity is high to ensure the fluorescence rate is saturated. The photons scattered into the fiber are counted on an APD, yielding a rate Γ_c which is compared to the saturation scattering rate of $0.5\Gamma_0 = 0.5 \times 2\pi \times 6$ MHz to determine the coupling efficiency. By counting only photons arriving in the first 250 ns after the driving laser is applied, we ensure that the atom has not been pushed closer to the fiber by radiation pressure or a gradient force from the driving beam. In this way, we obtain a cooperativity $\eta = 2\Gamma_c/\Gamma_0 = 0.015(6)$, where we have corrected only for the APD quantum efficiency (60%) and independently measurable losses in the optical path outside of the vacuum chamber. Using the numerically computed decay rate into the fiber at various distances, we conclude that the atom is at a distance $z_0 < 375\,\text{nm}$ from the fiber surface, which excludes the second lattice site. This is a maximally conservative estimate of the distance as we have not included any optical losses that we could not directly measure, such as losses in the fiber taper. In similarly fabricated devices, we have measured losses in the tapered region ranging from 25% to 80%, arising from a bend in the fiber taper that is necessary to satisfy geometric constraints in our apparatus. These losses have been reduced significantly in experiments with the PWC by changing the position of the bend.

The distance determination above implicitly assumes that the saturation scattering rate is the same near the fiber as in free space. Modifications to the total decay rate from emission into the fiber and increased emission into the far field can be incorporated self-consistently by adjusting the assumed total scattering rate as a function of z_0. This correction is less than 10% at a distance of $z_0 = 200$ nm, and decays rapidly at larger

distances from the fiber.

A.7 Analysis of transmission spectrum in Figure 3.4

The transmission data presented in Fig. 3.4 of the main text is shown with a full master equation model which includes 5 ground-state magnetic sublevels in the $F = 2$ manifold and 7 excited-state sublevels in $F' = 3$. The Hamiltonian includes the laser detuning $\Delta_a = \omega_L - \omega_a$ (with laser frequency ω_L, atomic resonance ω_a), the polarization of the cavity mode, the position of the atom in the $\hat{x}$ direction, a magnetic bias field of 2.5 G along $\hat{z}$, and scalar, vector and tensor light shifts from the dipole trap. The master equation also incorporates the cavity decay and the spontaneous emission of the atom into free-space modes, which is assumed to be unaffected by the proximity to the waveguide.

We calculate the steady-state solution to the master equation at each laser detuning, and extract the transmission $T(\Delta_a)$ from the mean intracavity photon number, which is proportional to the transmitted intensity. This accurately represents the experimental situation for all of the points in Fig. 3.4 that contribute to the fit, as the timescale to reach the steady state is short compared to the lifetime of the atom in the trap. Based on the drift observed in Fig. 3.3 we conclude that over the much longer time needed to acquire the data in Fig. 3.4 (49 hours) the position of the atom varies by about one lattice constant, so the resulting $T(\Delta_a)$ is averaged over a set of simulations using the cavity polarization and intensities at different points along the waveguide axis, spanning one period of the intra-cavity standing wave (290 nm). Each simulation is weighted equally in the average.

The resulting curve is then averaged over an ensemble of atomic energies to account for the finite temperature of the atom. A Boltzmann energy distribution and a harmonic

trapping potential are assumed so $p(E) = \frac{E^2}{2(k_B T_{at})^3} \exp\left[-E/(k_B T_{at})\right]$, where $p(E)$ is the probability density to have total energy E, T_{at} is the atomic temperature and k_B is Boltzmann's constant. In a harmonic trap, the average potential energy $U = E/2$, and the transmission curve is shifted by the ground state light shift such that $T(\Delta_a; E) \rightarrow T(\Delta_a + E/2)$. This is an approximation that neglects changes with E in the excited state light shift as well as in the vector light shift in the ground state.

Additional uncertainties in the waveguide rotation angles θ_{wg} and θ_{foc} and in the intensity and polarization of the trapping light relative to the waveguide axis make it impractical to produce a model with no adjustable parameters. However, for a broad range of parameters that coincides with the experimental bounds, we find reasonable agreement between the model and the data in terms of the asymmetry and shift of the transmission dip. The extracted cooperativity η is also insensitive to the precise values of the model parameters. The curve shown in the main text corresponds to a trap with a scalar light shift for the ground state of 32 MHz and a polarization ellipticity $\mathbf{Im}\left[\epsilon \times \epsilon^*\right] = 0.3$ [16], which gives rise to an effective magnetic field of 1.5 G that adds to the applied field for a total field of 4 G along the $\hat{z}$ axis. The temperature assumed is $T_{at} = 125\,\mu$K, which is plausible given that the atom in the free-space tweezer has a thermal energy around $k_B \times 7\,\mu$K along the $\hat{z}$ axis, and that the trap frequency along this axis is more than a factor of 30 higher in the lattice. This curve also reflects the simplest case $\theta_{wg} = \theta_{foc} = 0$, to reduce the number of free parameters. A small frequency offset of 6 MHz has been added to the model; without this shift, the model predicts a maximum decrease in transmission at more positive detuning. From this, we conclude that the experimentally measured transmission dip of 2.2% would be extended to 13(2)% for an atom fixed at the optimal $\hat{x}$ coordinate, constrained to the $|2,0\rangle \rightarrow |3,0\rangle$ subspace, and exactly on resonance with the cavity.

Two effects contribute to the broadening of the line: thermal broadening, and optical pumping into hyperfine sublevels with different energies. The first effect produces a spectrum that has a long tail at negative detunings (reflecting the long tail towards high energies found in the Boltzmann distribution). The second effect produces a spectrum with the appearance of a long tail at positive detunings. This arises from the combination of a magnetic field and the tensor light shift. The resulting energy eigenstates in the $F' = 3$ level have an uneven spacing, with more transitions at lower frequencies and fewer at higher frequencies, as shown in Fig. A.7. Since the cavity polarization is not circular, the atom is optically pumped into a distribution of m_F sublevels in the ground state, so the total transmission profile is effectively an average over all of the possible transitions in Fig. A.7. The width of the model curve is dominated by optical pumping, but thermal effects need to be included to get reasonable agreement with the data, and their combination makes the curve nearly symmetric.

This optical pumping effect is obviously undesirable, and is a significant drawback of having a linearly polarized cavity mode. However, it can be improved in future experiments by improving the control of the atomic position so the atom experiences only a single linear polarization, and isolating the $|2,2\rangle \rightarrow |3,3\rangle$ transition spectrally using magnetic fields. This will result in a cooperativity that is 5/6 lower than on the $|2,0\rangle \rightarrow |3,0\rangle$ transition, which has the largest $\hat{\pi}$ polarized dipole moment.

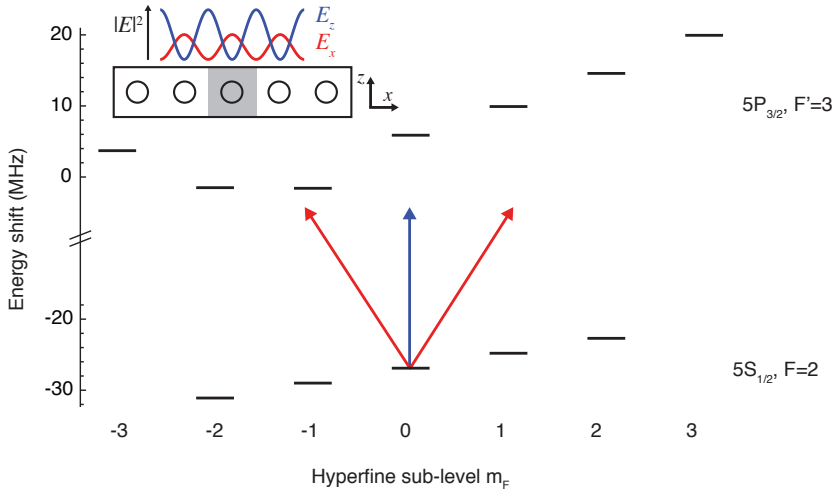

Figure A.7: **Energy levels in the presence of the dipole trap and a magnetic field** The energies of the magnetic sublevels within the ground state ($F = 2$) and excited state ($F' = 3$) manifolds are shown here for the parameters discussed in the text. Note that the excited state m_F levels are mixed significantly by the tensor light shift, such that m_F is no longer a good quantum number. For example, the state labeled $m_F = 0$ has only 60% overlap with the real $m_F = 0$ eigenstate. The inset shows the polarization of the cavity field over several periods of the photonic crystal waveguide: it consists of out-of-phase $z-$ and $x-$polarized standing waves. The optical transitions driven by these fields are indicated by the arrows of the same color in the main figure. In the model for the data in Fig. 3.4, the simulated transmission curve is averaged over a uniform distribution of positions within a single lattice site, as indicated by the gray shaded region in the inset.

Appendix B

Apparatus and methods used for the experiments presented in Chapter 4

B.1 Experimental setup

B.1.1 Apparatus

Our setup is described in detail in Ref. [16, 17], and is only briefly reviewed here. The apparatus consists of an ultra-high vacuum (UHV) system with a ^{87}Rb MOT. We trap single atoms in a tightly focused scanning optical tweezer (waist $w_0 = 0.9\,\mu$m, wavelength $\lambda = 815\,$nm, trap depth $U_0 = 1.0\,$mK), which is formed at the focus of a aspheric lens (Thorlabs 352240). After loading an atom from the MOT and performing Raman sideband cooling [16] to better localize the atom, we increase the tweezer depth to $U_0 = 2.1\,$mK and translate the tweezer to the photonic crystal cavity, about $40\,\mu$m away. At its final position the optical dipole trap is formed by the interference of the optical tweezer with its reflection from the PC, creating a 1D optical lattice. Based on numerical simulations we estimate the closest lattice site to be 180 nm away from the surface, with a maximum light shift of $\sim 4\,$mK. The trap depth is smaller than this maximum value because of a finite light intensity at the surface of the PC and additional surface forces.

From measurements of the atom-cavity coupling, we infer that the loading procedure succeeds more than 90% of the time. The lifetime of the atom in the tweezer is about 0.25s near the photonic crystal, which is shorter than the lifetime in the tweezer in free space (6 s). To ensure relative position stability of the tweezer and the PC we periodically measure the position of the PC and adjust our coordinate system for observed drifts. The PC position is determined by inserting 815 nm light into the PC and detecting the emitted light through the optical tweezer path. By taking 5 images in different focal planes the PC position is determined in 3D.

The finite temperature of the atom leads to time-varying light shifts of the optical transition in the presence of the dipole trap [17]. In order to suppress this effect in the measurements presented in Figures 2 and 4, we modulate the dipole trap intensity with full contrast at 5 MHz and probe the atom-photon interaction only when the intensity is nearly zero. Since this modulation is much faster than the highest trap frequency (710 kHz), the atom experiences a time-averaged potential and the trapping potential is well-described by the potential averaged over one modulation period, as explored in time-orbiting potentials for ultra cold atoms and RF Paul traps for ions. For modulation frequencies above 4 MHz we observe no reduction of the trap lifetime compared to the unmodulated trap. The modulation is produced by dividing the dipole trap beam into two paths, shifting with two coherently driven acousto-optic modulators (AOM) detuned by the desired modulation frequency, and recombining the two AOM outputs into a single-mode fiber. When applying this modulation we observe the optical transition frequency to be within 5 MHz of its free space value. In an unmodulated trap of the same average intensity it is shifted by ~ 120 MHz.

For the measurements in Figures 2 and 4, both the probe and gate pulses consist of a train of Gaussian pulses with a FWHM of 24 ns. These pulses are generated by a

fiber-based electro-optic modulator (Jenoptik AM 830) driven by an arbitrary waveform generator (Agilent 33250A). Synchronization with the dipole trap modulation is achieved by triggering the pulse train with a low-jitter delay generator (SRS DG645) from a photodiode which monitors the dipole trap power directly.

All measurements were performed with single photon counting modules (Perkin Elmer SPCM-AQRH), recorded using a PicoHarp 300 time-correlated single-photon counting system.

B.1.2 Polarization interferometer

In section B.4 we give a detailed description of the input and output modes of the interferometer. Here, we discuss the experimental implementation.

Experimental implementation

The PC is mounted inside the UHV system attached to a tapered optical fiber. The fiber is guided out of the UHV system through a fiber feedthrough and integrated into a fiber based interferometer (see Figure B.1). All fiber-fiber connections are fusion spliced to ensure high coupling efficiencies and we achieve a total efficiency from the free space fiber coupler to the tapered fiber of 78%, mostly limited by PBS2. The fiber of the $|V\rangle$ polarized reference arm is glued to the side of a piezo stack, which allows for tuning ϕ_{V} over many tens of π. We adjust the polarization of the various arms by means of fiber polarization controllers. We find that optimizing the polarization controllers once every few weeks is sufficient for stable operation of the interferometer.

The path length of the two arms of the interferometer are adjusted to be within several mm of each other, so that the free spectral range of the interferometer is large

($> 30\,\mathrm{GHz}$) compared to the range of frequencies used to probe the atom.

Thermal effects cause fluctuations of the relative phase of the two interferometer arms. We compensate for these drifts by stabilizing ϕ_V such that the power in the A port is minimized in the absence of an atom. In order to obtain an error signal for the stabilization we send a 780 nm probe beam through the interferometer while dithering ϕ_V. We use a field programmable gate array (FPGA) to implement lock-in detection of the modulated probe reflection and apply feedback to ϕ_V. This feedback is applied during the Raman cooling sequence (which lasts $\sim 150\,\mathrm{ms}$).

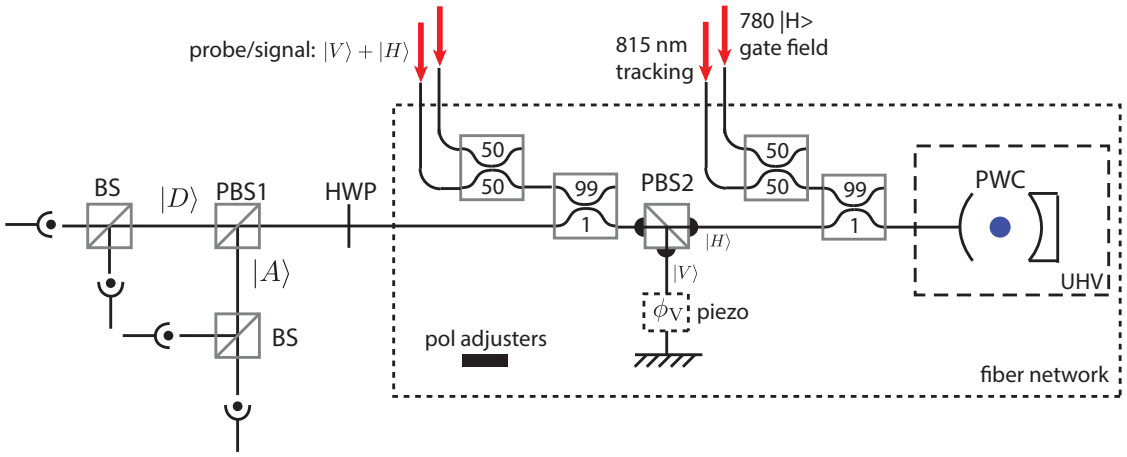

Figure B.1: Schematic drawing of the fiber based polarization interferometer. All components within the dashed line are fiber-based. PBS1 and PBS2 are free-space and a fiber-based polarization beamsplitters, respectively. BS denotes 50/50 beamsplitters and HWP and FC are a $\lambda/2$-plate and a fiber coupler. In both the D and A ports of the interferometer a pair of detectors is used for photon-photon correlation measurements. The fiber beamsplitters are labeled with their coupling ratios. The two 780 nm input fields are used for coupling to the atom and for stabilizing the cavity and interferometer, while the 815 nm field is used for stabilization of the device position.

B.1.3 Photonic crystal design and fabrication

The PC cavities are fabricated using electron beam lithography and reactive ion etching, as described previously in [1]. The cavities used in this work are formed from waveguides with a cross section of 500 nm by 175 nm, and are patterned with rectangular holes of size 225 nm by 126 nm. The pitch of the holes is 280 nm in the center of the cavity, and gradually increases to 315 nm on either end of the cavity. To make the cavity single-sided, there are 5 extra holes on the side of the cavity opposite the fiber, which increases the reflectivity of this mirror by a factor greater than 10.

To enable the cavities to be heated with a laser for thermal tuning of the transition frequency, a pad is formed on the waveguide (as visible in Figure 1c) and coated with amorphous silicon. Depositing this material is the final step in the fabrication process, to allow the absorbing material to be chosen independently of its compatibility with the strong acids and bases used for undercutting and cleaning the waveguides. This is accomplished by using a patterned silicon nitride membrane as a stencil for electron beam evaporation of the absorbing material. The membrane is held several microns over the top of the cavities with a spacer, and aligned to deposit the absorbing material on the pads without contaminating the cavities.

After fabrication, an array of cavities is characterized with a tapered fiber probe. Using the linewidth and the amount of power reflected at the cavity resonance frequency, we can extract both the decay rate into the waveguide and the decay rate into other modes that we do not collect. In the set of cavities fabricated for this experiment, the decay rates into other modes ranged from $\kappa_{sc} = 4 - 15\,\mathrm{GHz}$, corresponding to loss-limited quality factors of about 30,000 - 100,000. The waveguide decay rate was fixed by the fabrication parameters to be $\kappa_{wg} = 20\,\mathrm{GHz}$, ensuring that all cavities are over-coupled.

B.1.4 Interferometer and PC characterization

We characterize the cavity and interferometer using a New Focus Velocity TLB-6712 tunable laser. In the absence of an atom we measure the reflection of a diagonally polarized probe field as a function of laser frequency ν. The output state of the interferometer is $|\psi_{out}\rangle = (1/\sqrt{2})(|r_V|e^{i\phi_0(\nu)}|V\rangle + r_c(0)|H\rangle)$ where $\phi_0(\nu) = \nu/\nu_{FSR}$ is the relative phase accumulated between the two arms, ν_{FSR} is the interferometer free spectral range, $r_c(0) = |r_c(\nu)|e^{i\phi_c(\nu)}$ and $|r_c(\nu)|$ and $\phi_c(\nu)$ the reflection coefficient and phase of the empty cavity. We measure the power in the D and A ports as a function of probe detuning and analyze the sum and difference of the two detectors:

$$\mathcal{D} + \mathcal{A} \sim \frac{1}{2}\left(|r_V|^2 + |r_c(0)|^2\right) \tag{B.1}$$

$$\mathcal{D} - \mathcal{A} \sim \mathrm{Re}\left(|r_V| r_c(0) e^{-i\phi_0(\lambda)}\right) \tag{B.2}$$

Figure B.2 shows a measurement of both the sum and difference of the interferometer ports. The sum shows a dip in reflected power at the cavity resonance, which arises from the finite losses of the cavity. In the differential signal the resonance is resolved in the 2π phase flip of the interferometer across the cavity resonance. The solid lines are Eq. B.1 and B.2 fitted to the data leaving ν_{FSR}, κ_{wg}, κ_{sc} and a global phase and amplitude as free parameters. We obtain a free spectral range of the interferometer of $\nu_{FSR} = 33\,\mathrm{GHz}$, $\kappa_{wg} = 20.3\,\mathrm{GHz}$ and $\kappa_{sc} = 5.2\,\mathrm{GHz}$, yielding $k = \kappa_{wg}/\kappa = 0.8$, where $\kappa = \kappa_{sc} + \kappa_{wg}$.

B.1.5 Cavity tuning

At room temperature the cavity resonance is at 779.8 nm, selected to be slightly to the blue of the atomic ^{87}Rb resonance at 780.03 nm. We thermally tune the cavity resonance

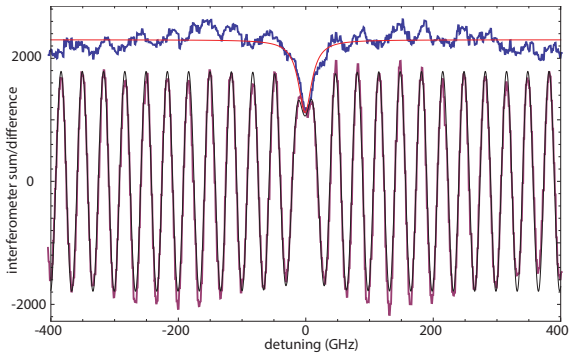

Figure B.2: Characterization of the interferometer and PC. The solid blue and black curves are the measured sum and difference of the two interferometer ports respectively. The red solid and dashed lines are the fit to Eq. B.1 and Eq. B.2 respectively. The cavity resonance is visible as the dip in the sum which arises from cavity losses and in the difference signal as a 2π phase flip over the resonance.

by applying a 802 nm laser beam focused to a 2.1 μm beam waist on the absorptive silicon patch shown in Figure 1b. Heating the cavity allows for thermal tuning of the cavity resonance to the red with a measured tuning coefficient of $\sim$ 0.4 nm/mW, we have observed reversible tuning up to +2 nm from the room-temperature resonance.

To lock the cavity on the atomic resonance we use a similar scheme as we use to lock the interferometer. We measure the reflection of the same 780 nm probe beam and lock the cavity resonance by applying feedback to the heater laser intensity. We dither the heater-intensity and perform a lock in measurement and feedback using the FPGA. The feedback is applied during the Raman cooling sequence, simultaneous with locking the interferometer. The cavity is typically locked $\sim 1-2$ linewidths to the blue of the ^{87}Rb resonance to account for a small additional heating of the cavity by the optical tweezer. Pointing alignment of the heater laser on the PC is periodically optimized by scanning the heater laser position using a scanning piezo mirror minimizing the heater laser intensity required for locking the cavity.

B.1.6 Measurement sequence for switching experiment

Figure B.3 shows a detailed version of the sequence used for the switch experiment. The first 500 μs consist of preparing the atom in the $|u\rangle$ state by means of microwave transfer and optical pumping (see section B.2.1). Following, the atom is put in the superposition $|u\rangle + |c\rangle$ by means of a 7.5 μs long $\pi/2$ microwave pulse. Then 10 Gaussian (FWHM of 25 ns) $|H\rangle$ polarized gate pulses are applied at instances that the dipole trap is at its minimal intensity. A second $\pi/2$ microwave pulse with variable phase θ rotates the atomic superposition to its final state. The atomic state is detected with 500 Gaussian probe pulses at times that the dipole trap intensity is minimal, followed by a 15 μs long π pulse and a second identical readout sequence. For the data with the gate pulse a fast conditional logic circuit (Lattice ispMACH LC4256ZE) prohibits the execution of the readout sequence if no photon was detected during the a several μs-wide window around the gate pulses. This prevents unnecessary heating of the atom by the readout at instances that no gate photon was detected. The complete sequence is typically repeated 100 times for one atom.

For the measurements of the photon phase presented in Figure 2 we use a similar method of pulsed probing using the dipole trap modulation without applying the microwave modulation and the gate pulse. For the data in Figure 3, no dipole trap modulation was applied.

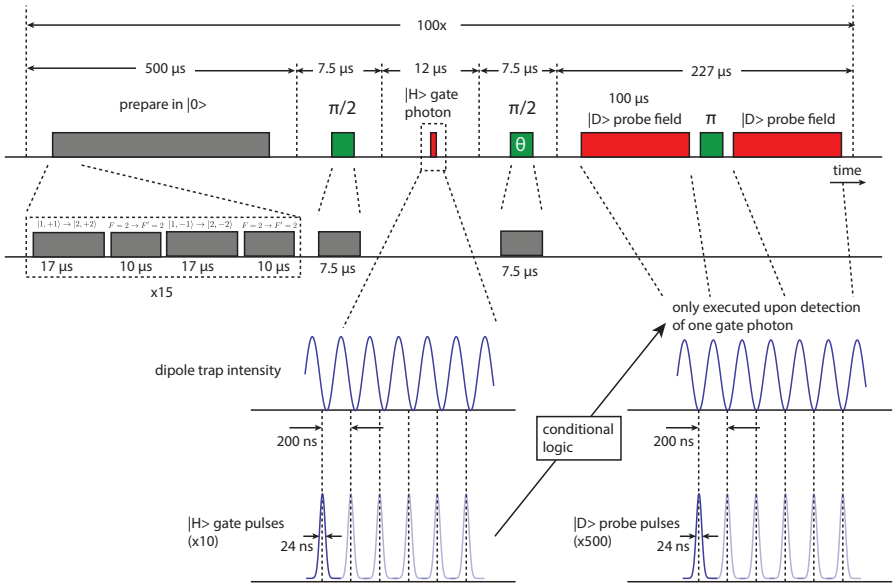

Figure B.3: A schematic representation of the switch sequence. See text for details.

B.2 Experimental methods

B.2.1 Internal state preparation

For the switching experiments we perform state preparation into the $|F = 1, m_F = 0\rangle$ magnetic sub-level. Conventional methods for state preparation in magnetic sub-levels involve optical pumping with well defined polarization such that one internal state is dark to the optical pumping process. However, in the vicinity of the PC obtaining a clean polarization is challenging because of unavoidable scattered light. To achieve efficient optical pumping while being trapped near the PC we employ a combination of optical pumping and coherent microwave transfer. We apply light resonant with the $F = 2 \rightarrow F' = 2$ transition of the D2-line to deplete the $F = 2$ manifold. Simultaneously, we perform a coherent microwave transfer between the $|F = 1, m_F = \pm 1\rangle$ and $|F = 2, m_F = \pm 2\rangle$

sub-levels. As a result the atomic population accumulates in the dark $|F = 1, m_F = 0\rangle$ sub-level. We toggle the microwave pulses (each $17\,\mu$s) and the optical pulses ($10\,\mu$s) sequentially but have observed similar behavior with the optical beam continuously on and $25\,\mu$s microwave pulses. The optical intensity is matched to have similar optical pumping rates and microwave transfer rates. We use the stretched $|F = 1, m_F = \pm 1\rangle \rightarrow |F = 2, m_F = \pm 2\rangle$ transitions instead of $|F = 1, m_F = \pm 1\rangle \rightarrow |F = 2, m_F = \pm 1\rangle$ because of the larger Clebsch Gordan coefficients and slightly σ-polarized nature of our microwave field, leading to a faster pumping rate. Under conditions with $25\,\mu$s microwave pulses and continuous optical pumping we find that after 5 cycles the atom is with $\sim 90\%$ probability in the $|F = 1, m_F = 0\rangle$ state, and the pumping rate is well fit by an exponential time-constant of $\tau_{1/e} = 57\,\mu$s.

B.2.2 Single shot readout and verification of the atom presence

We typically repeat each measurement 100 times per single trapped atom. After this period the atom is lost from the trap with high probability. Hence we analyze our data to select only events where an atom was present or not with high certainty. A typical readout measurement of the atom consists of 500 pulses (see Figure B.3) over which we typically detect $\bar{n}_A^1 \simeq 6.2$ and $\bar{n}_A^0 \simeq 0.2$ for the cases with and without an atom present in the $F = 2$ manifold (see Figure 4b). We observe no distinction between an atom present in the uncoupled $F = 1$ manifold and no atom present, confirming that the $F = 1$ state is not coupled to the cavity field. We assign events with $n > 1$ to have an atom present in the $F = 2$ manifold. For this threshold the measured fidelity for correctly assigning the cases without and with an atom in the $F = 2$ manifold is 97.2% and 93.7% respectively, yielding a combined readout fidelity of 95%. Poissonian distributions with the measured mean photon numbers would yield a readout fidelity of 98%. The reduction from the ex-

pected value is mostly due to an increased probability of events with low photon numbers, which we attribute to a finite optical pumping probability out of $F = 2$ during the readout period.

By assuming that the atom escapes the trap once and for all at a certain point in time, we can estimate the likelihood of having had an atom for a certain measurement i, using the combined data from all 100 measurements. From the number of collected photons in each measurement we determine the probability P_i that an atom was present during that specific measurement. Using all probabilities obtained for one atom we calculate the probability $P^L(i)$ that the atom is lost at the i-th measurement.

A typical datasets of 80 measurements on the same atom is shown in Figure B.4. The histogram shows the number of counted photons for each measurement, the blue dots P_i and the red line $P^C(i)$. We typically condition on a probability for the atom to be present of 99.9%. For this particular case it implies the atom is lost at the 38-th pulse.

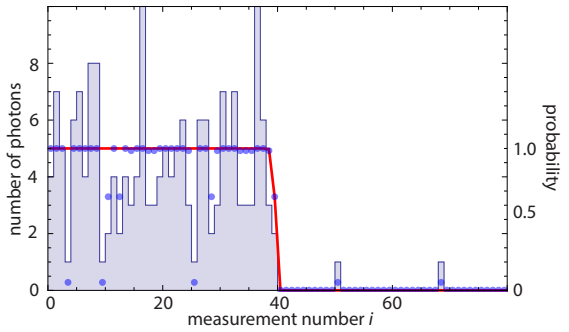

Figure B.4: Determining the presence of a single atom. 80 readout measurements (each consists of 500 24 ns pulses) are performed on the same atom. The histogram shows the number of photons counted per readout measurement. The blue dots show the probability P_i for a single measurement that an atom was present and the red line $P^C(i)$ that an atom was present at the i-th measurement based on all measurements in the dataset (see text).

For the measurements of the atomic spin state the uncoupled state $|u\rangle$ is indistinguishable from having no atom present in the trap. Therefore, for a typical experiment every 4th measurement we optically pump the atom in the $F = 2$ manifold and verify its presence. In case the atom presence is not confirmed we discard all data after the last control measurement where an atom was detected.

For the switching experiments we perform two readout sequences (see Figure B.3) to ensure the atom is in the $\{|u\rangle, |c\rangle\}$ subspace. The first readout sequence projects the atom on either $|u\rangle$ or $|c\rangle$; subsequently, we apply a microwave π-pulse transferring $|u\rangle$ to $|c\rangle$ followed by a second readout pulse. If in either of the two readout sequences the atom is detected the atom is in the $\{|u\rangle, |c\rangle\}$ subspace.

In the data in Figure 2a we can verify the presence of the atom only for certain values of ϕ_V ($-0.3 \leq \phi_V \leq 0.2$ and $0.8 \leq \phi_V \leq 1.2$), where the mean photon numbers in A and D are significantly affected by the presence of an atom. For these values of ϕ_V we determine that in 89% of the cases an atom was present during the first 10 measurements on each atom. We apply a correction of 11% to the other data in Figure 2 obtained at ϕ_V where the contrast was not sufficient to verify the presence of the atom.

B.3 Supplementary discussion

In this section we discuss several aspects of the experiments presented in the main text.

The proximity of a surface can alter the spontaneous emission rate of an atom substantially even in the absence of resonant structures [139]. We estimate the change in spontaneous emission due to the vicinity of the SiN waveguide by performing Finite-Difference-Time-Domain (FDTD) simulations of a dipole located at 180nm from the surface of a waveguide with equal dimensions to our PC. We perform simulations for an un-

patterned waveguide and for a waveguide with holes spaced at 315 nm, corresponding to the mirror sections of the PC but no resonant cavity structure. We find that the maximum Purcell factor for all dipole orientations is $1 \leq P \leq 1.25$, hence only a perturbation compared to the cavity enhanced Purcell effect. In the rest of our analysis we assume $P_{wg} \simeq 1$.

In Figure 1d, we measure the lifetime of the atomic excited state. Given a possible shot-to-shot variation in cooperativity (resulting *e.g.* from atomic motion), fitting a single exponential decay to the data gives a conservative estimate of the fastest decay rate in the ensemble. The data is accumulated over a window that begins 1 ns after the end of the excitation pulse, to ensure that background light from the falling edge of the pulse is excluded. However, this has the effect of systematically biasing the measurement away from fast decay rates. Therefore, the cooperativity of $\eta = 7.7$ measured from the decay rate should be interpreted as a conservative estimate of the maximum cooperativity in an ensemble. We also attribute the linewidth in the inset of Fig. 1d to this effect: the measured linewidth is 43 GHz, while the independently recorded cavity linewidth is 25 GHz (Fig. B.2). We expect non-radiative contributions to the decay of the atomic excited state to be negligible because the imaginary part of the dielectric permittivity of SiN in this wavelength range is small. Additionally, non-radiative decay processes would be represented in the data as a frequency independent decay enhancement, which we do not observe (see Figure 1d).

For the measurements presented in Figure 2 various experimental imperfections contribute to the reduced fringe visibility. The fringe visibility is defined by $(\mathcal{P}_{max} - \mathcal{P}_{min})/(\mathcal{P}_{max} + \mathcal{P}_{min})$, therefore a reduction of *e.g.* $\mathcal{P}_{max}$ of 10% arising from thermal motion reduces the fringe visibility by typically 20%. Imperfect balancing of the interferometer accounts for 5% reduction of the visibility, which we extract from the measurements

without an atom. Additional reduction can arise from finite saturation. To estimate the influence of saturation we have performed a measurement similar to Figure 2a at $\phi_V = \pi$ and an 8 times smaller driving intensity. We observe a maximum signal in the A port of $\mathcal{A}_1/\mathcal{P}_1 = 85\%$, compared to 75% as shown in Figure 2.

In our experiment the magnetic field axis is aligned orthogonal to the linearly polarized cavity field. Therefore, linearly polarized photons emitted into the cavity mode can leave the atom in a final state different from the initial state and reveal which-path information in the interferometer and therefore reduce the fringe visibility. We estimate this contribution to be $\sim 10\%$ of the scattering events. This effect can be suppressed by aligning the magnetic field axis and the cavity field polarization. The same effects are present in the measurements presented in Figure 4 where such scattering events move the atom out of the $\{|u\rangle, |c\rangle\}$ subspace.

Additional reduction of the fringe visbility could arise from positioning uncertainty of the atom with respect to the cavity mode (*e.g.* from thermal motion of the atom in the dipole trap) that gives rise to a fluctuating η. The cavity mode is a standing wave along the cavity axis and the effect of position uncertainty on our measurements depends strongly on the precise distribution of positions. Assuming complete uncertainty in the position along the cavity axis we estimate that this does not account for more than 20% in reduction of the fringe visibility.

In Figure 4 we typically route $\bar{n}_A = 6.2$ photons which is optimized to have a high readout fidelity and minimal heating of the atom, thereby increasing the number of repetitions of the experiment with the same atom. In the same configuration we have routed up to $\bar{n}_A = 14$ photons per readout pulse and in an unmodulated trap we have routed up to $\bar{n}_A \simeq 75$ detected photons after which the atom is optically pumped to the $F = 1$ manifold with $\sim 50\%$ probability.

In Figure 4b we present two datasets with an applied gate field: one where the switch state (P_{on}) is conditioned on having detected at least one gate photon, and one where it is not conditioned. The readout of the switch state is triggered by the arrival of a gate photon in a broad time window. The conditioned and unconditioned datasets are extracted from the same measurement by dividing the events based on the arrival time of the gate photon. If the gate photon arrived during one of the 24 ns pulses, then the measurement was included in the conditioned dataset. Otherwise, the photon is assumed to be a background event uncorrelated with the gate field, and the measurement is included in the unconditioned dataset. Careful analysis of the arrival times shows that about 70% of the background events are fluorescence from the dipole trap, while 30% are actually leaked gate photons that arrive at the wrong time. Since most of these photons arrive at times when the dipole trap intensity is high, they are mostly detuned by more than $\eta\gamma$, on average, and can be safely approximated as background events.

Finally, in Figure 4c an additional reduction of the fidelity arises from a combination of imperfect internal state preparation and readout, dephasing and microwave-pulse accuracy. All these effects are present in the data without a gate field (red curve) and amount to a maximum reduction of the fidelity of $\sim 10\%$.

B.4 Theoretical analysis

In this section, we outline the theoretical framework used to analyze our experimental observations.

B.4.1 Theoretical model

We consider an atom interacting with a single mode, single sided optical cavity. In a frame rotating with the incident laser, the Hamiltonian governing the atom-cavity dynamics is:

$$H_{\rm ac} = \frac{1}{2}\Delta_a\sigma_z + \Delta_c a^\dagger a + g(a^\dagger\sigma + a\sigma^\dagger), \tag{B.3}$$

where σ and a are the atomic and photonic lowering operators, σ_z is the atomic pseudo spin operator, $\Delta_a = \omega_a - \omega_L$ and $\Delta_c = \omega_c - \omega_L$ are the detunings between the bare atomic (ω_a), cavity (ω_c) and laser (ω_L) frequencies, and $2g$ is the single-photon Rabi frequency. Note that $\Delta_a = -\delta$ in the main text. In the presence of atomic excited state decay (γ) and cavity decay into the waveguide (κ_{wg}) and into other dissipation channels (κ_{sc}) the quantum dynamics is governed by Heisenberg-Langevin equations of motion [140]:

$$\dot{a}(t) = -ig\sigma(t) - (\kappa/2 + i\Delta_c)a(t) - \sqrt{\kappa_{wg}}a_{wg,in}(t) - \sqrt{\kappa_{sc}}\xi_{sc}(t) \tag{B.4}$$

$$\dot{\sigma}(t) = iga(t)\sigma_z(t) - (\gamma/2 + i\Delta_a)\sigma(t) + \sqrt{\gamma}\xi_{at}(t)\sigma_z(t) \tag{B.5}$$

$$\dot{\sigma_z}(t) = -2ig(\sigma^\dagger(t)a(t) - \sigma(t)a^\dagger(t)) - \gamma(\sigma_z(t) + 1) - 2\sqrt{\gamma}\xi_{at}^\dagger(t)\sigma(t) - 2\sqrt{\gamma}\sigma^\dagger(t)\xi_{at}(t) \tag{B.6}$$

where $a_{wg,in}(t)$ is the input field operator representing the cavity-waveguide coupling and $\xi_{sc}(t)$ and $\xi_{at}(t)$ are noise operators corresponding to other cavity dissipation channels and atomic spontaneous emission into other modes, respectively. The cavity output field is described by the input-output relation:

$$a_{wg,out}(t) - a_{wg,in}(t) = \sqrt{\kappa_{wg}}a(t) \tag{B.7}$$

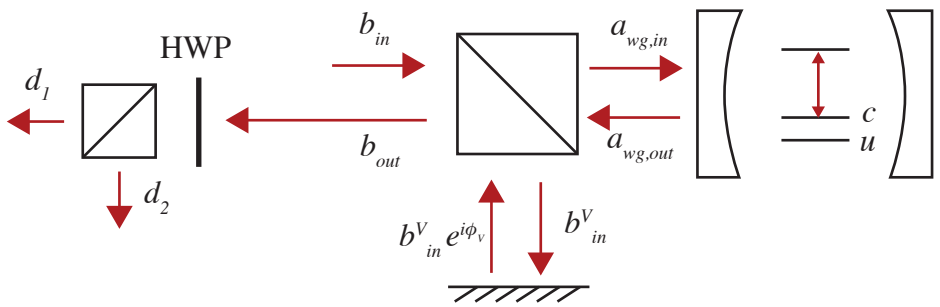

Figure B.5: Modes at various points in the interferometer, as used in section B.4.

Following the notations defined in Fig. B.5, the interferometer input and output fields $\vec{b}_{in}$, $\vec{b}_{out}$ are:

$$\vec{b}_{in} = b^H_{in}\hat{\epsilon}_h + b^V_{in}\hat{\epsilon}_v \tag{B.8}$$

$$\vec{b}_{out} = (b^H_{in} + \sqrt{\kappa_{wg}}a)\hat{\epsilon}_h + b^V_{in}e^{i\phi_V}\hat{\epsilon}_v \tag{B.9}$$

where $\hat{\epsilon}_{h/v}$ are unit vectors denoting horizontal and vertical polarization. Here, we have treated the action of the V-polarized reference arm as perfect reflection with a phase shift ϕ_V. Using a HWP to orient the detection basis at an angle θ' with respect to the H axis, the fields at the two detectors are given by:

$$d_1 = \vec{b}_{out} \cdot (\cos\theta'\hat{\epsilon}_h + \sin\theta'\hat{\epsilon}_v) \tag{B.10}$$

$$d_2 = \vec{b}_{out} \cdot (-\sin\theta'\hat{\epsilon}_h + \cos\theta'\hat{\epsilon}_v) \tag{B.11}$$

If the input field is linearly polarized at an angle θ with respect to the H axis, then we can define two input modes b_s and b_v such that $\vec{b}_s = b_s(\cos\theta\hat{\epsilon}_h + \sin\theta\hat{\epsilon}_v)$ and $\vec{b}_v = b_v(-\sin\theta\hat{\epsilon_h} + \cos\theta\hat{\epsilon_v})$. The mode b_v is orthogonal to the input field and is not driven.

In practice, we fix $\theta' = \pi/4$ and adjust θ to compensate for the effects of cavity losses and finite reflectivity in the V-polarized arm of the interferometer, as discussed in the next section. In this case, the output modes are given by:

$$d_1 = A_1 b_s + a\sqrt{\frac{\kappa_{wg}}{2}} + C_1 b_v \tag{B.12}$$

$$d_2 = A_2 b_s - a\sqrt{\frac{\kappa_{wg}}{2}} + C_2 b_v \tag{B.13}$$

with $A_1 = (\cos\theta + e^{i\phi_V}\sin\theta)/\sqrt{2}$, $A_2 = (-\cos\theta + e^{i\phi_V}\sin\theta)/\sqrt{2}$, $C_1 = (e^{i\phi_V}\cos\theta - \sin\theta)/\sqrt{2}$ and $C_2 = (e^{i\phi_V}\cos\theta - \sin\theta)/\sqrt{2}$. Note that for $\theta = \pi/4$ and $\phi_V = 0$ these equations are identical to the input-output relations for a symmetric cavity driven from one side by b_s and from the other side by b_v.

B.4.2 Linear response

When the driving field is weak, the atom is nearly always in its ground state and we can approximate the action of the operator $a\sigma_z$ with $-a$. In this case, the expectation values of Eq. (B.4-B.5) form a closed system of differential equations that we can solve exactly to find the response to a slowly-varying incident coherent field $\langle a_{wg,in}\rangle$:

$$\langle a\rangle = \frac{-\sqrt{\kappa_{wg}}}{\tilde{\kappa}} \frac{\langle a_{wg,in}\rangle}{1+\frac{g^2}{\tilde{\kappa}\tilde{\gamma}}} \tag{B.14}$$

$$\langle \sigma\rangle = \frac{ig\sqrt{\kappa_{wg}}}{\tilde{\kappa}\tilde{\gamma}} \frac{\langle a_{wg,in}\rangle}{1+\frac{g^2}{\tilde{\kappa}\tilde{\gamma}}} \tag{B.15}$$

where we have introduced complex decay rates $\tilde{\kappa} = \frac{\kappa}{2} + i\Delta_c$ and $\tilde{\gamma} = \frac{\gamma}{2} + i\Delta_a$, and defined the cooperativity $\tilde{\eta} = g^2/\tilde{\kappa}\tilde{\gamma}$. On resonance, it reduces to $\eta = 4g^2/\kappa\gamma$. The reflected field

from the cavity is given by Eq. B.7:

$$\langle a_{wg,out}\rangle = \langle a_{wg,in}\rangle \frac{\tilde{\kappa}(1+\tilde{\eta}) - \kappa_{wg}}{\tilde{\kappa}(1+\tilde{\eta})} \rightarrow \langle a_{wg,in}\rangle \frac{\eta - 1}{\eta + 1}, \tag{B.16}$$

where the final limit is taken on resonance and with $\kappa_{wg} = \kappa$. This expression captures the key result of the atom-photon interaction: the reflection coefficient of the cavity changes from -1 to $+1$ in the presence of a strongly coupled atom with $\eta > 1$.

The output fields at the two ports of the interferometer are given by Eq. (B.12-B.13). For the data presented in the paper, the angle θ was chosen to null the light in one port (d_1) in the absence of an atom, with the probe field on resonance with the cavity. This is accomplished when $\tan\theta = (2k-1)$, with $k = \kappa_{wg}/\kappa$. For this choice of θ the d_1 and d_2 ports correspond to the A and D ports in the main text respectively. The output field is given by:

$$\langle d_1\rangle = \frac{\langle b_s\rangle}{2\sqrt{1+2k(k-1)}} \frac{(e^{i\phi_V}(2k-1)+1)(1+\tilde{\eta}) - \kappa_{wg}/\tilde{\kappa}}{1+\tilde{\eta}} \rightarrow \langle b_s\rangle \frac{\eta}{1+\eta} \tag{B.17}$$

$$\langle d_2\rangle = \frac{\langle b_s\rangle}{2\sqrt{1+2k(k-1)}} \frac{(e^{i\phi_V}(2k-1)-1)(1+\tilde{\eta}) + \kappa_{wg}/\tilde{\kappa}}{1+\tilde{\eta}} \rightarrow \langle b_s\rangle \frac{1}{1+\eta}, \tag{B.18}$$

where the final expression is evaluated on resonance with $k = 1$ and $\phi_V = 0$. In this case, the fields at the ports d_1 and d_2 are identical to the reflection and transmission outputs of a symmetric cavity with an atom. Within this linear approximation, the intensity at the output ports is given by $\langle d_1^\dagger d_1\rangle = |\langle d_1\rangle|^2$.

Figure B.6 shows the output power of the interferometer on resonance ($\Delta_a = \Delta_c = 0$) versus cooperativity, both without losses (red, $k = 1$) and with losses for our cavity parameters (blue, $k = 0.8$). At $\eta = 1/k$ the cavity reflection vanishes, and the interferometer reflection is 0.5. In the absence of an atom ($\eta = 0$) the cavity reflection is determined by

the cavity losses. For an atom strongly coupled to the cavity ($\eta \gg 1$) the light is blocked from entering the cavity, therefore the cavity losses are suppressed. For our parameters ($\eta \simeq 8$) the reflection on resonance without an atom is $|\langle d_1\rangle|^2 + |\langle d_2\rangle|^2 = 0.35$ and is expected to increase by $(|\langle d_1\rangle|^2 + |\langle d_2\rangle|^2)_{\eta=8}/(|\langle d_1\rangle|^2 + |\langle d_2\rangle|^2)_{\eta=0} = 1.46$ due to the presence of an atom. The expected maximum fraction of the power switched from D to A is $|\langle d_1\rangle|^2/(|\langle d_1\rangle|^2 + |\langle d_2\rangle|^2) = 0.97$.

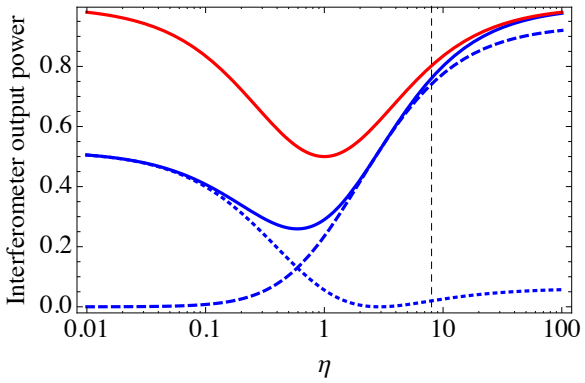

Figure B.6: Interferometer output as a function of cooperativity given by Eq. B.17 and B.18. The red solid curve shows the total power in the absence of cavity losses, blue dashed, dotted and solid lines show the power $|\langle d_1\rangle|^2$, $|\langle d_2\rangle|^2$ and $|\langle d_1\rangle|^2 + |\langle d_2\rangle|^2$ respectively including cavity losses of $k = 0.8$.

B.4.3 Saturation behavior

The treatment above made use of the approximation $\langle\sigma_z\rangle \approx -1$. This is valid for input field amplitudes such that the excited state population $\sim \langle\sigma^\dagger\sigma\rangle$ remains small:

$$\langle\sigma^\dagger\sigma\rangle \approx |\langle\sigma\rangle|^2 = \frac{\kappa_{wg}}{|\tilde{\kappa}\tilde{\gamma}|^2}\frac{g^2}{|1+\tilde{\eta}|^2}|\langle a_{wg,in}\rangle|^2 \ll 1. \tag{B.19}$$

In the limit of large η and neglecting other cavity loss channels, this corresponds to $|\langle a_{wg,in}\rangle|^2 \ll \eta\gamma/2$. That is, the rate of incident photons should be much less than one per excited state lifetime.

For stronger input fields, this approximation breaks down due to atomic saturation. This has two consequences. First, we can no longer make the approximation $\langle\sigma_z\rangle \approx -1$. Second, we can no longer factor expectation values of operator products. To describe saturation dynamics of our system, we make use of the hierarchy of our experimental parameters ($\kappa \gg (g,\gamma)$), which allows us to integrate out the cavity degree of freedom. Following [141], in the limit of large κ we find:

$$a(t) = \left[-ig\sigma(t) - \sqrt{\kappa_{wg}}a_{wg,in}(t) - \sqrt{\kappa_{sc}}\xi_{sc}(t)\right]/\tilde{\kappa} \tag{B.20}$$

which yields the following atomic dynamics (assuming vacuum for the ξ_{sc} and ξ_{at} operators):

$$\dot{\langle\sigma\rangle} = -\left(\tilde{\gamma} + \frac{g^2}{\tilde{\kappa}}\right)\langle\sigma\rangle - \frac{ig}{\tilde{\kappa}}\sqrt{\kappa_{wg}}\langle a_{wg,in}\rangle\langle\sigma_z\rangle \tag{B.21}$$

$$\dot{\langle\sigma_z\rangle} = -\left(\gamma + \frac{g^2\kappa}{|\tilde{\kappa}|^2}\right)(\langle\sigma_z\rangle + 1) + 2ig\sqrt{\kappa_{wg}}\left(\frac{\langle\sigma^\dagger\rangle\langle a_{wg,in}\rangle}{\tilde{\kappa}} - \frac{\langle\sigma\rangle\langle a^\dagger_{wg,in}\rangle}{\tilde{\kappa}^*}\right). \tag{B.22}$$

Focusing on the resonant cw case ($\Delta_a = \Delta_c = 0$) and introducing a dimensionless amplitude of the driving field $Y = \frac{4g}{\kappa\gamma}\sqrt{\kappa_{wg}}\langle a_{wg,in}\rangle$, we find the following steady state solution:

$$\langle\sigma\rangle = \frac{iY(1+\eta)}{2Y^2 + (1+\eta)^2} \tag{B.23}$$

$$\langle\sigma_z\rangle = \frac{-(1+\eta)^2}{2Y^2 + (1+\eta)^2}. \tag{B.24}$$

Choosing $\tan\theta = 2k - 1$ and $\phi_V = 0$ again, we find for the output ports of the

interferometer:

$$\langle d_1^\dagger d_1 \rangle = \frac{\gamma}{2\eta} k Y^2 \frac{\eta^2}{2Y^2 + (1+\eta)^2} \tag{B.25}$$

$$\langle d_2^\dagger d_2 \rangle = \frac{\gamma}{2\eta} k Y^2 \frac{(2Y^2+1)(1-2k)^2 + 2(1-k)(1-2k)\eta + (1-k)^2\eta^2}{k^2(2Y^2 + (1+\eta)^2)}. \tag{B.26}$$

The dimensionless driving intensity is $Y^2 = \frac{4\eta}{\gamma} k |b_s|^2 \cos^2\theta$, in terms of the input field intensity $|b_s|^2$ (which has units of photons/second).

The two-photon correlation functions are calculated using:

$$g_i^2(\tau) = \frac{\langle d_i^\dagger(t) d_i^\dagger(t+\tau) d_i(t+\tau) d_i(t) \rangle}{\langle d_i^\dagger(t) d_i(t) \rangle^2} \tag{B.27}$$

with the operator d_1 for the A port, and d_2 for the D port. The time dependence has been worked out analytically for the case of a double sided cavity in the bad cavity limit in Ref. [140]. Here, we calculate $g^2(\tau)$ numerically from the master equation using the Hamiltonian (B.3) together with the quantum regression theorem [140].

The data in Figure 3 was taken in the presence of the dipole trap which imposes a position-dependent AC-Stark shift, which fluctuates because of the finite kinetic energy of the atom. To account for this effect, we average equations (B.25−B.27) over a Gaussian distribution of atomic detunings with a standard deviation of 60 MHz. The resulting averaged intensities and correlation functions are shown as the solid lines in Figure 3. We estimate the maximum differential light shift between the ground and excited state in our trap to be ~ 130 MHz. In the normalization of the averaged $g^2(\tau)$ we account for the detuning-dependent intensity at the detector, with the assumption that the timescale on which the detuning fluctuates is much faster than the window over which photon data is accumulated (tens of ms) but slower than the excited state dynamics in Figures 3b-c.

B.4.4 Analysis of the quantum phase switch

In this section we consider the effect of imperfections such as photon loss and multiphoton excitations on the operation of the quantum phase switch.

Photon loss is included in the Heisenberg-Langevin equations (B.4 - B.6) in the form of coupling to three photonic modes: the waveguide mode a_{wg}, a second cavity loss mode ξ_{sc}, and a spontaneous emission mode ξ_{at}. For low input intensities, with less than one photon per bandwidth, the optical response is linear. In this case the combined evolution of the atomic and photonic systems can be represented as:

$$U = \sum_{i,j} \left(r_{ij,c} \left| c \right\rangle \left\langle c \right| + r_{ij,u} \left| u \right\rangle \left\langle u \right| \right) a_i^\dagger a_j, \tag{B.28}$$

where $r_{ij,c}$ and $r_{ij,u}$ denote the scattering amplitudes coupling modes i, j, with an atom in the coupled or uncoupled states. a_i corresponds to one of the modes $\{a_{wg}, \xi_{sc}, \xi_{at}\}$. The scattering amplitudes can be found by using input-output relations similar to Eq. (B.7) for the modes ξ_{sc} and ξ_{wg}, together with the linear response as described in B.4.2. Since only the mode a_{wg} is driven, the important terms are the coefficients for $a_{wg}^\dagger a_{wg}$, $\xi_{sc}^\dagger a_{wg}$ and $\xi_{at}^\dagger a_{wg}$, which we denote as r_i, t_i and l_i, respectively, with the appropriate atomic state subscript. They obey $|r_i|^2 + |t_i|^2 + |l_i|^2 = 1$. These are related to microscopic param-

eters of the system as follows:

$$r_u = 1 - \frac{\kappa_{wg}}{\tilde{\kappa}} \tag{B.29}$$

$$r_c = 1 - \frac{\kappa_{wg}}{\tilde{\kappa}(1+\tilde{\eta})} \tag{B.30}$$

$$t_u = -\frac{\sqrt{\kappa_{sc}\kappa_{wg}}}{\tilde{\kappa}} \tag{B.31}$$

$$t_c = t_u/(1+\tilde{\eta}) \tag{B.32}$$

$$l_u = 0 \tag{B.33}$$

$$l_c = \frac{ig\sqrt{\gamma\kappa_{wg}}}{\tilde{\gamma}\tilde{\kappa}(1+\tilde{\eta})} \tag{B.34}$$

For an initial atomic state $|\psi_{in}\rangle = |+\rangle = (|u\rangle + |c\rangle)/\sqrt{2}$ and a coherent state α in a_{wg}, the output state is:

$$|\psi_{out}\rangle = \left(|u, r_u\alpha, t_u\alpha, l_u\alpha\rangle + |c, r_c\alpha, t_c\alpha, l_c\alpha\rangle\right)/\sqrt{2}, \tag{B.35}$$

where the output state is labeled by the atomic state and the three coherent state amplitudes in the output modes $\{a_{wg}, \xi_{sc}, \xi_{at}\}$. If we detect at least one photon in the mode a_{wg}, then the conditional state of the system $|\psi_{out}^{cond}\rangle \sim a_{wg}\,|\psi_{out}\rangle$ is given by:

$$|\psi_{out}^{cond}\rangle = \frac{1}{\sqrt{|r_u\alpha|^2 + |r_c\alpha|^2}}\left(r_u\alpha\,|u, r_u\alpha, t_u\alpha, l_u\alpha\rangle + r_c\alpha\,|c, r_c\alpha, t_c\alpha, l_c\alpha\rangle\right). \tag{B.36}$$

Since the residual photons in all three modes are eventually measured or lost to the environment, the state of the system in both the unconditioned and conditioned cases can be described by tracing over all photon modes. This results in the reduced density matrix for

the atom:

$$\rho_{out} = \frac{1}{2}\begin{pmatrix} 1 & D \\ D^* & 1 \end{pmatrix} \tag{B.37}$$

$$\rho_{out}^{cond} = \frac{1}{(|r_u|^2 + |r_c|^2)}\begin{pmatrix} |r_u|^2 & Dr_c^* r_u \\ D^* r_u^* r_c & |r_c|^2 \end{pmatrix} \tag{B.38}$$

$$D = \langle r_c\alpha, t_c\alpha, l_c\alpha | r_u\alpha, t_u\alpha, l_u\alpha\rangle \tag{B.39}$$

where D is the overlap between the output photonic states, which scales as $e^{-|\alpha|^2}$. Now we calculate two fidelities, quantifying the extent to which we leave the input state untouched without conditioning (P^{unc}), and the overlap with the target output state with conditioning (P^{cond}). These two quantities are related to the visibility of the green and blue curves in Fig. 4 of the main text, respectively. They are given by:

$$P^{uncond} = \langle +|\rho_{out}|+\rangle = \frac{1}{2}(1 + \mathrm{Re}[D]) \tag{B.40}$$

$$P^{cond} = \langle -|\rho_{out}^{cond}|-\rangle = \frac{1}{2(|r_u|^2 + |r_c|^2)}\left(|r_u|^2 + |r_c|^2 - \mathrm{Re}[Dr_c^* r_u]\right). \tag{B.41}$$

These expressions can be easily generalized to evaluate an overlap with arbitrary atomic state.

To illustrate the combined effect of photon loss and multiphoton excitations, we set $r = r_u = -r_c$. Even in the presence of losses ($k < 1$) this case is experimentally achievable by balancing the cavity losses with a finite cooperativity. In this case, the conditional and unconditional fidelities become the same: $P^{uncond} = P^{cond} = \frac{1}{2}(1 + D)$. Additionally, if

$\eta \gg 1$, D takes a simple form such that:

$$P^{uncond} = P^{cond} = \frac{1}{2}(1 + e^{-(1+r^2)|\alpha|^2}). \tag{B.42}$$

Note that while a lower α results in a higher conditional fidelity, it also decreases the probability of successfully flipping the switch, which scales as $P = 2\epsilon\eta_c r^2/(1+r^2)$, where η_c is the total detection efficiency of reflected photons and $\epsilon = P^{cond} - 1$ is the error of the gate operation.

For our experimental parameters ($k = 0.8$, $\eta \simeq 8$ and $|\alpha|^2 = 0.6$) we estimate a gate fidelity from (B.41) of $P^{cond} = 0.79$ and $P^{uncond} = 0.80$ on resonance, mostly limited by the relatively large $|\alpha|^2$. Additional reduction of the fidelity arises from spontaneous scattering events by the gate photon leaving the atom in a different hyperfine sub-level than $|c\rangle$ ($\sim 10\%$) and from imperfect hyperfine state preparation and readout ($\sim 10\%$) as discussed in section B.3.

Finally, implicit in this discussion is the assumption that the reflected H- and V-polarized photons occupy the same temporal mode, so the photon arrival time does not contain any which-path information for the photon. Since the V-polarized interferometer arm is just a mirror, this requires the response time of the atom-cavity system to be instantaneous as well, in the sense that the intracavity field must equilibrate to its steady-state value on a timescale that is short compared to the duration of the input pulse. In our experiment, the bandwidth of the coupled atom-cavity system is given by $\eta\gamma$. Thus, as long as the temporal mode containing the input photon is much longer than the inverse of this rate, the output mode should be identical to the input mode and the gate will operate as expected. In practice, we use gaussian pulses of duration 24 ns (FWHM), which is not quite long enough to fully neglect retardation in the atomic dynamics. We

estimate that this introduces imperfections at a level of less than 10%.

Appendix C

Fabrication procedures

This appendix provides a fairly detailed listing of the fabrication procedures used to make the photonic crystal cavities for the experiments presented here, as well as a few things that didn't work.

C.1 Photonic crystal fabrication

1. **Substrate procurement** The fabrication begins with the desired thickness of silicon nitride deposited via LPCVD onto a 100 mm $\langle 100 \rangle$ silicon substrate. We have this done commercially by Rogue Valley Microdevices, or Silicon Valley Microelectronics Industries. The nitride should be "stoichiometric" and have a refractive index of 2.0, which also implies that it will have a high tensile stress of ≈ 1 GPa. We like to have the substrate scored on the backside with a 1cm grid, without cutting completely through. This allows us to do some processing steps (cleaning, resist spinning) on an entire wafer, and then to cleanly break it apart into smaller pieces as desired by simply tapping it with tweezers. The ideal scoring depth for this process is about halfway through the wafer, or 250 μm for a 500 μm thickness wafer. This can be done by SVMI, or afterwards by American Precision Dicing. In a bind,

it can also be done on our dicing saw SW-1.

2. **Substrate preparation** Shortly before the next step, the substrate should be cleaned thoroughly. We use the following procedure: 10 minutes in piranha (3:1 sulfuric acid to hydrogen peroxide), 2x DI rinse, blow dry (from DI), then 5 minutes in an O_2 plasma (RIE-5) at 20 sccm. flow with 150 W of RF power.

3. **E-beam resist** The substrate (still a wafer) is baked on a hotplate at 180C for 5 minutes to drive off water, then spun at 3,000 rpm with ZEP520A electron-beam lithography resist, and baked for 2 minutes at 180C. The resulting film thickness should be about 450 nm (see ZEP data sheet for spin curves).

At this point, a subset of the wafer is broken off and processed to produce devices. We have found that we can use pieces of the same wafer (without re-spinning resist) for more than 6 months with no significant change in exposure or development characteristics. Or, to state our results more precisely, we have not found that the variation between a freshly spun wafer piece and a 6 month old one is any more than the variation between two freshly spun pieces.

1. **E-beam exposure** Expose wafer piece in Elionix F125 (EL-5) e-beam lithography machine. A piece usually comprises either 2x2 or 4x1 1 cm^2 chips, on which we write identical patterns. For a long time, we used a 150 μm write field, 20k dots, 1 nA of beam current and 260 ns/dot exposure. More recently, we found that the cavity Qs go up if we use more dots*, so now we use 150 μm field, 60k dots, 300

*At the lower dot setting, high resolution SEM images of the final structures revealed that the hole spacing (lattice constant) varied along the device in a way that was suggestive of pixelization. In addition to going to a higher dot setting on the e-beam writer, we also switched from square to circular (ellipsoidal) holes, with the idea that these would be less sensitive to pixel boundaries. At the 60k dot setting, there is still a faint trace of pixelization visible in the SEM images, but it is much smaller and arguably within the noise of the SEM images.

ption A of beam current and 100 ns/dot (which gives roughly the same charge density as the old settings). We have not explored whether going to even finer resolution improves things, because it would become impractical to write large arrays with finer resolution. A workaround would be to use a two-step writing process, which would require markers for alignment.

2. **Development** The wafer piece is developed in o-xylene for 60 s (lightly agitated by rocking the cup back and forth), followed by a 15 s rinse in IPA (same conditions) and blown dry (from IPA).

3. **Reactive Ion Etch** The pattern is transferred from the resist to the silicon nitride using a reactive ion etch in the STS ICP RIE system (RIE-8). The etch recipe is 130/80 sccm of C_4F_8/SF_6 at 10 mtorr, with 1000 W of ICP RF power and 30 W of platen RF power. The platen temperature is held at 15 C. Before running an actual sample through the etcher, we first condition the chamber with a 15 minute O_2 plasma (standard CNS parameters are XX sccm O_2, 800/XX W of RF power, 45 mtorr) followed by 45 minutes with the actual etch recipe. Then, we measure the etch rate with a 1 minute etch performed on a silicon nitride test chip, using the ellipsometer to measure the film thickness after the etch. The etch rate varies from 110 - 120 nm/min. The measurement of the etch rate is used to adjust the etch time on the real samples, to keep the nominal etch depth constant. The nominal etch depth is typically 150% of the film thickness. The color of the resist film after the etch should be recorded, and is a sensitive probe of whether anything has changed from run-to-run.

4. **Cleaning** The remaining resist is stripped with at least 10 minutes immersion in the solvent NMP (N-Methyl-2-pyrrolidone), either pure (stocked in our wet lb) or

in the form of Remover PG or Remover 1165 (proprietary NMP-based mixtures stocked in the solvent bench in the cleanroom). The chips are then rinsed in DI and dried (from DI). The drying can be skipped if the chips can be deposited directly into the KOH bath in the next step.

5. **KOH Undercut** The silicon underneath the nanobeams is now removed using an anisotropic wet etch solution consisting of 10 mL DI, 2 g KOH pellets (potassium hydroxide), and 400 μL IPA. The solution should be at a temperature of 80 C, and covered to prevent evaporation during the long etch time. We typically put three small beakers inside one large beaker filled with water on a hotplate, and then use a thermometer to measure the temperature of the water bath. One of the small beakers contains the KOH solution, and the others contain heated DI water to use as a rinse bath. It is essentially impossible to remove all of the KOH with a room temperature rinse, resulting in crystals on the surface of the chip after drying. The etch time in the KOH will depend somewhat on the structures being made, but we typically use 20 - 30 minutes followed by 5 minutes in each of the two water baths. It is important that the water baths be changed if multiple batches of wafers are to be processed, because the amount of KOH transferred by the chip and tweezers is significant. After both baths, the chips are transferred to a jar of DI water (at room temperature). Drying them at this point would destroy the structures[†].

6. **Cleaning** The jar of DI water is used to transfer the chips back into the cleanroom, where they are again cleaned for 10 minutes in piranha (3:1 sulfuric acid to hydrogen peroxide) and rinsed in two DI baths for 30s each. Then they go back

[†]At least, it will destroy the hockey-stick beams that we use for the experiment. Straight-across waveguides clamped on both sides can survive blow drying, because the nitride film stress is high enough to keep them from bending past the point of failure. In curved or singly-clamped structures, however, this stress is relieved.

into the water jar.

7. **Critical point drying** From the water jar, the chips are transferred into a jar of ethanol, and then installed in the critical point drying machine in B15A (CPD-3). To ensure cleanliness, it is advisable to fill the CPD chamber with ethanol and pipette it all out once before filling it again and installing the chip. The machine settings do not matter too much–in particular, it is not necessary to use a purge time longer than 5 minutes, because our structures have comparatively large openings.

After drying, the photonic crystals are finally free and can be characterized. If they are not good, go back to the e-beam step. If they are to be used in the experiment, then the following section describes the procedures for depositing absorbing material on them to tune the resonances.

C.2 Heaters for tuning the cavity resonances

In the experiment, the photonic crystals are tuned by heating them with a laser. We accomplish this using an absorbing material deposited on the waveguide itself, at the end opposite the fiber. In this way, the poor thermal conductance of the photonic crystal itself (arising from its small cross-sectional area) allows a relatively small amount of absorbed power to produce a large increase in temperature. The thermal conductivity of the fiber is so good in comparison to the waveguide that it can be thought of as a heat sink at room temperature: the amount of power required to produce a thermal gradient across the fiber is orders of magnitude higher. We do not have a very accurate measure of the thermal coefficient of the cavity resonance (because it is difficult to know precisely the

temperature of the photonic crystal), but we estimate it to be in the ballpark of 5 pm/K, or 0.5 nm for every 100 K temperature increase.

The challenge with depositing absorbing material onto the waveguide is that the final processing steps are a KOH bath and an acid clean (piranha), and one of them or the other will remove basically anything (see [142] for a table of things that won't work). The only exception is gold, which is very inert, so this was what we tried first, by doing photolithograph and lift-off after RIE but before undercutting to deposit 2 μm-wide stripes of gold perpendicular to the array of waveguides, on the side opposite the fiber coupling. We used about 10 nm of gold with a 3 nm Cr adhesion layer, both thermally evaporated. The metal films can survive all of the subsequent processing steps as described above, although we found that it was better to make the piranha gentler by using a 10:1 acid:peroxide ratio and heating the solution on a hotplate to 80 C (it is no longer appreciably self-heating at this ratio).

The gold heaters worked great: it was possible to use only a few microwatts of power into the waveguide to shift the cavity resonance by up to 2 nm[‡]. However, beyond that point, the cavities are irreversibly damaged: a large blue-shift of the resonance occurs, and the Q is reduced to only a few thousand. While initially we thought that we could avoid this problem by controlling the amount of laser power, it eventually became clear that this degradation process also happens at lower temperatures, just more slowly. Using controlled experiments in a furnace, we observed reductions in the Q after only 1 hour at 250 C. We were able to trace this problem to gold diffusion along the surface of the waveguide, because it can be reversed by immersing the chip containing the cavities briefly in gold etching solution. The extreme mobility of gold ions even at low temperatures is well-known in the semiconductor industry (see Refs. [143, 144] for a foothold

[‡]Absorbing light is perhaps the only useful application of plasmonics.

into the literature, though most of it is about diffusion into the bulk rather than along surfaces). Rather than try to fix that problem, we moved on to finding non-gold solutions, which required new deposition techniques because the material would have to be deposited *after* undercutting the waveguides, when it is no longer possible to spin resist.

Using the techniques described in the following section, we currently use electron-beam evaporated silicon as an absorbing material for cavity tuning. Unlike the gold heaters, we now send the laser light from the side, because the absorption of light from the waveguide is very small with the silicon heaters (compared to essentially 100% for gold).

An alternative approach would be to absorb the light directly in the waveguide. Although silicon nitride itself has increasing absorption towards the blue/UV part of the spectrum, we discovered early on that this causes problems when trapping atoms (see Appendix A). We also tried heating with green light, which worked with quite high powers (¿ 1 mW into the waveguide, via the fiber), but we found that over a timescale of a few minutes the absorption appears to increase in a runaway fashion, eventually leading to a catastrophic event of some type that results in an irreversible shift in the cavity resonance, and a significant degradation in the cavity quality factor. The nitride is very non-absorbing in the NIR, and additionally we would be concerned about light in this spectral region impacting the atoms. One idea in this direction that we did not try is using a CO_2 laser at 10.6 μm wavelength, for which both glass and silicon nitride should be quite absorbing. This would require replacing a window on the vacuum chamber.

C.3 Using nano-stencils for patterned material deposition

The solution that we developed to deposit arbitrary materials is to fabricate a stencil out of a silicon nitride membrane, align it on top of the chip with the waveguides, and deposit

material through the holes in the stencil. Some work with nano-stencils had been done previously [145, 146], but as far as I know, the ability to align stencils to a substrate with $\approx 1\mu$m accuracy is novel.

The stencil fabrication begins with a double-side polished $< 100 >$ Si wafer coated on both sides with a 200 nm thin film of low-stress LPCVD silicon nitride (residual stress < 50 MPa, $n = 2.x$). Photolithography and reactive ion etching in a SF_6/C_4F_8 plasma are used to pattern the backside nitride with 8 mm square windows and a 10mm grid of lines that will be used to separate individual chips at the end of the process. The dimensions of the separation lines is chosen such that approximately 100 microns of silicon will remain after the wet etch used to release the membranes. Then, the same techniques are used to pattern the stencil features into the front side nitride, with the photolithography aligned to the features already etched on the back side. After removing all resist layers, the wafer is etched in potassium hydroxide (KOH, 20 % w./v. with 4% isopropyl alcohol added) at 80° C for approximately 6 hours until the silicon underneath the membranes have been completely cleared of silicon. During the etch, the wafer is placed in a covered dish on a hotplate with the front side facing down, so the majority of the bubbles produced during the etching can escape and are not trapped under the membranes. After etching, the wafer is rinsed in one hot and one room temperature deionized water (DI) bath, and then immersed in a 3:1 H_2SO_4:H_2O_2 solution to ensure all traces of KOH are removed. Finally, the wafer is cleaned in two DI baths at room temperature and carefully dried with nitrogen applied at an oblique angle so as not to rupture the membranes. After drying, the stencil chips are separated for individual use.

To ensure a minimum gap distance between the stencil and the target substrate, a photoresist annulus is applied to the front side of the stencil, on the areas that are not part of the membrane. This is accomplished by spinning the front side with positive-tone

photoresist (Shipley S1813), baking, and performing a flood exposure from the back side to expose all of the resist above the membrane. After developing, rinsing and drying, the stencils are ready for alignment. It is important to remove any resist edge bead with a razor blade before baking the resist, as this an result in very non-uniform and irreproducible spacer thicknesses.

The alignment and attachment of the stencil to the target substrate is performed in a standard photolithography mask aligner (Karl Suss, MJB4). A transparent plexiglass adapter allows the stencil to be held inverted by the mask vacuum chuck (Fig. C.1a), while the target substrate is attached to a larger carrier wafer with double-sided tape and held on the substrate chuck which can be moved with an $xyz\theta$ stage. Before the stencil and substrate are brought completely into contact, the $xy\theta$ degrees of freedom are roughly aligned to position the sample region of the target substrate completely under the membrane. After this, the target substrate is brought into contact with the stencil and the wedge error correction (WEC) is performed to parallelize the two surfaces. Then the surfaces are brought just out of contact and finer $xy\theta$ alignment is performed. After this, the substrate is lowered and the entire mask chuck is removed from the machine with the stencil still held to it by the mask vacuum. Two small drops of UV-curing epoxy (NOA63) are applied to opposite corners/edges of the stencil, with the goal that as little glue as possible should be present on the front surface of the stencil (Fig. C.1b). We find it easiest to do this using a wooden toothpick. The mask chuck is then re-installed into the mask aligner, and the final alignment is performed by bringing the surfaces into contact, backing off slightly to line up the features, and slowly bringing them together again while adjusting the alignment as necessary (Fig. C.1c). A 60 s flood exposure is used to set the epoxy (which should be exposed to the UV lamp through the transparent plexiglass adapter), and the substrate and stencil are lowered together by disconnecting the

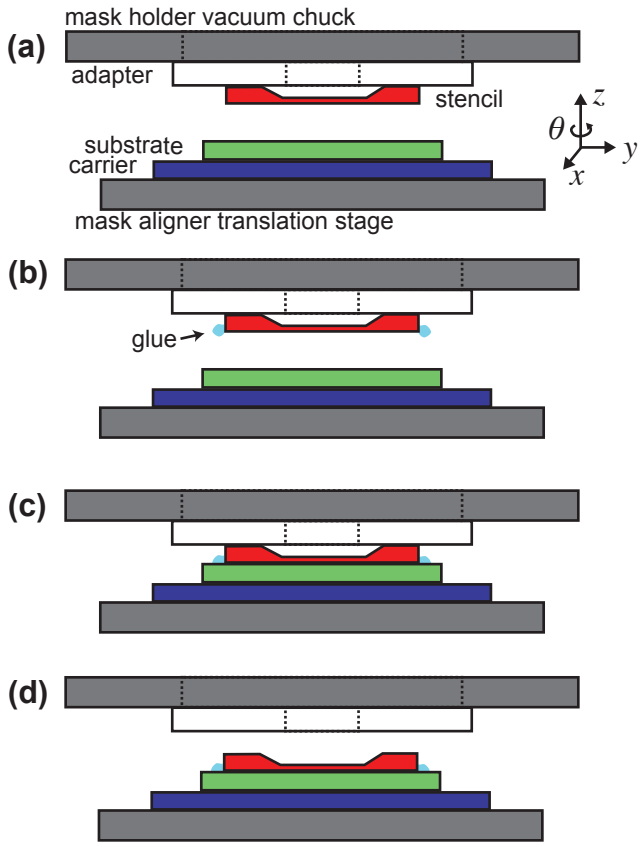

Figure C.1: (a) The initial mask aligner setup showing the target substrate on a carrier wafer, and the stencil attached to the mask holder using a vacuum chuck adapter. The lower stage has $xyz\theta$ translation capabilities, and an optical microscope with 5x - 20x objectives allows the alignment to be observed from the top, through the stencil membrane. (b) Very small drops of UV-curing glue are deposited on two corners of the stencil. The hope is that when the stencil is pressed onto the substrate, most of the glue ends up outside rather than in between. (c) The surfaces are brought together, aligned, and the glue is cured using the UV lamp in the mask aligner. (d) The vacuum line is disconnected from the maskholder, freeing the stencil and allowing the stages to be separated, but now with the stencil glued onto the target substrate.

mask vacuum that was holding the stencil onto the plexiglass adapter. After removing the mask chuck from the machine (Fig. C.1d), several more 60 s flood exposures are applied to completely cure the epoxy. Finally, the sample is removed from the mask aligner by handling the carrier wafer, and installed in a material deposition tool.

After deposition, the mask can be removed from the substrate by using tweezers to pry it off of the surface. A small amount of uncured epoxy usually remains on the substrate, in the area covered by the stencil, and can be removed if necessary with a solvent-coated cleanroom swab.

It is possible to determine the separation and tilt of the stencil and substrate using a non-contact white light profilometer, if sufficiently large (¿10 μm) windows exist in the stencil to allow viewing the substrate underneath directly. We typically achieve separations of 10-15 μm and tilts of less than 1 mrad. We routinely achieve alignment errors of less than 1.5 microns. We believe this accuracy is limited mostly by parallax effects from the mask aligner optics that make it difficult to reliably line up the stencil and alignment marks when they are separated by 10 μm vertically.

We have used this technique to deposit numerous metals and silicon (amorphous) using thermal or electron beam evaporation.

Deposition of very thick films can cause the membrane to buckle and stick to the sample surface after it is cooled and removed from the evaporator. We have observed this problem with silicon films greater than 150 nm and with tantalum films of 10 nm (which is deposited at a very high source temperature), both deposited by electron beam evaporation. This effect could presumably be mitigated by performing the evaporation at a lower rate, to reduce the heating of the stencil. We have, however, successfully removed collapsed stencils from the surface of photonic crystal devices by immersion in a standard piranha cleaning solution.

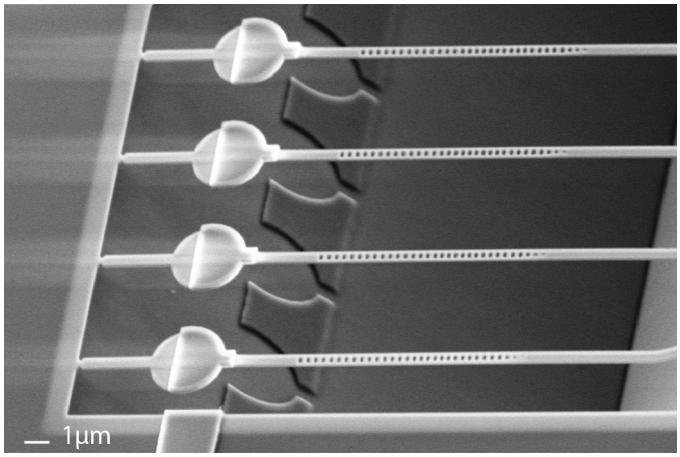

Figure C.2: SEM picture of amorphous silicon stripes deposited across photonic crystal waveguides using a silicon nitride stencil mask. The width of the lines is about 2 μm, and the alignment accuracy to is better than 1 μm. The shadows of the photonic crystal waveguides on the trench sidewall shows that the silicon was deposited after undercutting the waveguides.

The chief limitation of this technique is the requirement that the patterned membrane be structurally stable. This prohibits single-step patterning of closed loops and very long lines. In certain cases, these limitations might be circumvented by leaving many thin connecting bridges and performing double-angle (or more) evaporation to eliminate their shadows on the substrate.

C.4 Final device processing and assembly steps

Picking up where we left off after critical point drying, the final process steps are:

1. **Align stencil** Align stencil and glue into place, as described above

2. **Deposit silicon** in EE-3. We have used thicknesses from 25 - 200 nm (as read on

the crystal monitor) to get varying amounts of absorption. After removing the chip from EE-3, the stencil is pried off.

3. **Clean and CPD again** For good measure, we now piranha clean and critical point dry the sample again. This is ok because the silicon is not affected by piranha (though it would be rapidly removed by the KOH).

Now the devices are ready to be removed from the substrate and attached to a tapered optical fiber. This process is somewhat delicate and requires practice, but the basic steps are:

1. **Pull tapered fiber**

2. **Attach photonic crystal to it** using a tungsten tip manipulated by a 3-axis piezo stage. At this point the fiber-waveguide coupling efficiency should be measured as described in Chapter 5 to ensure it is satisfactory.

3. **SEM fiber and device** to make sure it is installed properly. Additionally, it is good to zoom in tightly to the fiber-waveguide junction and scan the electron beam over that region for about 60 seconds, to deposit some hydrocarbon junk to act as glue.

4. **Align device in UHV chamber mount**, and install it into the UHV chamber.

References

[1] W. K. Wootters and W. H. Zurek, Nature **299**, 802 (1982).

[2] C. H. Bennett and G. Brassard, **175** (1984).

[3] M. O. Scully and M. S. Zubairy, *Quantum Optics* (Cambridge University Press, 1997).

[4] S. Haroche and D. Kleppner, Phys. Today **42**, 24 (1989).

[5] D. Meschede, H. Walther, and G. Müller, Physical Review Letters **54**, 551 (1985).

[6] P. Goy, J. M. Raimond, M. Gross, and S. Haroche, Physical Review Letters **50**, 1903 (1983).

[7] H. J. Kimble, Physica Scripta **1998**, 127 (1998).

[8] T. Kampschulte, W. Alt, S. Brakhane, M. Eckstein, R. Reimann, A. Widera, and D. Meschede, Physical Review Letters **105**, 153603 (2010).

[9] J. Volz, R. Gehr, G. Dubois, J. Estève, and J. Reichel, Nature **475**, 210 (2011).

[10] A. Reiserer, S. Ritter, and G. Rempe, Science **342**, 1349 (2013).

[11] K. Hennessy, A. Badolato, M. Winger, D. Gerace, M. Atatüre, S. Gulde, S. Fält, E. L. Hu, and A. Imamoglu, Nature **445**, 896 (2007).

[12] T. Aoki, B. Dayan, E. Wilcut, W. P. Bowen, A. S. Parkins, T. J. Kippenberg, K. J. Vahala, and H. J. Kimble, Nature **443**, 671 (2006).

[13] D. O'Shea, C. Junge, J. Volz, and A. Rauschenbeutel, Physical Review Letters **111**, 193601 (2013).

[14] N. Schlosser, G. Reymond, I. Protsenko, and P. Grangier, Nature **411**, 1024 (2001).

[15] J. Beugnon, C. Tuchendler, H. Marion, A. Gaëtan, Y. Miroshnychenko, Y. R. P. Sortais, A. M. Lance, M. P. A. Jones, G. Messin, A. Browaeys, et al., Nature Physics **3**, 696 (2007).

[16] J. D. Thompson, T. G. Tiecke, A. S. Zibrov, V. Vuletić, and M. D. Lukin, Physical Review Letters **110**, 133001 (2013).

[17] J. D. Thompson, T. G. Tiecke, N. P. de Leon, J. Feist, A. V. Akimov, M. Gullans, A. S. Zibrov, V. Vuletić, and M. D. Lukin, Science **340**, 1202 (2013).

[18] T. G. Tiecke, J. D. Thompson, N. P. de Leon, L. R. Liu, V. Vuletić, and M. D. Lukin, Nature **508**, 241 (2014).

[19] T. G. Tiecke, K. P. Nayak, J. D. Thompson, T. Peyronel, N. P. de Leon, V. Vuletić, and M. D. Lukin, Submitted (2014).

[20] D. D. Yavuz, P. B. Kulatunga, E. Urban, T. A. Johnson, N. Proite, T. Henage, T. G. Walker, and M. Saffman, Physical Review Letters **96**, 063001 (2006).

[21] M. P. A. Jones, J. Beugnon, A. Gaëtan, J. Zhang, G. Messin, A. Browaeys, and P. Grangier, Physical Review A **75**, 4 (2007).

[22] M. Gibbons, C. Hamley, C.-Y. Shih, and M. Chapman, Physical Review Letters **106**, 133002 (2011).

[23] A. Fuhrmanek, R. Bourgain, Y. Sortais, and A. Browaeys, Physical Review Letters **106**, 133003 (2011).

[24] E. Urban, T. Johnson, T. Henage, L. Isenhower, D. D. Yavuz, T. G. Walker, and M. Saffman, Nature Physics **5**, 110 (2009).

[25] A. Gaëtan, Y. Miroshnychenko, T. Wilk, A. Chotia, M. Viteau, D. Comparat, P. Pillet, A. Browaeys, and P. Grangier, Nature Physics **5**, 115 (2009).

[26] D. Alton, N. Stern, T. Aoki, H. Lee, E. Ostby, K. Vahala, and H. Kimble, Nature Physics **7**, 159 (2011).

[27] E. Vetsch, D. Reitz, G. Sagué, R. Schmidt, S. T. Dawkins, and A. Rauschenbeutel, Physical Review Letters **104**, 203603 (2010).

[28] D. E. Chang, J. D. Thompson, H. Park, V. Vuletic, and M. D. Lukin, Physical Review Letters **103**, 123004 (2009).

[29] D. Hunger, S. Camerer, T. W. Haensch, D. Koenig, J. P. Kotthaus, J. Reichel, and P. Treutlein, Physical Review Letters **104**, 143002 (2010).

[30] M. Hafezi, Z. Kim, S. L. Rolston, L. A. Orozco, B. L. Lev, and J. M. Taylor, Physical Review A **85**, 020302 (2012).

[31] P. Rabl, D. DeMille, J. Doyle, M. Lukin, R. Schoelkopf, and P. Zoller, Physical Review Letters **97**, 33003 (2006).

[32] N. Daniilidis, S. Narayanan, S. A. Moeller, R. Clark, T. E. Lee, P. J. Leek, A. Wallraff, S. Schulz, F. Schmidt-Kaler, and H. Haeffner, New Journal Of Physics **13**, 013032 (2011).

[33] Y. Lin, I. Teper, C. Chin, and V. Vuletić, Physical Review Letters **92**, 50404 (2004).

[34] T. Grünzweig, A. Hilliard, M. McGovern, and M. F. Andersen, Nature Physics **6**, 951 (2010).

[35] C. Tuchendler, A. M. Lance, A. Browaeys, Y. R. P. Sortais, and P. Grangier, Physical Review A **78**, 9 (2008).

[36] W. Rosenfeld, F. Hocke, F. Henkel, M. Krug, J. Volz, M. Weber, and H. Weinfurter, Physical Review Letters **101**, 260403 (2008).

[37] M. K. Tey, G. Maslennikov, T. CH Liew, S. A. Aljunid, F. Huber, B. Chng, Z. Chen, V. Scarani, and C. Kurtsiefer, New Journal Of Physics **11**, 043011 (2009).

[38] C. Monroe, D. Meekhof, B. King, S. Jefferts, W. Itano, D. Wineland, and P. Gould, Physical Review Letters **75**, 4011 (1995).

[39] S. Hamann, D. Haycock, G. Klose, P. Pax, I. Deutsch, and P. Jessen, Physical Review Letters **80**, 4149 (1998).

[40] H. Perrin, A. Kuhn, I. Bouchoule, and C. Salomon, EPL (Europhysics Letters) **42**, 395 (1998).

[41] A. Kerman, V. Vuletic, C. Chin, and S. Chu, Physical Review Letters **84**, 439 (2000).

[42] D. Han, S. Wolf, S. Oliver, C. McCormick, M. DePue, and D. Weiss, Physical Review Letters **85**, 724 (2000).

[43] B. Richards and E. Wolf, Proceedings of the Royal Society A: Mathematical, Physical and Engineering Sciences **253**, 358 (1959).

[44] A. Rohrbach, Physical Review Letters **95**, 168102 (2005).

[45] O. M. Maragò, P. H. Jones, F. Bonaccorso, V. Scardaci, P. G. Gucciardi, A. G. Rozhin, and A. C. Ferrari, Nano Letters **8**, 3211 (2008).

[46] P. J. Reece, W. J. Toe, F. Wang, S. Paiman, Q. Gao, H. H. Tan, and C. Jagadish, Nano Letters **11**, 2375 (2011).

[47] S. Kuhr, W. Alt, D. Schrader, I. Dotsenko, Y. Miroshnychenko, A. Rauschenbeutel, and D. Meschede, Physical Review A p. 023406 (2005).

[48] C. Lacroûte, K. Choi, A. Goban, D. Alton, D. Ding, N. Stern, and H. Kimble, New Journal Of Physics **14**, 023056 (2012).

[49] W. S. Bakr, J. I. Gillen, A. Peng, S. Fölling, and M. Greiner, Nature **462**, 74 (2009).

[50] I. H. Deutsch and P. S. Jessen, Physical Review A **57**, 1972 (1998).

[51] K. Corwin, S. Kuppens, D. Cho, and C. Wieman, Physical Review Letters **83**, 1311 (1999).

[52] L. Förster, M. Karski, J. Choi, A. Steffen, W. Alt, D. Meschede, A. Widera, E. Montano, J. Lee, W. Rakreungdet, et al., Physical Review Letters **103**, 233001 (2009).

[53] X. Li, T. Corcovilos, Y. Wang, and D. Weiss, Physical Review Letters **108**, 103001 (2012).

[54] P. Lett, R. Watts, C. Westbrook, W. Phillips, P. Gould, and H. Metcalf, Physical Review Letters **61**, 169 (1988).

[55] M. McGovern, A. J. Hilliard, T. Grünzweig, and M. F. Andersen, Optics Letters **36**, 1041 (2011).

[56] A. M. Kaufman, B. J. Lester, and C. A. Regal, Physical Review X **2**, 041014 (2012).

[57] C. Monroe and M. D. Lukin, Physics World **21**, 32 (2008).

[58] M. Wallquist, K. Hammerer, P. Rabl, M. Lukin, and P. Zoller, Physica Scripta **2009**, 014001 (2009).

[59] B. Dayan, A. Parkins, T. Aoki, E. Ostby, K. Vahala, and H. Kimble, Science **319**, 1062 (2008).

[60] M. Hijlkema, B. Weber, H. P. Specht, S. C. Webster, A. Kuhn, and G. Rempe, Nature **3**, 253 (2007).

[61] D. E. Chang, A. S. Sorensen, E. A. Demler, and M. Lukin, Nature Physics **3**, 807 (2007).

[62] I. Fushman, D. Englund, A. Faraon, N. Stoltz, P. Petroff, and J. Vuckovic, Science **320**, 769 (2008).

[63] H. J. Kimble, Nature **453**, 1023 (2008).

[64] C. Nölleke, A. Neuzner, A. Reiserer, C. Hahn, G. Rempe, and S. Ritter, Physical Review Letters **110**, 140403 (2103).

[65] I. Dotsenko, W. Alt, M. Khudaverdyan, S. Kuhr, Y. Miroshnychenko, D. Schrader, and A. Rauschenbeutel, Physical Review Letters **95**, 033002 (2005).

[66] R. Gehr, J. Volz, G. Dubois, T. Steinmetz, Y. Colombe, B. Lev, R. Long, J. Estève, and J. Reichel, Physical Review Letters **104**, 203602 (2010).

[67] A. Goban, K. Choi, D. Alton, D. Ding, C. Lacroûte, M. Pototschnig, T. Thiele, N. Stern, and H. Kimble, Physical Review Letters **109**, 033603 (2012).

[68] R. A. Cornelussen, A. H. Van Amerongen, B. T. Wolschrijn, R. Spreeuw, and H. B. van Linden van den Heuvell, The European Physical Journal D-Atomic, Molecular, Optical and Plasma Physics **21**, 347 (2002).

[69] D. Chang, J. Thompson, H. Park, V. Vuletic, A. Zibrov, P. Zoller, and M. Lukin, Physical Review Letters **103**, 123004 (2009).

[70] P. R. Villeneuve, J. S. Foresi, J. Ferrera, E. R. Thoen, G. Steinmeyer, S. Fan, J. D. Joannopoulos, L. C. Kimerling, H. I. Smith, and E. P. Ippen, Nature **390**, 143 (1997).

[71] B. Lev, K. Srinivasan, P. Barclay, O. Painter, and H. Mabuchi, NANOTECHNOLOGY **15**, S556 (2004).

[72] C. L. Hung, S. M. Meenehan, D. E. Chang, O. Painter, and H. J. Kimble, New Journal Of Physics **15**, 083026 (2013).

[73] E. Hecht, *Optics* (Addison Wesley Longman, Reading, MA, 1998), 3rd ed.

[74] J. Ye, H. J. Kimble, and H. Katori, Science **320**, 1734 (2008).

[75] M. Eichenfield, R. Camacho, J. Chan, K. J. Vahala, and O. Painter, Nature **459**, 550 (2009).

[76] M. J. Hartmann, F. G. S. L. Brandao, and M. B. Plenio, Nature Physics **2**, 849 (2006).

[77] A. D. Greentree, C. Tahan, J. H. Cole, and L. C. L. Hollenberg, Nature **2**, 856 (2006).

[78] A. André, D. DeMille, J. M. Doyle, M. D. Lukin, S. E. Maxwell, P. Rabl, R. J. Schoelkopf, and P. Zoller, Nature Physics **2**, 636 (2006).

[79] M. Gullans, T. Tiecke, D. Chang, J. Feist, J. Thompson, J. Cirac, P. Zoller, and M. Lukin, Physical Review Letters **109**, 235309 (2012).

[80] O. Romero-Isart, C. Navau, A. Sanchez, P. Zoller, and J. I. Cirac, Physical Review Letters **111**, 145304 (2013).

[81] J. Cirac, P. Zoller, H. J. Kimble, and H. Mabuchi, Physical Review Letters **78**, 3221 (1997).

[82] L. M. Duan and C. Monroe, Reviews Of Modern Physics **82**, 1209 (2010).

[83] J. M. Raimond and S. Haroche, *Exploring the quantum* (Oxford University Press, 2006).

[84] H.-J. Briegel, W. Dür, J. I. Cirac, and P. Zoller, Physical Review Letters **81**, 5932 (1998).

[85] P. Kómár, E. M. Kessler, M. Bishof, L. Jiang, A. S. Sorensen, J. Ye, and M. D. Lukin, Nature Physics **10**, 582 (2014).

[86] I. Carusotto and C. Ciuti, Reviews Of Modern Physics **85**, 299 (2013).

[87] L. M. Duan and H. J. Kimble, Physical Review Letters **92**, 127902 (2004).

[88] I. Schuster, A. Kubanek, A. Fuhrmanek, T. Puppe, P. W. H. Pinkse, K. Murr, and G. Rempe, Nature Physics **4**, 382 (2008).

[89] T. Aoki, A. Parkins, D. Alton, C. Regal, B. Dayan, E. Ostby, K. Vahala, and H. J. Kimble, Physical Review Letters **102**, 083601 (2009).

[90] W. Chen, K. M. Beck, R. Bucker, M. Gullans, M. D. Lukin, H. Tanji-Suzuki, and V. Vuletić, Science **341**, 768 (2013).

[91] T. Volz, A. Reinhard, M. Winger, A. Badolato, K. J. Hennessy, E. L. Hu, and A. Imamoğlu, Nature Photonics **6**, 607 (2012).

[92] H. Kim, R. Bose, T. C. Shen, G. S. Solomon, and E. Waks, Nature Photonics **7**, 373 (2013).

[93] D. I. Schuster, A. A. Houck, J. A. Schreier, A. Wallraff, J. M. Gambetta, A. Blais, L. Frunzio, J. Majer, B. Johnson, M. H. Devoret, et al., Nature **445**, 515 (2007).

[94] S. Gleyzes, S. Kuhr, C. Guerlin, J. Bernu, S. Deleglise, U. Busk Hoff, M. Brune, J.-M. Raimond, and S. Haroche, Nature **446**, 297 (2007).

[95] S. Deleglise, I. Dotsenko, C. Sayrin, J. Bernu, M. Brune, J.-M. Raimond, and S. Haroche, Nature **455**, 510 (2008).

[96] Q. Turchette, C. Hood, W. Lange, H. Mabuchi, and H. J. Kimble, Physical Review Letters **75**, 4710 (1995).

[97] S. Ritter, C. Nölleke, C. Hahn, A. Reiserer, A. Neuzner, M. Uphoff, M. Mücke, E. Figueroa, J. Bochmann, and G. Rempe, Nature **484**, 195 (2012).

[98] M. H. Devoret and R. J. Schoelkopf, Science **339**, 1169 (2013).

[99] E. Waks and J. Vuckovic, Physical Review Letters **96**, 153601 (2006).

[100] D. Witthaut, M. D. Lukin, and A. S. Sorensen, EPL (Europhysics Letters) **97**, 50007 (2012).

[101] B. Wang and L. M. Duan, Physical Review A **72**, 022320 (2005).

[102] J. D. Joannopoulos, S. G. Johnson, J. Winn, and R. Meade, *Photonic Crystals: Molding the flow of light* (Princeton University Press, MIT, 2008).

[103] X. Chen, C. Li, and H. K. Tsang, NPG Asia Materials **3**, 34 (2011).

[104] D. A. B. Miller, Nature Photonics **4**, 3 (2010).

[105] D. W. Pohl, W. Denk, and M. Lanz, Applied Physics Letters **44**, 651 (1984).

[106] A. Lewis, M. Isaacson, A. Harootunian, and A. Muray, Ultramicroscopy **13**, 227 (1984).

[107] W. Tan, Z. Shi, S. Smith, D. Birnbaum, and R. Kopelman, Science **258**, 778 (1992).

[108] R. Yan, J.-H. Park, Y. Choi, C.-J. Heo, S.-M. Yang, L. P. Lee, and P. Yang, Nature Nanotechnology **7**, 191 (2011).

[109] T. D. Ladd, F. Jelezko, R. Laflamme, Y. Nakamura, C. Monroe, and J. L. O'brien, Nature **464**, 45 (2010).

[110] R. van Meter, T. D. Ladd, A. G. Fowler, and Y. Yamamoto, International Journal of Quantum Information **08**, 295 (2010).

[111] T. Yoshie, A. Scherer, J. Hendrickson, G. Khitrova, H. M. Gibbs, G. Rupper, C. Ell, O. B. Shchekin, and D. G. Deppe, Nature **432**, 200 (2004).

[112] J. D. Cohen, S. M. Meenehan, and O. Painter, Optics Express **21**, 11227 (2013).

[113] S. Gröblacher, J. T. Hill, A. H. Safavi-Naeini, J. Chan, and O. Painter, Applied Physics Letters **103**, 181104 (2013).

[114] A. W. Snyder and J. D. Love, *Optical Waveguide Theory* (Chapman and Hall, London, 1983).

[115] J. D. Love, W. M. Henry, W. J. Stewart, R. J. Black, S. Lacroix, and F. Gonthier, Iee Proceedings-J Optoelectronics **138**, 343 (1991).

[116] J. E. Hoffman, S. Ravets, J. A. Grover, P. Solano, P. R. Kordell, J. D. Wong-Campos, L. A. Orozco, and S. L. Rolston, AIP Advances **4**, 067124 (2014).

[117] A. Stiebeiner, R. Garcia-Fernandez, and A. Rauschenbeutel, Optics Express **18**, 22677 (2010).

[118] S. G. Johnson and J. D. Joannopoulos, Optics Express **8**, 173 (2001).

[119] L. Tong, R. R. Gattass, J. B. Ashcom, S. He, J. Lou, M. Shen, I. Maxwell, and E. Mazur, Nature **426**, 816 (2003).

[120] J. M. Ward, A. Maimaiti, V. H. Le, and S. N. Chormaic, arXiv.org (2014), 1402.6396v1.

[121] G. Brambilla, Journal of Optics **12**, 043001 (2010).

[122] G. Shambat, S.-R. Kothapalli, J. Provine, T. Sarmiento, J. Harris, S. S. Gambhir, and J. Vuckovic, Nano Letters **13**, 4999 (2013).

[123] L. M. Duan, B. Wang, and H. J. Kimble, Physical Review A **72**, 032333 (2005).

[124] I. Bloch, J. Dalibard, and W. Zwerger, Reviews Of Modern Physics **80**, 885 (2008).

[125] S. Trotzky, P. Cheinet, S. Fölling, M. Feld, U. Schnorrberger, A. M. Rey, A. Polkovnikov, E. A. Demler, M. D. Lukin, and I. Bloch, Science **319**, 295 (2008).

[126] B. Yan, S. A. Moses, B. Gadway, J. P. Covey, K. R. Hazzard, A. M. Rey, D. S. Jin, and J. Ye, Nature **501**, 521 (2013).

[127] M. Saffman, T. G. Walker, and K. Molmer, Reviews Of Modern Physics **82**, 2313 (2010).

[128] H. Ritsch, P. Domokos, F. Brennecke, and T. Esslinger, Reviews Of Modern Physics **85**, 553 (2013).

[129] J. S. Douglas, H. Habibian, A. V. Gorshkov, H. J. Kimble, and D. E. Chang, arXiv.org (2013), 1312.2435v1.

[130] A. González-Tudela, C. L. Hung, D. E. Chang, J. I. Cirac, and H. J. Kimble, arXiv.org (2014), 1407.7336v1.

[131] K. P. Nayak, P. N. Melentiev, M. Morinaga, F. Le Kien, V. I. Balykin, and K. Hakuta, Optics Express **15**, 5431 (2007).

[132] M. Antezza, Pitaevskii, L.P., and S. Stringari, Physical Review A **70**, 053619 (2004).

[133] A. Derevianko, S. G. Porsev, and J. F. Babb, Atomic Data and Nuclear Data Tables **96**, 323 (2010).

[134] E. D. Palik, *Handbook of Optical Constants of Solids*, vol. 1 (Academic Press, Inc., Orlando, 1985).

[135] M. Klanjšek Gunde and M. Maček, Physica status solidi (a) **183**, 439 (2001).

[136] S. Buhmann, Ph.D. thesis, Friedrich-Schiller-Universität Jena (2007).

[137] J. M. Obrecht, R. J. Wild, and E. A. Cornell, Physical Review A **75**, 7 (2007).

[138] K. P. Nayak and K. Hakuta, New Journal Of Physics **10**, 053003 (2008).

[139] V. V. Klimov and M. Ducloy, Physical Review A **69**, 13812 (2004).

[140] H. J. Carmichael, *Statistical Methods in Quantum Optics 1: Master Equations and Fokker-Planck Equations* (Springer-Verlag New York Inc., New York, NY, 2002).

[141] P. R. Rice and H. J. Carmichael, Quantum Electronics, IEEE Journal of **24**, 1351 (1988).

[142] K. Williams, K. Gupta, and M. Wasilik, Journal of Microelectromechanical Systems **12**, 761 (2003).

[143] M.-A. Nicolet, Thin Solid Films **52**, 415 (1978).

[144] N. A. Stolwijk, B. Schuster, and J. Hölzl, Applied Physics A **33**, 133 (1984).

[145] S. Aksu, A. A. Yanik, R. Adato, A. Artar, M. Huang, and H. Altug, Nano Letters **10**, 2511 (2010).

[146] M. J. K. Klein, F. Montagne, N. Blondiaux, O. Vazquez-Mena, H. Heinzelmann, R. Pugin, J. Brugger, and V. Savu, Journal Of Vacuum Science & Technology B **29**, 021012 (2011).